Aalto University
School of Chemical
Engineering

School of Chemical Technology
Degree Programme of Chemical Technology

Manu Tenhunen

ATOMIC LAYER DEPOSITION OF NICKEL MANGANESE OXIDES

Master's thesis for the degree of Master of Science in Technology submitted for inspection, Espoo, 22 May, 2017.

Supervisor Academy Professor Maarit Karppinen

Instructor Ph.D. Dirk Hagen

Aalto University
School of Chemical Engineering

Aalto University, P.O. BOX 11000, 00076 AALTO
www.aalto.fi

Abstract of master's thesis

Author Manu Tenhunen

Title of thesis Atomic layer deposition of nickel manganese oxides

Department Department of chemistry

Major Chemistry

Thesis supervisor Academy Professor Maarit Karppinen

Thesis advisor(s) / Thesis examiner(s) Ph.D Dirk Hagen

Date 22.05.2017 **Number of pages** 100 **Language** English

Abstract

Ternary metal oxides are among the most researched areas in inorganic chemistry. They are interesting because they offer a wide range of functionalities and their properties can be controlled with correct fabrication methods. One such method is atomic layer deposition (ALD) which, in theory, makes it possible to control the structure of the material down to the level of atom layers. In general, the atomic layer deposition of ternary oxides is challenging but the problems can be overcome with careful design of the ALD reactor and its parameters.

One of the interesting materials in ternary oxides is the nickel manganese oxides which have three different structures: Spinel structure ($NiMn_2O_4$), ilmenite structure ($NiMnO_3$) and murdochite structure (Ni_6MnO_8). The spinel structured $NiMn_2O_4$ has been the most interesting one and shown good results in practical applications such as an electrode material for lithium ion batteries. The other structures have been researched as potential catalysts for oxygen evolution and reduction reactions for devices like fuel cells. Nickel manganese oxide thin films have been fabricated before but not with ALD.

In this work, ALD is used to fabricate nickel manganese oxide thin films and their crystal structures are determined with grazing angle incidence x-ray diffraction (GIXRD). $Mn(thd)_3$, $Ni(thd)_2$ and ozone are used as precursor materials. Different ratios of nickel and manganese are deposited in various temperatures to see if this causes any difference to the structure. In addition, the thin films are heat-treated and their crystal structures are examined afterwards. Some magnetic and optical measurements are also taken.

Keywords atomic layer deposition, ternary metal oxide, nickel manganese oxides

Aalto-yliopisto
Kemian tekniikan korkeakoulu

Aalto-yliopisto, PL 11000, 00076 AALTO
www.aalto.fi

Diplomityön tiivistelmä

Tekijä Manu Tenhunen

Työn nimi Nikkelimangaanioksidien atomitasokasvatus

Laitos Kemian laitos

Pääaine Kemia

Työn valvoja Professori Maarit Karppinen

Työn ohjaaja(t)/Työn tarkastaja(t) Ph.D Dirk Hagen

Päivämäärä 22.05.2017 **Sivumäärä** 100 **Kieli** Englanti

Tiivistelmä

Ternääriset metallioksidit ovat tutkituimpia alueita epäorgaanisessa kemiassa. Ne ovat erityisen kiinnostavia funktionaalisuuksiensa takia ja siksi, että niiden ominaisuudet ovat säädeltävissä oikeilla valmistustekniikoilla. Eräs tällainen valmistustapa on atomitasokasvatus (ALD), jonka avulla on teoriassa mahdollista kontrolloida materiaalin rakennetta jopa atomitasoille asti. Yleisesti ottaen ternääristen metallioksidien atomitasokasvatus on haastavaa, mutta sen ongelmat voidaan usein ratkaista muuttamalla ALD-reaktorin kokoonpanoa tai sen parametreja.

Yksi kiinnostava osa ternäärisiä metallioksideja on nikkelimangaanioksidit, joille on kolme eri rakennetta: spinellirakenne ($NiMn_2O_4$), ilmenite-rakenne ($NiMnO_3$) ja murdochite-rakenne (Ni_6MnO_8). Spinellirakenteinen $NiMn_2O_4$ on rakenteista tutkituin ja osoittanut hyvää suorituskykyä käytännön sovelluksissa kuten elektrolyyttimateriaalina litiumioniakuissa. Muita rakenteita on tutkittu potentiaalisina katalysaattoreina hapen kehitys- ja pelkistysreaktioille esimerkiksi polttokennoihin. Nikkelimangaanioksidi ohutkalvoja on valmistettu ennen, mutta ei käyttäen atomitasokasvatusta.

Tässä työssä nikkelimangaanioksidi ohutkalvoja valmistetaan atomitasokasvatuksella ja niiden kiderakenne määritetään röntgenkristallografialla. $Mn(thd)_3$, $Ni(thd)_2$ ja otsoni toimivat lähtöaineina. Nikkelin ja mangaanin määrää sekä kasvatuslämpötilaa vaihdellaan, jotta nähdään näiden vaikutus rakenteeseen. Lisäksi ohutkalvoja lämpökäsitellään ja niiden kiderakenteet tutkitaan tämän jälkeen. Joitain magneettisia ja optisia ominaisuuksia myös mitataan.

Avainsanat Atomitasokasvatus, ternääriset oksidit, ohutkalvo

Preface

The experimental work was done at Laboratory of Inorganic Chemistry at Aalto University School of Chemical Engineering during from the end of summer 2016 until the summer of 2017. In addition, the facilities of Aalto University Nanomicroscopy Center were used in some measurements.

First I want to thank Professor Antti Karttunen for talking me about the diploma thesis position in the inorganic group. In addition, I'm grateful to my supervisor Professor Maarit Karppinen for helping me with the literature part of the work and to thesis advisor Ph.D Dirk Hagen for spending numerous working hours helping me with experimental and literature work. The research of this thesis could not have been made without the help of Dirk. Big thanks to all my co-workers but especially to Mikko Stenholm and Juho Heiska with whom I shared a room and who gave me a lot of practical information regarding the laboratories and the thesis.

I was very happy to be able to do my thesis for the Laboratory of Inorganic Chemistry. The laboratories and the working environment in general were excellent. Last, I thank my friends and family for supporting this endeavor through the studies.

Espoo 22.05.2017

Manu Tenhunen

Table of contents

1 Introduction 1

Literature part

2 Atomic layer deposition 3

2.1 The principle of ALD 3

2.2 Reactor design 6

2.3 Materials 11

2.4 Thin films 13

3 Ternary oxides 15

3.1 Perovskite structure 16

3.2 Applications for ternary oxides 17

3.3 Problems associated with ALD of ternary oxides 21

4 Nickel manganese oxides 23

4.1 Spinel: $Ni_xMn_{3-x}O_4$ 27

4.2 Ilmenite: $NiMnO_3$ 29

4.3 Murdochite: $Ni_{6+2x}Mn_{1-x}O_8$ 30

4.4 Synthetization of nickel manganese oxides 31

4.5 Applications 35

4.6 Atomic layer deposition of nickel oxide and manganese oxide 39

Experimental part

5 Research goals 42

6 Sample preparation 42

6.1 Precursors’ syntheses 42

6.2 Thin film deposition 44

6.3 Annealing 45

7 Characterizations 47

7.1 X-ray reflectivity 47

7.2 Grazing angle incidence x-ray diffraction 48

7.3 Spectroscopy 49

7.4 Magnetic measurements 51

7.5 Scanning electron microscopy 52

8 Results 53

8.1 Quality of the thin films 53

8.2 ALD-reactor optimization 57

8.3 Crystal structure of the thin films 61

8.4 Annealing 70

8.5 Spectroscopy 75

8.6 Magnetic measurements 77

9 Conclusions 83

10 Further research 85

References 87

1 Introduction

Ternary metal oxides (oxides containing two additional metallic elements) are among the most researched areas in inorganic chemistry. They are particularly interesting because they have the good electrical properties of the metals while offering a wide range of interesting functionalities such as ferroelectricity. Ternary oxides have many possible crystal structures including the spinel and perovskite structures which are researched intensively. Some ternary metal oxides are already widely used in various applications. For instance, indium tin oxide (ITO) is one the most used transparent conducting oxide materials and is commonly utilized in displays including flexible displays. Ternary metal oxides are also frequently used in state-of-the art electrical devices such as solar cells, supercapacitors, and fuel cells.

One long studied class of ternary metal oxides is the nickel manganese oxides. Nickel manganese oxides are particularly interesting because both nickel and manganese have excellent properties as sole materials. For example, they are cheap and abundant, chemically stable and form durable compounds. The partially filled d electron sub-shell of transition of metals gives them intriguing properties such as multiple oxidation states and paramagnetism. The most known and well-studied nickel manganese oxide is the spinel structured $NiMn_2O_4$ but ilmenite ($NiMnO_3$) and murdochite (Ni_6MnO_8) structures exist as well. The most promising application for nickel manganese oxides is as a cathode material for high energy density devices such as lithium ion batteries.

Research of ternary metal oxides has advanced from bulk materials towards complex structures and thin film coatings. In modern state of the art electronic devices, it is essential to control the structure of the material on nanometer scale and even small defects can break the devices. This is why atomic layer deposition (ALD) has become an important fabrication method for ternary oxides. It works by sequentially depositing layers of atoms and ideally allows very precise control down to a single layer of atoms. ALD of ternary oxides is usually difficult requiring precise optimization of the deposition parameters and fine-tuning the ALD-reactor. Even though nickel manganese thin films have been fabricated for long, there are no published articles describing atomic layer deposition of nickel manganese oxides.

In the literature part of this thesis, the topics of atomic layer deposition, ternary oxides and nickel manganese oxides are covered. The concept of ALD is given in detail focusing on the reactor design and on the features concerning the deposition of ternary oxides. Ternary oxides, their applications and problems associated with them are introduced to pave the way for the nickel manganese oxides. The different structures of nickel manganese oxides and their inherent properties are presented but also the spinel and perovskite structures are introduced. In addition, the most common applications and different fabrication methods for nickel manganese oxides are introduced giving a broad overview of the literature covering nickel manganese oxides.

The experimental part of the thesis is focused on ALD of nickel manganese oxides. The goal of the experimental work was to deposit thin films of spinel structured $NiMn_2O_4$ and investigate their electric and magnetic properties. First the reactor needed to be optimized for the deposition after which nickel and manganese were deposited in various ratios to see if this causes any difference. The crystal structures of the deposited oxides were characterized with X-ray diffraction (XRD) and some optical, electrical and magnetic measurements were conducted. The deposited nickel manganese oxides were also heat-treated in different temperatures and atmospheres to see if this had any effect on the material. The results were analyzed and compared with the literature on the area. Last, suggestions are given how to advance on the research of nickel manganese oxides with atomic layer deposition.

Literature part

2 Atomic layer deposition

Atomic layer deposition (ALD), also known by such names as atomic layer epitaxy (ALE) and molecular lamination (ML), is a gas-to-surface layer-by-layer thin film deposition technique developed by two independent research groups (Aleskovskii *et al.* in the Soviet Union [1] and Suntola *et al.* in Finland [2]) during the 60's and the early 70's. But it was until the 1990s and 2000s when the usage and research of ALD became more common. The trending is mostly due to the advances both in ALD technique and microfabrication in general but also due to miniaturization of integrated circuits for electronic devices such as computers and mobile phones. [3]

2.1 The principle of ALD

ALD is strongly related to the chemical vapor deposition (CVD) technique. Both are gas-to-surface processes to grow thin films which chemically bond to the substrate. The big difference between ALD and CVD processes is that ALD uses sequential self-limiting reactions where the gasses react with the surface one at a time while in CVD the starting materials react with together on the surface of the substrate. In ALD, precursors (starting materials) are fed to the reaction chamber one after another and left to completely react with the surface before purging the reactor empty with inert gas. This means that every possible chemical reaction site on the surface of the substrate is filled and the reaction is self-terminating, leaving no possibility for unwanted reactions. Hence, purity of ALD thin films can at best be over 99 atom-% and the film quality is usually very uniform [4]. The small impurities can rise from precursor materials, residues left to reaction chamber and from reactions between the carrier gas and oxygen. [5]

ALD allows the deposition of a single layer of atoms layer-by-layer on many different substrates that can even have complex three-dimensional shapes. In theory, the growth rate of trenches and walls are similar to growth rates in completely flat substrates making

the technique suitable for complex shapes. Furthermore, the deposited films are uniform, usually pinhole-free and the thickness and the composition of the layer can be controlled with great accuracy. These characteristics are extremely important in small-scale devices such as MOSFETs in which details of the nanometer size are required and even very small defects can render the device useless. [6]

An ideal binary ALD reaction consists of a four-step cycle: First, a precursor is introduced to the reactor where it reacts with surface sites on the substrate. Once the reaction is complete, an inert gas purge removes extra precursor material and gaseous reaction by-products. Then, the other reactant is transported into the reactor where it reacts with the adsorbed precursor. Last, the reactor is purged to remove extra materials and another ALD cycle can begin. One cycle of ALD ideally produces a certain amount of film thickness (known as growth per cycle, GPC) making it easy to control film thicknesses. A common binary ALD cycle is illustrated in Figure 1.

An ALD process has a specific temperature range in which the growth is near ideal called the "ALD-window" which typically ranges somewhere in between 100 and 400 °C. During the ideal temperature window, the reaction is self-limiting and complete meaning that the chemical adsorption is irreversible and that all surface sites are filled. If the temperature is too low for a certain precursor, it may not react with all the available surface sites or could condense on the substrate decreasing or increasing the growth rate. On the other hand, a too high temperature can cause self-decomposition and other unwanted chemical reactions. During an ideal ALD process, parameters like gas pressures should not have an effect on the growth rate and processes should be easily replicated from lab to lab as long as the temperatures and the materials are the same. [7]

The ALD-window can be searched by changing the pulse and purge lengths and plotting those against growth per cycle. In an ideal saturated process, this should form a linear line on the graph. Usually the ideal ALD temperature window can be as wide as 50 or 100 °C but in some cases it can be as low as 10 °C.

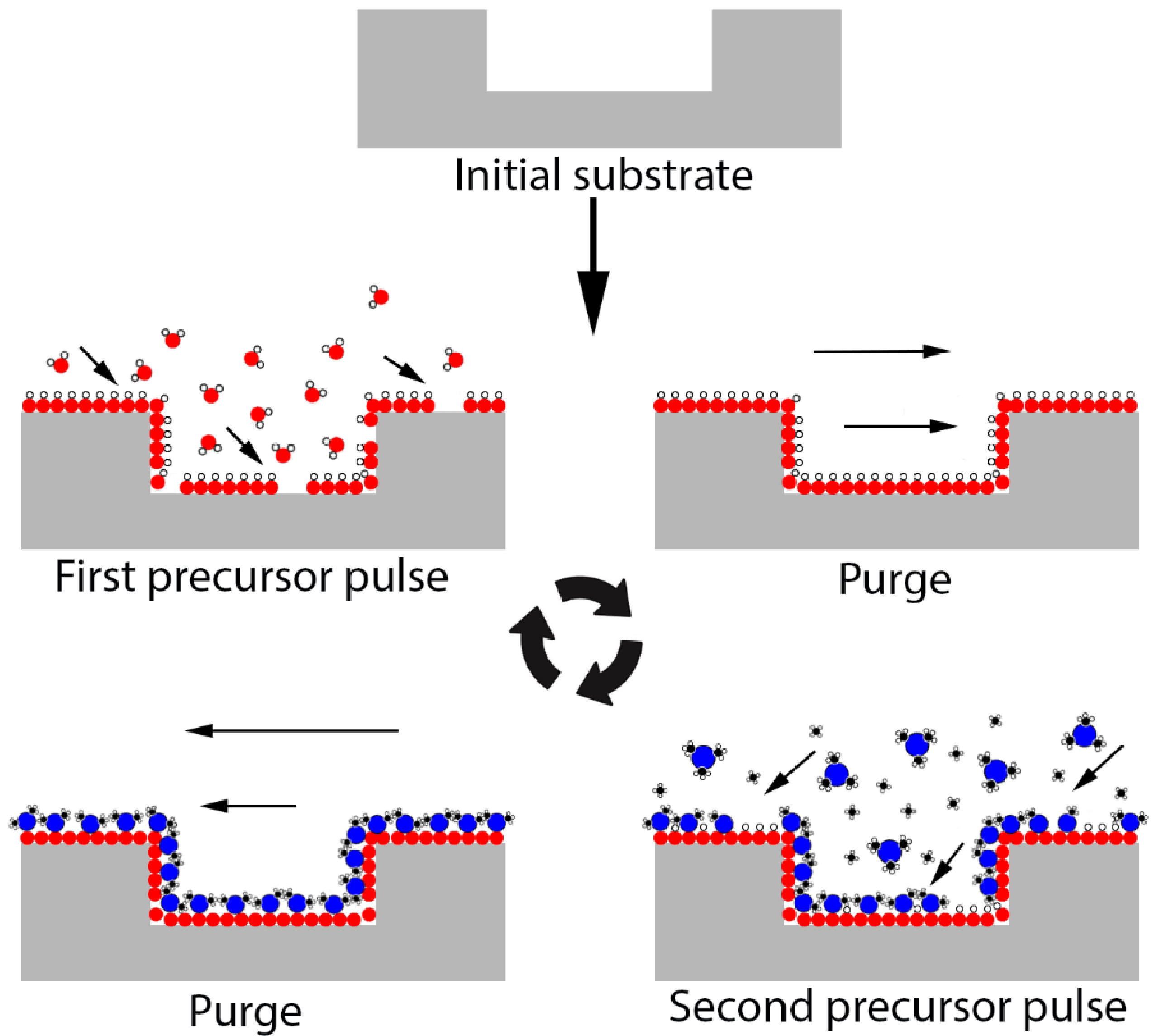

Figure 1. Illustration of an ALD cycle with H_2O and $Al(CH_3)_3$ precursors to produce Al_2O_3 thin film.

2.2 Reactor design

The first ALD reactors were based on physical vapor deposition (PVD), or more exactly molecular beam epitaxy (MBE), reactors. Precursors were evaporated from two different sources and sequentially exposed to the substrate using a spinning substrate holder and shutters to block the other gas flow, as shown in Figure 2. However, as the reactors developed a horizontal reactor or so called "travelling-wave" type of design got popular. This design is similar to tubular CVD reactors where gasses flow horizontally through the wall of the reactor chamber. For example, the first commercial ALD reactor used travelling-wave design and a tube structure but nowadays, most commercial reactors rely on vertical flow because of better thin film uniformity. [3]

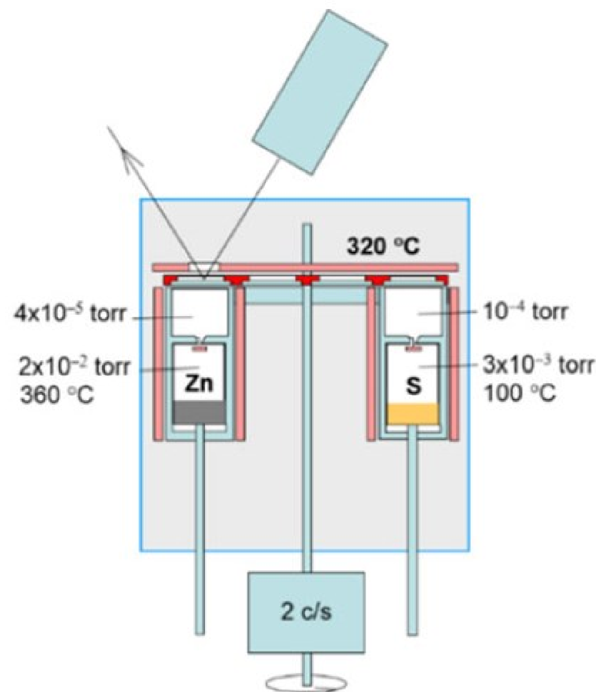

Figure 2. Drawing of the deposition mechanism and the parameters used in the very first ALD reactor [3]. Spinning substrate holder switched the place of the substrate from one side to another allowing sequential exposure to different gasses. Elemental zinc and sulfur were heated to get adequate gas pressures.

One way to classify ALD reactors is the way they are heated. The chamber of the reactor can be either heated completely (so called hot-wall reactor) or only the substrate is heated inside the chamber (cold-wall reactor). There are also combinations of the two; for example, reactors which have independently heated substrate and separately heated reactor so the classification is not always that simple. Some precursors may require the extra heating done by the hot-wall reactor before they reach the substrate to deposit properly and some precursors may condensate on the walls of a cold-wall reactor. On the other hand, cold-wall reactor is faster to use because of shorter heating and cooling times.

One major difference in reactor design can come from the way the precursors are fed to the reaction chamber. The precursors can be directly transported to the reaction chamber with pumping or by utilizing inner pressure differences of the reactor or they can flow with assist from an inert carrier gas. There are also multiple ways for an ALD reactor to flow the reacting gas to the substrate. The common way is via cross-flow where the gas flow is parallel to the substrate. Cross-flow also suits batch processing where large amounts of substrates are deposited the same time. The gas flow can as well be perpendicular to the substrate and transported to the chamber via showerhead kind of nozzle that spreads the gas evenly across the surface. Even though one can spread the gas more evenly with the showerhead nozzle and could get more uniform results, it dramatically slows the deposition time because evacuation times are longer due to non-parallel gas flow. Thus, showerhead nozzles are mainly used in semiconductor processing where extreme purity and uniformity is pursued.

ALD precursors can be in gas form and directly fed to the reactor but this is not always the case. Some reactants can be solids or liquids and they need to be gasified before the delivery to the reactor which is done with the help of Liquid delivery systems (LDS) and solid delivery systems (SDS). Aerosol delivery systems also exists but they are very rarely used in ALD.

The simplest and most common delivery system in ALD is the direct vapor draw system in which the precursor is either fed from a bottled gas source or held in the heated vaporizer. Once the container is opened, the gasified precursor exits the vaporizer or the bottle by itself (pressure difference) and is transported to the reaction chamber with carrier gas. Direct draw systems are simple and cheap to build but as the whole precursor container is heated there can be thermal decomposition. In addition, it is difficult to get a steady

precursor flow from the system but this is usually not considered a problem in ALD due to its self-limiting nature. Open boat system has some similarities to vapor draw system. It is usually utilized in tubular ALD reactors and features an open vessel with most often solid precursor in it contained in a separate tube of the reactor, shown in Figure 3. The vessel is kept heated and the precursor evaporates in to the tube from which it can be separately drawn into the reaction chamber with the help of carrier gas. [8]

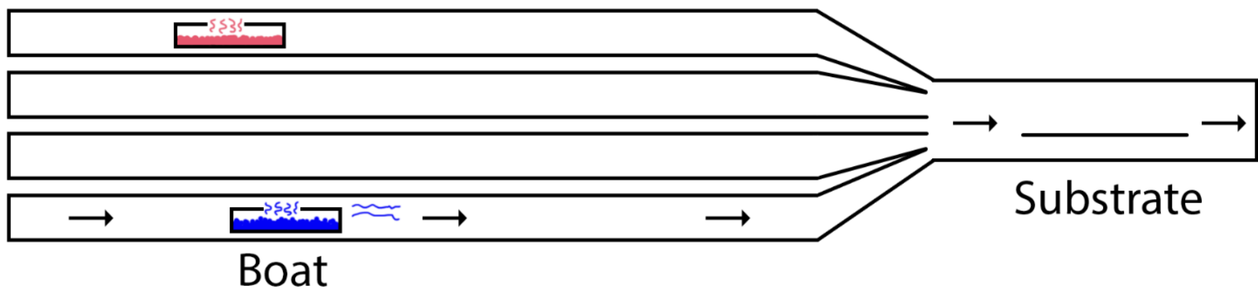

Figure 3. Illustration of tubular ALD reactor using heated open vessels to sublimate the precursors. Carrier gas transports the precursor gas to the substrate one at a time.

A bubbler is a device to ease the gasifying of some difficult precursors. Usually, steadier gas flow can be achieved with lower temperatures. In a bubbler system, the carrier gas is fed through the bubbler containing the precursor so the precursor is sublimated or evaporated and transported to the reactor by the gas flow going through the precursor material. Typical bubbler design is similar to a Dreschler bottle as illustrated in Figure 4. Bubblers almost always require heating and sometimes multiple bubblers in a row might be needed to produce sufficient evaporation. However, problems such as entrainment of small liquid droplets within the carrier gas may persist. [9]

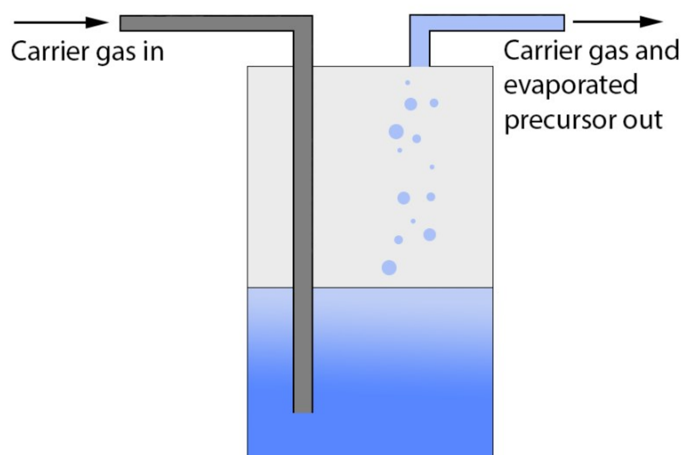

Figure 4. Sketch of a simple bubbler evaporator.

Direct liquid injection (DLI) system is the most advanced of the systems as it has a precursor container and a separate vaporizer which means there is no unwanted evaporation or thermal decomposition of the precursor. The precursor is delivered or injected to the vaporizer where it evaporates and is swept to the reaction chamber by a carrier gas. The vaporization of precursor can be done in multiple different ways; heated chambers are the most common way but devices such as lasers and IR-lamps can also be used. The amount of injected precursor and thus the amount of gasified precursor can be controlled with great accuracy and the generated gas flow is stable. Either solid or liquid precursors can be used in DLI systems but solids need to be dissolved into a solvent first. There are numerous patents and different kind of systems for DLI and one is illustrated in Figure 5. [8]

Both the liquid and the solid delivery systems have some common problems. As mentioned, low volatility precursors may require intense heating which in turn could cause the precursor to condense on a cold part of a system demanding the whole feed line and the reactor to be heated. Solid precursors cause the biggest issues. If the solid is not dissolved into a liquid, it needs to be sublimated. Problems of sublimation rise from the difficulties of keeping heating and surface area constant; as the solid gasifies its surface area changes which addedly changes the sublimation rate of the solid. If gas is

running through a solid precursor, it is challenging to get a uniform gas flow through the whole area of the solid. Fluidized beds, large surface areas, and pressing of the solid are few of the ways to enhance stable sublimation. Solids can always be dissolved into liquids but this may cause its own line of problems. The solvent itself can produce impurities and the solid may not necessarily be stable in the solution. Also, the evaporation of the mixture could only gasify the liquid and leave most of the solid precursor to the vaporizer causing low precursor flow and constant need for maintenance of the system. [8,9]

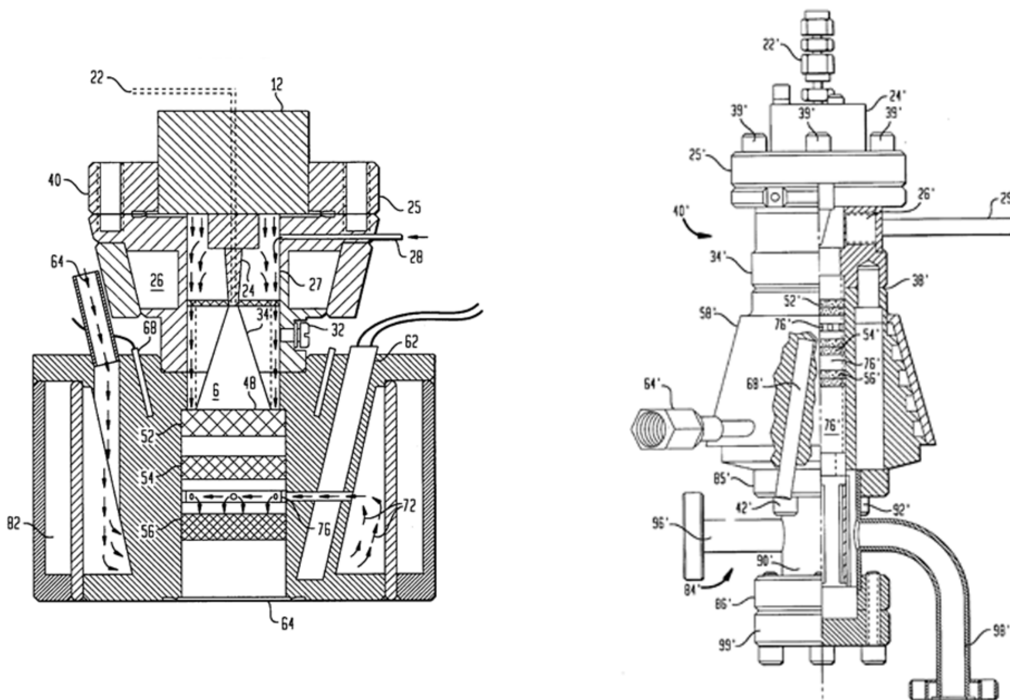

Figure 5. Detailed presentations of a vaporizer system (left) and a whole liquid delivery system (right) from an US-patent by Li *et al*. [10]. Example of the possible complexity of the DLI devices.

Not all materials can be deposited with a normal thermally activated ALD reaction. For example, single-element metals and nitride films often require high energies which can be created with plasma-enhanced ALD (PEALD). It operates like a normal ALD reactor but provides additional energy in the form of plasma to the reaction during some step on the ALD-cycle. PEALD enables lower deposition temperatures and different precursors than

thermal ALD while maintaining high growth rate and excellent quality of the deposited film. Depending on the plasma reactor’s configuration, plasma can introduce different kinds of high-energy particles like ions, electrons and radicals to the reaction. There are three general categories for PEALD reactor types. In radical-enhanced ALD, the plasma source is added into a normal ALD reactor so the plasma species must flow in the tubes to reach the reactor which causes it to lose ions and electrons introducing only radicals to the reaction. Direct plasma ALD places the substrate on one of the plasma electrodes which enables very high energies and can even cause damage to the substrate. The last configuration is remote plasma that generates the plasma remotely from the substrate but still close enough to produce some ion and electron flow to the substrate compared to radical-enhanced plasma. Having a separate plasma setup, it is possible to control the properties of the plasma independently of the substrate. There are also other types of special ALD like atmospheric pressure ALD but their usability is limited. [5,11,12]

2.3 Materials

In general, ALD can be used on all substrates that have required surface chemical species to bond with precursors and do not decompose on ALD temperatures. The most common substrates are silicon wafers, used in electronics, but also glass and sapphire wafers are frequently used. Depositions have also been done on numerous of different substrates including wood, bamboo, cloth and fabrics. Development of low temperature ALD has also made it possible to deposit thin films on various polymers such as poly(methyl methacrylate) (PMMA) and polyvinyl chloride (PVC). It is essential to have a clean substrate because any impurity on the surface will most likely work as a growing point which will lead into island type of growth. Also, it is good for a substrate to have a flat defect-free surface to achieve stable growth and good film quality.

The first requirement for a precursor is being volatile enough to provide a sufficient amount of reactive gas flow to the substrate and saturating the surface. Low volatility can be solved with high processing temperatures and long cycle times but these can cause new problems. Reactants need to be able to adsorb chemically to the surface of the substrate in a self-terminating manner but also react with the other co-reactant at the deposition temperature. Thermal stability of the reactants is also of importance because

precursors might otherwise decompose too early and react differently with the substrate which could lead to CVD kind of surface reactions.

Materials grown by ALD include oxides, nitrides, sulphides, selenides and pure elements like metals. Oxides are by far the most researched of the materials which might be partly because they are usually deposited from easy oxygen sources such as water vapor, O_2 and O_3. The deposition of pure elements often requires high temperatures or a plasma source but at least Ti, Fe, Co, Ni, Cu, Mo, Ru, Pd, Ta, W, Ir, Pt, Al, C, Si and Ge have been grown with varying success. Additionally, almost all metals, with the exception of some alkali metals, have been grown as compounds. [4,13]

Nowadays, organic molecules are also used in depositions called molecular layer deposition (MLD). The process is very similar to ALD but using organic molecules. Combining ALD with MLD enables completely new types of inorganic-organic hybrid thin films which can have very different characteristics compared to normal purely inorganic counterparts. Especially so, because inorganic-organic thin films can be deposited to complex structures like superlattices and nanolaminates which bring new functionalities to the material. Superlattice is a very thin layer of a material between thicker layers of another material and nanolaminates are thicker layers of the two materials on top of each other. It is also possible to remove the organic material from a deposited thin film to achieve several 3d-structures. The combination of organic and inorganic molecules into hybrids makes it possible to exploit the best properties of both. For example, flexible electronics can be fabricated by using elastic organic molecules to bring flexibility and inorganic molecules to bring the electronic abilities. [14,15]

The most common organic molecules used in hybrid thin films are alcohols and phenols but other molecules like acids are also used. Purely organic thin films have been made with MLD from various organic molecules such as polyurea, polyamides and –imides. Organic molecules are significantly different to inorganic ones. Most notably, they usually have long chains which can cause steric hindrance and can bend on a surface to react again with the surface. Often, they also suffer from low vapor pressures and can even diffuse inside the thin film. Therefore, the deposition of organic molecules is more difficult and usually much slower because of longer exposure times. [14,15]

2.4 Thin films

As all atomic layer depositions produce thin films, it is necessary to give a short introduction to thin films and clarify how they differ from bulk material. A thin film is a layer of material with a thickness in scale of less than a nanometer to few micrometers which means that the dimensions are near the scale of room temperature quantum effects such as quantum tunneling. The surface area of a thin film is usually large compared to its size which makes surface effects such as surface scattering of electrons important. In contrast to bulk materials, thin films are not as dense and can even be more porous which can cause long-term problems such as absorption of humidity and oxidization of the material. For example, porous ZnO thin films are used for gas sensing and light scattering [16]. [17]

Many properties of a thin film are thickness dependent which is also one of the reasons why the accurate thickness control of ALD is so important. For example, resistivity, thermal expansion and refractive index coefficients are related to thickness. Moreover, the structure of the material can change according to thickness: very thin films can be amorphous and thicker films of the same material can be polycrystalline. The structure of the film can also be affected by the choice of substrate. The substrate can induce a structural change near the interface between the materials (substrate-induced phase, SIP) but the SIP might not cover the whole thickness of the film. For example, in study by Ghosh *et al.* the resistivity of ZnO thin films depended on the stresses caused by substrate [18]; More stress the substrate induced, the more electrical resistivity there were. [17,19]

Different deposition methods cause differences on films. In practice, the difference of physical and chemical depositions is significant; the first relies on physical means of creating the deposited vapor and the other is based on chemical reactions and formation of chemical bonds. Logically this influences the structure of the deposited material. For example, Ong *et al*. compared the differences of physical and chemical vapor deposition in the case of a MOSFET's high-k gate dielectric [20]. They deposited tungsten silicide (WSi_2) with both methods in different thicknesses and compared their properties. The performance of chemically deposited WSi_2 film was significantly better in properties such as drive current, maximum transconductance and maximum effective mobility. These improvements were attributed to incorporation of passivating fluorine atoms into the WSi_2 dielectric layer during the chemical vapor deposition and to better interface quality.

There are also different growth modes for thin films; they can either grow optimally layer-by-layer or the growth may concentrate on certain “islands” that will eventually grow together as the islands spread. The deposited film may also be amorphous and crystallize on certain growth stages or after annealing. Usually, single crystal thin films grown on crystalline substrate, so called epitaxial growth is pursued.

Thin films are most commonly utilized in state of the art electronics such as microprocessors, light-emitting diodes (LEDs) and lasers because thin film deposition techniques allow large scale production while maintaining very precise control on composition of the films. Current high-level lithography techniques can achieve details of around 10 nanometers but such devices have not been commercialized yet. For example, the biggest semiconductor companies, Intel and AMD, currently market 14 nm technology.

3 Ternary oxides

Before going in to the nickel manganese oxides, it is good to introduce the wider topic of ternary oxides in which the nickel manganese oxides belong. Ternary oxides are defined as compounds that contain two different elements in addition to oxygen. The definition is not completely strict; for example, there is no clear distinction between an element being considered a dopant or a component of a multiple oxide since dopant percentages in oxides are often quite high. Perhaps, the most notable and researched structures of ternary oxides are the perovskites (ABO_3) and spinels (AB_2O_4) but there are numerous of other interesting structures such as trirutiles (AB_2O_6). A lot of study is being done on ternary oxides for numerous applications and new compounds and better synthetization methods are constantly searched.

Ternary oxides are intriguing because of their inherent physical and chemical properties e.g. ferroelectricity and ferromagnetism, which can be utilized in different applications. Each of the elements can introduce new properties to the oxide. The stoichiometries of the elements in ternary metal oxides can be tuned allowing precise control of many electrical properties such as bandgap, conductivity and dielectric constant. In addition, the ions in ternary metal oxide can exist in multiple different valence states making the material excellent for electrochemical devices utilizing reduction and evolution reactions. For example, fuel cells and supercapacitors are among most researched areas in functional material chemistry. [21,22]

Quaternary oxides are investigated for similar reasons as ternary oxides since the additional element brings more functionalities and allows further tuning of the material. Likewise, quaternary oxides are more difficult to synthesize and control accurately than ternary oxides. A good example of a well-researched quaternary oxide is indium gallium zinc oxide (IGZO) that is used as a material for transparent amorphous-oxide semiconductor thin film transistors (flexible displays). Gallium was introduced to the original indium zinc oxide (IZO) material to control carrier concentration and to increase the stability of the material with the high bonding strength of gallium. [23]

3.1 Perovskite structure

Perovskites are one of the most studied materials in chemistry and the perovskite structure could possibly be the most abundant structure found on Earth's mantle. Nowadays, about 30 different perovskite or perovskite-like structures have been deposited with ALD [24]. There are numerous interesting applications for perovskites ranging from superconductors to solar cells. Even though manganese and nickel have not been found to form perovskite oxides, perovskite structure is an essential part of ternary oxides and deserves its own subchapter. The spinel structure and other structures found in nickel manganese oxides are introduced in the next chapter.

The perovskites have the structure of ABX_3 where A and B are cations and X is the bonding anion, Figure 6. In the case of perovskite oxides, the X is always an oxygen atom. In an ideal cubic structure, the larger sized A-cations locate on the corners and B-cations reside on the body-centered positions while the X-anions are on the face-centered locations. Most perovskites do not have the ideal structure but are distorted in different ways. The perovskite structure can easily distort to occupy different sized atoms; it can expand, contract, tilt or curve. Additionally, it is possible to partially substitute any of the three components of the perovskite or create vacancies into the structure. This enables the usage of different elements to fine-tune the properties of the perovskites. [25,26]

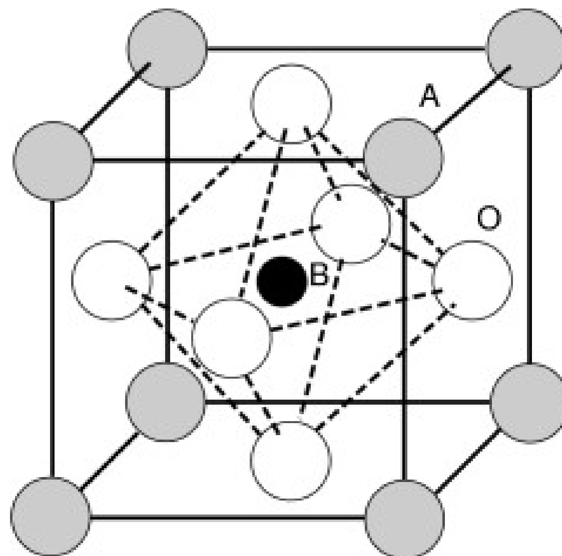

Figure 6. The ideal cubic perovskite structure illustrated by Ito *et al*. [27]

Also, there are more complex perovskite structures called superstructures. These structures have some of their atoms replaced by different elements. For example, a structure with half of the A or B locations filled with different atoms is called A or B site substituted perovskite. The substitution of the elements can happen with different orderings: it can form layers consisting of substituted elements or the substituted element can be evenly distributed into the lattice. Substitutions can bring new functionalities to the material and the substitutions usually cause some distortion to the lattice because the substituted atoms can be of different size than the originals. [25,26]

One important type of distortion in the perovskites is the Jahn-Teller effect (JTE). The Jahn-Teller effect is strongly related to transition metal chemistry because of their partially filled d-subshell and octahedral coordination of the B cations. In a perfect octahedral coordination, the d-orbitals are split in three degenerate t_{2g} and two degenerate e_g orbitals but for some electron configurations such as d4 and d9 it is often energetically beneficial to reduce degeneracy by lowering the symmetry through tetragonal distortion. Another notable distortion in perovskites is the shifting of the B cation, which is the cause for ferroelectricity in perovskites; the B cation shifts off-center to a lower symmetry phase below the Curie temperature producing an electric dipole. [28,29]

3.2 Applications for ternary oxides

In this subchapter, the various applications for ternary oxides are presented. In addition, the origins of functionalities present in the applications are discussed.

One major field for ternary oxides is in optoelectronics. In short, optoelectronic devices are used to create an electrical signal induced by optical phenomena or vice versa. Light-emitting diodes (LEDs), photodiodes (solar cells), liquid crystal displays (LCDs), photoresistors and lasers are good examples of optoelectronic devices. The possibility to tune the bandgap by varying the stoichiometry makes ternary metal oxides very compelling for optoelectronics. Other important properties include good conductivity, crystallinity and smooth interfaces between the materials so there are no carrier-transport barriers. It may be difficult to fabricate such ternary oxides but it can be

achieved with careful choice of materials and correct chemistry used. Nowadays, transparency and flexibility of the material are particularly important factors because of the demand of modern electronics. [21,30]

Indium tin oxide (ITO, In_2O_3:SnO_2) is an excellent example of a ternary oxide used in optoelectronics and also one of the most utilized ternary oxides in commercial applications. The most important applications for ITO are transparent conductive coatings for displays and thin film photovoltaics. The excellence of ITO stems from its high conductivity, refractive index of two and transparency in thin film form. In addition, the deposition of ITO is well known and the depositions produce uniform crystalline films. ITO can be doped and mixed with different elements to induce different properties. For example, Sawada *et al*. deposited ITO (40 nm) / Ag (15 nm) / ITO (40 nm) sandwich that showed high transmittance but very low resistance and high conductivity [31]. The resistivity decreased by 93 % with the insertion of the 15 nm silver layer compared to pure ITO with same thickness. In recent years, the prices of indium have risen because of its rarity and high usage in LCD-panels so research for replacing materials is on-going. Ternary oxides such as Cd_2SnO_4, $ZnSnO_3$, $CuAlO_2$, AlZnO, and $GaInO_3$ have been developed and the indium in ITO has been partly replaced with other elements such as zinc. [32–34]

Perovskite oxides are largely studied to replace the standard electrolyte materials of solid-oxide fuel cells (SOFC). Normal SOFCs operate by conducting oxygen ions through the electrolyte but there are also cells that work by conducting protons (H-SOFC). It is theorized that the proton-diffusion in perovskites is based on thermal vibrations of the BO_6 octahedral which leads to fluctuations around the O-atoms briefly changing the distance between two adjacent O-atoms and allowing a proton to overcome the potential barrier and to hop to next O-atom. Similarly, the fluctuations can break O-H bonds allowing the proton to bond to another O-atom. As said, current technology SOFCs use ceramic electrolytes that conduct oxygen ions such as yttria-stabilized zirconia (YSZ). The major drawbacks of the current electrolytes are the high temperatures required (over 800 °C) to get adequate conductivity and the chemical instability of the electrolyte. Yttrium-doped barium zirconate (BZY, Y:$BaZrO_3$) has gained a lot of attention as one of the most potential replacements because of its good chemical stability and high bulk ionic conductivity in much lower temperatures. The problem of BZY has been its high resistance at interfaces that is caused mostly by the grain boundaries along the other materials. Bae

et al. recently demonstrated that these problems can be resolved with careful optimization of the boundaries and using the correct deposition methods [35]. They managed to reduce the pore and grain sizes of the anode to make it flatter and to improve the physical integration with the electrolyte. In addition, they deposited anode functional layers to improve the interfaces of the material and they managed to make a thin (100 nm) but dense BZY film with a columnar microstructure. The fabricated SOFC, illustrated in Figure 7, provided a maximum power density of 740 mW/cm^2 at 600 °C which is good value for such a low temperature cell and the record for BZY-based SOFCs. [35–37]

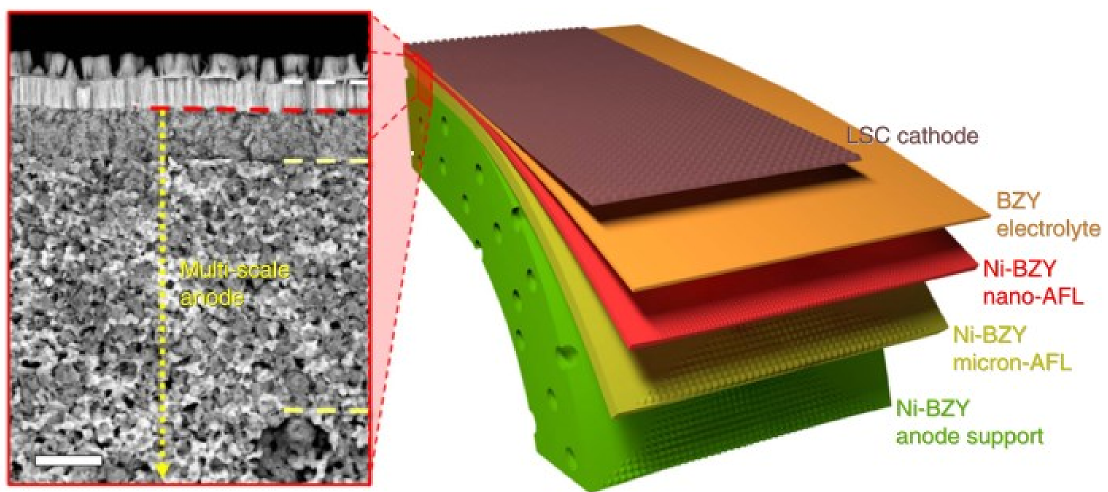

Figure 7. Cross-sectional SEM-image and a schematic picture of the BZY SOFC fabricated by Bae *et al*. [35]

Supercapacitors are also a potential application for ternary oxides. Supercapacitors are electrochemical energy storage devices which cycle energy faster than batteries while containing more energy than normal electrostatic capacitors being in the middle in properties. Important material properties for supercapacitors include high cycling life, good capacitance and fast charge-discharge kinetics. In general, ternary oxides are stable and cheap to produce and also provide good capacitance with high energy density. The kinetics and cycling stability of the ternary oxides can be improved with nanostructuring for example by decreasing the particle size and inducing pores to the structure which enhance the specific surface area. Most researched ternary oxide supercapacitors materials are XCo_2O_4 with spinel structure and $XMoO_4$ (X = transition metal). Especially nanostructured $NiCo_2O_4$ and $CoMoO_4$ materials have been proven to perform well. For

example, Mai *et al*. fabricated hierarchical $MnMoO_4/CoMoO_4$ structure where $MnMoO_4$ nanowires worked as the substrate or backbone for the $CoMoO_4$ nanorods [38]. This increased the Brunauer-Emmett-Teller (BET) surface area from 3.17 m^2/g (pure $MnMoO_4$) to 54.06 m^2/g. Furthermore, the capacity of the nanostructured composite material was higher compered to each nanostructured material alone which was attributed to decreased self-aggregating and high contact areas between the materials. The $MnMoO_4/CoMoO_4$ material showed excellent cycling efficiency of 98 % after 1000 cycles and exhibited specific capacitance of 187.1 F/g at 1 A/g. [22,39]

Ternary oxides have gained a lot of interest as possible replacements for SiO_2 as gate dielectric materials in metal-oxide-semiconductor (MOS) transistors. Modern electronics have surpassed the properties of traditionally used SiO_2 because gate dielectrics are getting to thicknesses around one nanometer where SiO_2 starts to leak substantial currents and electron tunneling poses a threat. Therefore, dielectrics with higher dielectric constants than SiO_2 (called high-κ dielectrics) have been manufactured to get higher capacitances with less current leakage. Silicon dioxide has a dielectric constant of only 3.7 – 3.9 in contrast to HfO_2 and ternary rare-earth oxides which have dielectric constants with values over 20. Rare-earth ternary oxides also have other good properties for dielectrics such as large band gap and a band offset to silicon, and in addition they withstand high processing temperatures without deteriorating. Toleration of high temperatures is important in fabrication of MOS transistors because after the production of the dielectric layer there are additional steps such as doping which require high temperatures. For example, thin film scandates such as $LaScO_3$ and $GdScO_3$ are among the most extensively researched materials in the field but others such as $CeHfO_2$ and $LaZrO_2$ have also displayed promising results. [40–42]

Another notable application for ternary oxides is titanium-sapphire lasers which normally use crystalline $Ti{:}Al_2O_3$ (doped binary oxide) but also doped ternary oxide crystals such as $Nd{:}YVO_4$ and $Nd{:}Y_3Al_5O_{12}$ are used in similar kind of laser. The lasers are widely used in research because their wavelength can be tuned and they are able to generate very short light pulses. [43]

One important material to mention is the perovskite $SrTiO_3$ (STO). It has been widely researched for numerous applications because of its anomalous properties. It has very high dielectric constant and specific resistivity yet it can be made conducting with doping

thus making it an excellent substrate for superconductors, perovskite oxides and many other oxides [44]. In addition to being good substrate, it has also been studied in the field of thermoelectrics [45], room-temperature ferroelectrics [46] and magnetism [47]. Some of the abnormal properties of STO come from the interfaces formed with other materials, especially with other perovskites. It is theorized that STO forms an exotic two-dimensional phase of electron matter at the interface called 2d electron gas (2DEG). [48]

3.3 Problems associated with ALD of ternary oxides

Even though many of the currently researched ternary oxides are thin films fabricated with ALD, there are many unknowns to how the deposition is actually happening. Usually, there is no clear “ALD-window” for ternary oxides as the growth can be non-linear with different pulse ratios but often some kind of correlation between the pulse ratios and the composition of the film can be found. The non-linearity of the ALD is also the reason why the stoichiometries of the elements can be difficult to control accurately. Sometimes deposition leads to a solid solution, sometimes real ternary phases are formed. The reaction mechanisms or other atomic-level details for the ALD of ternary oxides are not completely known so it is not fully resolved why the non-linearity happens. There are many possibilities for the anomalies such as different mechanisms in early and steady growth, stepwise surface decomposition of the precursor, changes in oxidation states and so on. For example, a mechanism has been proposed for an ALD process utilizing β-diketonate precursors and ozone oxidizer in which some of the ligands are eliminated during the second precursor pulse instead of being completely eliminated by the ozone pulse. This would mean that the process is kind of a mixture of CVD and ALD techniques because the precursor react partly together on the surface of the substrate. [49,50]

The growth rates of the elements in ternary oxides can deviate a lot as some elements grow multiple Å per cycle and some grow less than one Å which is less than a mono-layer of atoms. Such strong digression in the GPC makes it difficult to control the stoichiometry. Furthermore, the characteristics and properties of binary and ternary thin films differentiate largely from one another meaning that conclusions about ternary materials should not be made solely based on binary depositions. One significant problem in the ALD of ternary oxides is caused by the precursor chemistry as the oxide materials can be

deposited from numerous precursors which have different processing conditions. Most important parameters are the deposition and sublimation temperatures: a too low deposition temperature will inhibit growth but also increase the hydrogen and carbon impurities caused by the precursors and a too high temperature will cause decomposition of the precursor materials which leads to uneven film growth. In addition, deposition temperature can have an effect on the surface and interface roughness of the thin films. [49,51]

The precursor chemistry is also important because some precursors have very low thermal stability as some precursors require high processing temperatures which makes it difficult to combine these precursor in an ALD process. In addition, some precursors oblige the usage of strong oxidant (O_3) which can cause issues such as decomposition of the surface of the film and creating undesired interfacial layers. Volatility and sufficient vapor pressure of the precursor are also important factors in ALD and one of the possible problems in the ALD of ternary oxides. However, these problems can be solved with adequate reactor design using DLI systems, bubblers and heaters. Tubular type ALD reactors are particularly vulnerable to have heating problems with precursors because the precursors and the reaction chamber are a part of a single heating system which need to be carefully heated to a certain heat gradient. This means that the precursors cannot have big differences in their sublimation temperatures and that the temperature of the reaction chamber cannot widely exceed the sublimation temperatures. [24,52]

The surface chemistries of the substrates have a considerable effect on the thin films deposited on top. Particularly so in the cases of ultrathin films and applications that require high purity films. Additionally, perovskite-perovskite interfaces show exotic properties such as superconductivity. In these cases, single crystal perovskite substrates such as STO are used. Commercial perovskite substrates are carefully cut along a crystallographic direction to endorse epitaxial growth of certain kind. In addition, the surfaces of the substrates need to be chemically terminated (etched), annealed in high-temperatures (~1000 °C) and mechanically polished. Even small misalignments can lead to major crystallographic errors. It is also possible to support the growth of certain nanostructures through accurate surface control. [53]

4 Nickel manganese oxides

This chapter presents different nickel manganese oxides, their basic properties, and common applications. Three distinct structures (spinel, ilmenite, and murdochite) of nickel manganese oxides are introduced from which the spinel structure is clearly the most researched one. In addition, the basic properties of nickel and manganese are discussed and later on in the chapter the various deposition and synthetization methods for the different nickel manganese oxides are given. Also, practical applications of the nickel manganese oxides are introduced. Because ALD of nickel manganese oxides has not been reported in literature, the atomic layer deposition of nickel and manganese oxides is discussed and can work as a good starting point for the ALD of Ni-Mn composite.

Nickel manganese oxides have been widely studied all the way from the first synthesis of $NiMn_2O_4$ in 1957 [54]. On the early days, most of the interest came from magnetic properties of the system's spinel structure (AB_2O_4) but later on these oxides have been researched as potential charge storage electrodes and as new materials for oxygen evolution and reduction reactions (OER/ORR) with other transition metal oxides (TMOs). Both nickel and manganese are first-row transition metals having a partially filled d sub-shell. The partially filled d shell causes most of the interesting properties of transition metals such as paramagnetism, coloured compounds, and numerous oxidation states. The detailed electron configuration of manganese is [Ar] $3d^5$ $4s^2$ and the structure of nickel is described in literature either as [Ar] $3d^8$ $4s^2$ or [Ar] $3d^9$ $4s^1$. [55]

Nickel manganese oxides differ from other TMOs with nickel's and manganese's distinct characteristics. Manganese is cheap and abundant, non-toxic, shows excellent pseudocapacitive properties as oxide, is chemically stable, and has many possible valences enabling a multitude of different reactions. Nickel has a high theoretical specific capacitance value, is naturally magnetostrictive, and for example provides strength and hardness in compounds. Magnetostrictive materials change their dimensions in a changing magnetic field and pseudocapacitance is material ability to store electrical energy with electron charge transfer inside the material. The nickel manganese composites can have very distinct properties diverging largely from the single component's features. For example, Liu *et al.* resolved that the bulk mixture of nickel and

manganese oxides has a higher specific capacitance than either of the materials as sole, represented in Figure 8 [56]. [57]

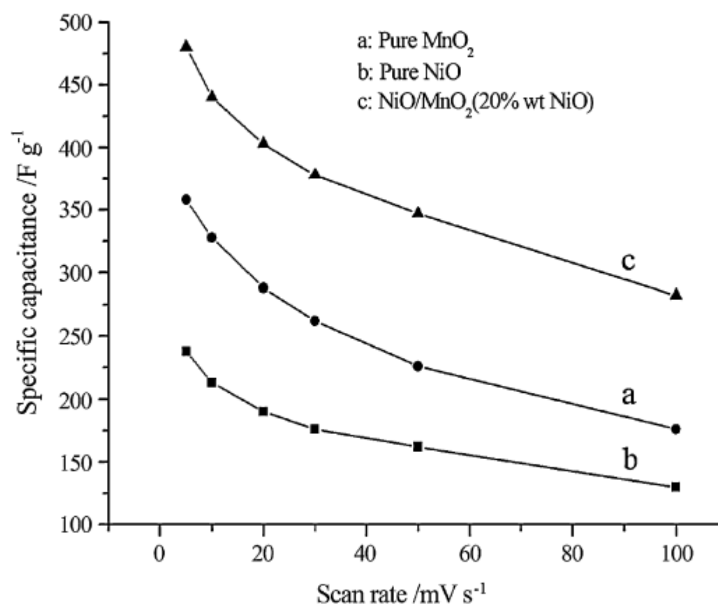

Figure 8. Comparison of specific capacitances plotted against scan rate of pure oxides and their composite mixture [56].

Nickel has four common oxidation states Ni^0, Ni^+, Ni^{2+} and Ni^{3+} of which 2+ is the most common one. Nickel has five stable isotopes from which ^{62}Ni which has the highest nuclear binding energy of all nuclides and the most abundant isotope is Nickel-58. On the other hand, manganese has common oxidation states from 0 to +7 from which Mn^{2+} is the most stable state. Manganese has only one stable isotype which is Manganese-55.

Temperature programmed reduction studies under hydrogen atmosphere have been conducted for both manganese and nickel oxides and for the spinel and ilmenite forms of nickel manganese oxides [58]. Christel *et al*. concluded from their study that manganese oxides successively reduce to less oxidized oxide (MnO_2 -> Mn_2O_3 -> Mn_3O_4 -> MnO) but contrariwise the manganese ion in nickel manganese oxides went directly from Mn^{4+} to

Mn^{2+} and Ni^{2+} was reduced to metallic nickel. The difference was believed to be caused by the promoting effect of nickel which increased the number of nucleation sites and accelerated the reactions preventing the less oxidized states on manganese. Few separate research groups have calculated phase diagrams for Mn-Ni-O system over years with some major differences. The newest calculations have been done by Kjellqvist and Selleby with the CALPHAD method in 2010 and their versions of the phase diagram are presented in Figure 9 among results from other research groups [59].

As can be seen from the Figure 9, multiple phases for nickel manganese oxides exists. In temperatures under 1000 K the murdochite structured Ni_6MnO_8 is composed when the amount of manganese is less than 15 % and ilmenite structured $NiMnO_3$ forms when there's 15 – 50 % of manganese. In higher manganese contents the structure changes to spinel; $NiMnO_2$ is synthetized in temperatures below 700 K and $NiMn_2O_3$ is fabricated between 700 – 1000 K. Higher temperatures than 1000 K will lead to additional phases and different ionic configurations but they are not relevant in case of ALD.

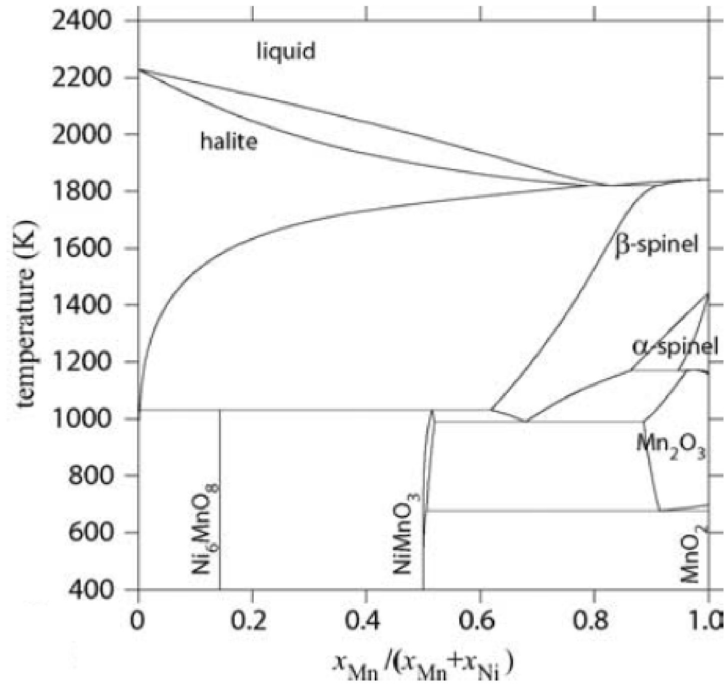

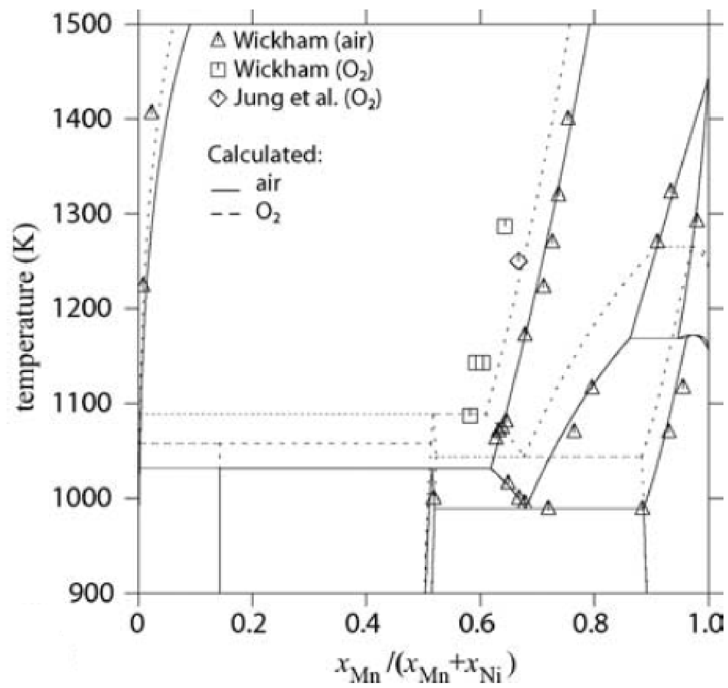

Figure 9. Phase diagrams of Mn-Ni-O with temperature in Kelvins on y-axis and the proportional amount of manganese on x-axis. Top: calculated in air by Kjellqvist and Selleby, bot: experimental data from other sources. [59]

4.1 Spinel: $Ni_xMn_{3-x}O_4$

$Ni_xMn_{3-x}O_4$ (where $0 \le x \le 3$) thin films have been studied at least from the early years of the 1990s. These manganese nickel oxides have been interesting because of their negative temperature coefficient (NTC) and semiconductivity which enabled their use in wide range of electronic applications such as bolometers (and thermistors (resistance depends on temperature). The properties of $Ni_xMn_{3-x}O_4$ are highly dependent on the fine structure of the material and they can differ a lot between bulk and thin film forms. For example, the resistivity of the thin films is higher than the resistivity of bulk material. It is more difficult to control the fine structure of the material in bulk form which also makes the reproducibility quite hard. Consequently, research is nowadays mostly based on thin films. [60]

The crystal and the electronic structures of $Ni_xMn_{3-x}O_4$ have been widely studied but there is no widely accepted explanation what causes the functionalities of the material. It is definitely a cubic spinel when $0.4 \le x \le 2$ and a tetragonal-distorted spinel when x is near zero due to the cooperative Jahn-Teller effect. The cubic version is said to have at least 10 times higher conductivity but the tetragonal material is more thermally stable. It has been reported that the $Ni_xMn_{3-x}O_4$ system has minimum resistivity at $x = 0.75$ [61]. It is suggested that all Mn^{2+} species are on the tetrahedral sites of the spinel and Mn^{3+}, Mn^{4+}, and Ni^{2+} would locate on the octahedral sites. Also, a structure where some of the Ni^{2+} and Mn^{3+} ions are located on tetrahedral sites is proposed based on neutron diffraction studies and on the good conductivity of the material [62]. The spinel is of inverse structure with inversion parameter varying around 0.7 - 0.95 depending on annealing temperatures and cooling rates. It’s mentioned in the literature that stability of the electrical properties of the material can be dependent on the inversion parameter [63]. Structure of the cubic spinel is displayed in Figure 10. [58,64]

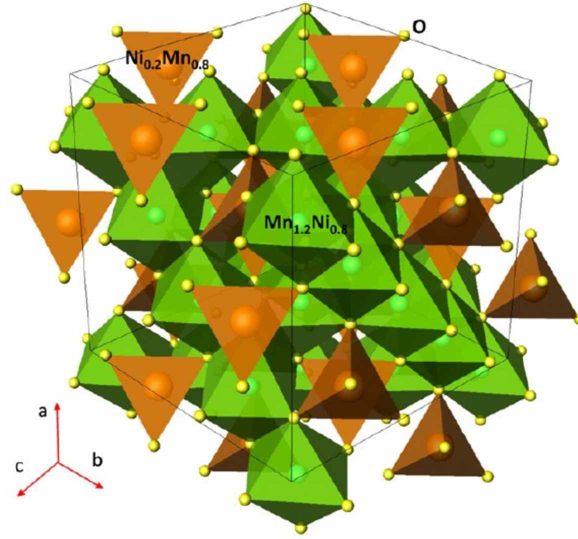

Figure 10. Cubic spinel structure of $NiMn_2O_4$ along the 111 plane. [65]

The electronic properties of the material are usually explained by thermally activated localized electron hopping between nearby Mn^{3+} and Mn^{4+} ions, also called the small polaron hopping model. In short, the polaron is caused by a charge carrier's ability to deform the surrounding lattice because of natural repulsion and attraction of different charges and the resulting trapping of the electron [66]. Basu *et al.* performed *in situ* studies with scanning tunneling spectroscopy for thin film $Ni_xMn_{3-x}O_4$ and concluded that their observations support variable range hopping model for conductivity of Shklovskii and Efros (ES-VRH), not the model of Mott [67]. According to ES-VRH theory, conductivity can be calculated from:

$$G \propto \exp(-\sqrt{\frac{T_{es}}{T}}) \quad (1)$$

$$T_{es} = \frac{\beta e^2}{\kappa k_B \xi} \quad (2)$$

Where β is the numerical constant of the order of unity, κ is the dielectric constant, and ξ is the localization length. [68]

It is also possible to dope nickel manganese's spinel structure to introduce different properties. Elements such as Cu, Zn, Fe, Co, Mg, Ti and Al have been successfully incorporated to the structure in different amounts. The dopant replaces one Mn^{3+} ion which in turn causes one Mn^{3+} ion to convert into Mn^{4+} ion to maintain the electrical neutrality. Thus, the number of Mn^{3+}/Mn^{4+} pairs change as well as the electrical properties of the material change. For example, doping with Cu reduces and doping with Ti increases the resistance of nickel manganese. [59,69]

As most spinel materials, $NiMn_2O_4$ is ferromagnetic. The Curie temperatures reported for bulk $NiMn_2O_4$ vary between 122 K and 145 K but some structures can go as low as 72 K [70]. The Curie-Weiss temperatures also diverse largely: Peña *et al*. calculated it to change from -86 K for $NiMn_2O_4$ to -245 K for Ni_2MnO_4 indicating strong antiferromagnetic interactions in the samples [71]. In addition, using the reverse micellar method with different combinations of surfactants they obtained different nanostructures of $NiMn_2O_4$ (different sized nanorods, cuboidal, hexagonal, and spherical nanoparticles) which showed varying magnetic behavior. For example, the magnetic susceptibility was almost five times larger for anisotropic nanostructures compared to agglomerated nanostructures.

4.2 Ilmenite: $NiMnO_3$

Even though $NiMnO_3$ has been synthetized and characterized roughly the same time as the spinel $NiMn_2O_4$, no widespread applications have been found for it [72]. The only researched practical usages for the ilmenite nickel manganese oxide have been in supercapacitors and in catalyzing oxidation reactions in which it can perform better than either nickel or manganese oxides because of the high oxidation state of +4 in Mn-ions [73]. The structure of $NiMnO_3$ is ilmenite, shown in Figure 11. In detail, the structure consists of alternating magnetic Ni^{2+} and Mn^{4+} hexagonal phases which cause the material to be ferromagnetic similarly to Fe_2O_3. All the manganese and nickel in the ilmenite are in Mn^{4+} and Ni^{2+} forms on the octahedral sites. The ilmenite structure is close to the

perovskite structure presented in chapter 3 having the same ABX_3 formula but the ilmenite structure is hexagonally packed instead of cubic packing in perovskites. [74,75]

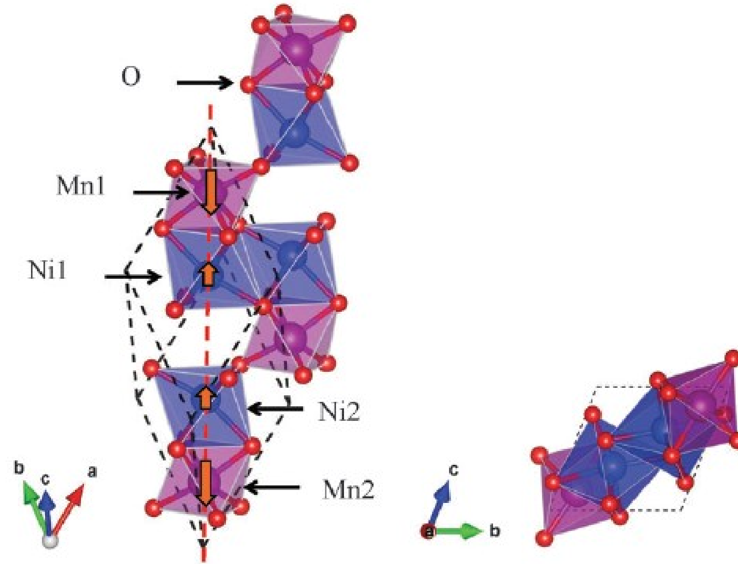

Figure 11. Structure of ilmenite $NiMnO_3$ illustrated by Yu *et al.* [76]. The differently aligned hexagonal magnetic phases are marked with arrows.

4.3 Murdochite: $Ni_{6+2x}Mn_{1-x}O_8$

Nickel manganese oxide $Ni_{6+2x}Mn_{1-x}O_8$ and the common form Ni_6MnO_8 (hexanickel manganese oxide) have seen very little research compared to other nickel manganese oxides even though they have been synthetized and studied more than 20 years ago [77]. The research on hexanickel manganese oxides has been mainly focused either on the determination of their electrical and magnetic properties or evaluation of their potential as a catalyzer in oxidation and decomposition reactions. Also, the Ni_6MnO_8 structure with the addition of magnesium has been studied [78,79]. In many cases, hexanickel manganese is one of the many phases seen in mixed nickel manganese oxides.

$Ni_{6+2x}Mn_{1-x}O_8$ has the structure of murdochite (Figure 12) when $0 \leq x \leq 0.8$ and the structure of basic rock-salt (Fm-3m) when x is close to one. The transformation from rock salt to murdochite structure happens by replacement of Ni^{2+} ions with Mn^{4+} ions and

cationic vacancies. According to Taguchi, the 4a positions of the lattice are occupied by Mn^{4+} and Ni^{2+} ions and the 4b position is occupied by Ni^{3+} ions and vacancies [80]. The increase in x shows as an increasing amount of Ni^{3+} ions and less vacancies on the 4b position. The Ni^{2+} and Mn^{4+} ions are both octahedral coordinated by six oxygen ions. Taguchi determined that $Ni_{6+2x}Mn_{1-x}O_8$ exhibits highest electrical resistivity and Seebeck coefficient at x = 0.8. In addition, based on the conductivity measurements he adds that $Ni_{6+2x}Mn_{1-x}O_8$ follows the hopping conductivity in the small-polaron model similarly as $Ni_xMn_{3-x}O_4$. Hexanickel manganese oxide is antiferromagnetic and according to Taguchi *et al*. it shows the highest degree of crystallinity after calcining in 400 °C. [80,81]

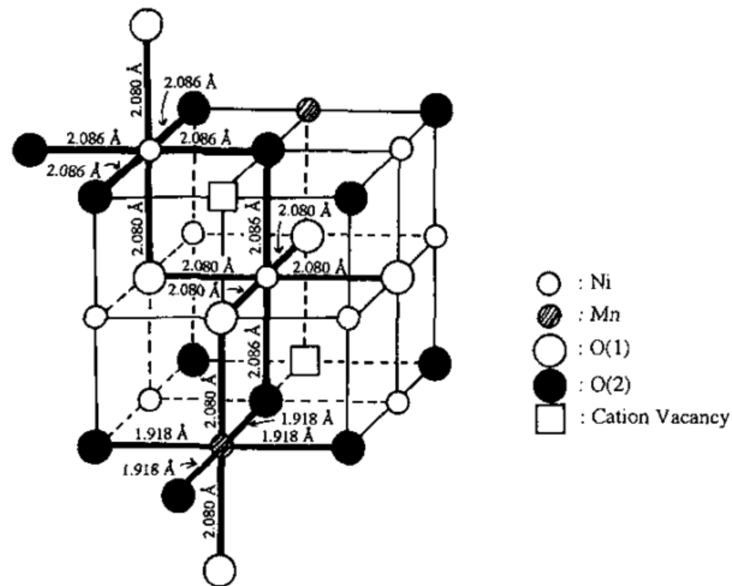

Figure 12. One-eighth of the crystal structure of Ni_6MnO_8 according to Taguchi *et al.* [79]

4.4 Synthetization of nickel manganese oxides

$Ni_xMn_{3-x}O_4$ has been synthetized with many techniques both in bulk and thin film form. The material's characteristics can change drastically between different techniques and conditions used so a short review of the fabrication methods is given. For example, Fau *et al*. report that their thin films had a much higher resistivity than bulk material and also the microstructure was notably different [61].

The first synthetizations of $Ni_xMn_{3-x}O_4$ were made with the powder sintering technique. It is possible to control the structure of sintered $Ni_xMn_{3-x}O_4$ by annealing in different atmospheres and temperatures. For example, Golestani-Fard *et al*. used a mixture of 20 wt-% of NiO and 80 wt-% of Mn_2O_3 powders and sintered them for 8 hours at 950 °C. The formed nickel manganese oxide spinel was annealed at different temperatures up to 1350 °C while measuring the bulk density and electrical resistivity of the sample. They conclude that the annealing caused significant oxygen loss from the spinel structure and caused changes in the amounts of Mn^{2+} and Mn^{3+} ions in the spinel. In addition, they state that annealing at temperatures over 1100 °C caused pore formation, loss in density, and increase in resistivity. [82]

Fritsch *et al*. studied the effect of annealing and aging in detail with sintered $Ni_xMn_{3-x}O_4$ samples using neutron diffraction experiments [63]. They found out that annealing around 850 °C caused the biggest drop (20 %) in resistivity but also that the cooling had a big effect on the structure. If the sample was cooled fast, it had some of the Ni^{2+} ions on the tetrahedral site but with slow cooling there were close to zero Ni^{2+} ions on that site. The amount of Ni^{2+} ions on the tetrahedral site changes the amount of charge carriers which in turn alter the electronic properties. The aging, usually visible as change in resistivity, of the samples was also inspected. Fritsch *et al*. concluded that metallization in oxygen atmosphere causes oxidation and defect spinel phases leading to severe aging. Aging was not observed under metallization in nitrogen atmosphere. However, a more recent article by Fang *et al*. claims that aging is influenced by the composition of the material and its thermal history [83]. Their results indicate that aging decreases with less nickel content: aging being less than 0.5 % with $x \leq 0.7$ and 850 °C annealing. They propose that the aging mechanism is caused by the change in cation distribution: First, the order is random but heating migrates the cations to their thermodynamically preferred positions.

Sintering can be combined with other techniques to create thin films by using the sintered material as a precursor target material. Datta *et al*. coupled sintering with radio frequency magnetron sputtering and studied the effect of the sputtering atmosphere on the material. First, $Ni_xMn_{3-x}O_4$ sputtering target was created from NiO and Mn_2O_3 powders by pressing them to a disc and sintering for 24 hours at 1200 °C. The magnetron sputtering was done on a custom build machine onto a Si-wafer using 2.5, 10, and 15 % oxygen

concentrations in argon atmosphere. Lastly, the films were annealed at temperatures between 600 °C and 900 °C. The films showed no difference between the oxygen ratios and the film's morphology was not changed by *in-situ* temperature cycling (from 20 °C to 200 °C and back). [60]

Sintering has also been combined with electron beam evaporation to create nickel manganese oxide thin films. Parlak *et al*. first created a Ni-Mn powder by calcining a 1:1 mixture of NiO and Mn_2O_3 powders at 900 °C for two hours. Then, the powder mixture was placed on a graphite crucible and was exposed to a beam of energetic electrons which caused the powder to evaporate and react with the substrate surface. The deposited samples were annealed in different temperatures and atmospheres which revealed that heat treatment in air or oxygen replaces oxygen deficits in the lattice and decreases resistivity. In turn, annealing in nitrogen caused further loss of oxygen that increased resistivity. [84]

Also, spin spray deposition has been used to produce nickel manganese thin films. Ko *et al*. used two solutions: a reaction solution of mixed nickel and manganese chlorides and an oxidizing solution of sodium nitrite or hydrogen peroxide and ammonium acetate or or potassium acetate. The solutions were nebulized by a nitrogen carrier gas and sprayed on a rotating substrate. The formed film was nanocrystalline and had similar electrical properties as nickel manganese oxide deposited with different methods. [85]

Nguyen *et al*. deposited nickel manganese oxides with different Ni-Mn ratios using electroplating. They used an electrolyte containing $Ni(NO_3)_2$ and $Mn(NO_3)_2$ and a stainless-steel substrate. An electric potential of -1.1 V was applied to the mixture and the samples were annealed afterwards at 250 °C for 3 hours. It was found out that small amount of manganese produced $Ni_{1-x}Mn_xO$ phases while higher concentrations generated a mixture of $Ni_{1-x}Mn_xO$ and $Ni_xMn_{3-x}O_4$ phases. In addition, different ratios produced numerous structures such as nanosheets and nanoparticles. $Ni_{1-x}Mn_xO$ nanocrystals were small sized (~2 nm) and $Ni_xMn_{3-x}O_4$ crystals were larger (~20 nm). [57]

$Ni_xMn_{3-x}O_4$ thin films have also been deposited via spin coating and chemical solution deposition (CSD). Schulze *et al*. prepared the solution for spin coating by mixing manganese and nickel acetates together with acetic acid and distilled water at 70 °C under argon atmosphere. Also, another solution route was tested where manganese acetylacetonate was dissolved into methanol and ethylene glycol at 60 °C and combined

with solution of nickel acetylacetonate dissolved in glacial acetic acid at room temperature. The combined mixture was adjusted to pH 1 and mixed for 30 min at 60 °C. Both solutions were spin coated (3000 rpm for 30 s) on Si-wafers and pyrolyzed either for 1 min at 100 °C and 3 min at 300 °C (acetate films) or 40 s at 500 °C (acetylacetonate films). Both routes produced good quality thin films which showed the spinel structure after annealing in temperatures over 530 °C. [86]

Hadj-Sadok Ouaguenouni *et al*. synthesized $Ni_xMn_{3-x}O_4$ with the coprecipitation and sol-gel methods. The coprecipitation was done by mixing manganese and nickel nitrate with sodium bicarbonate, drying the solid, and finally calcining. For the sol-gel method, nickel(II) acetate and manganese(II) acetate hydrates were separately dissolved in boiling propionic acid and then mixed together. The solvent was evaporated and the resin was calcined. Wu *et al*. report a possible hydrothermal route to create $Ni_xMn_{3-x}O_4$ but they do not mention the detailed structure of the formed oxides [87]. [88]

Hexanickel manganese oxide Ni_6MnO_8 has only been synthesized by solid-state and solution methods. The original articles behind the synthetization of Ni_6MnO_8 are inaccessible to the author of this work so only the papers describing the synthesis of pure $Ni_{6+2x}Mn_{1-x}O_8$ compounds from Taguchi *et al*. [80,81] and from Menezes *et al*. [89] are discussed here. Both groups used very similar methods utilizing nickel and manganese acetate tetrahydrate precursors for the synthetizations. Taguchi's group did it with coprecipitation method; they dissolved the acetate precursors either in water or acetic acid and the solution was mixed with oxalic acid. The liquids were evaporated by keeping the solution at 100 °C and the remaining compound was calcined at various temperatures and finally heated in 600 °C air. Menezes *et al*. used reverse micelle approach with three micro-emulsions. Cetrimonium bromide was used as surfactant, 1-hexanol as co-surfactant and hexane as lipophilic phase. Separate micro-emulsion was made for the three precursor materials: nickel acetate, manganese acetate and ammonium oxalate. The micro-emulsions were slowly mixed together and stirred overnight after which the precipitate was centrifuged, washed and dried in 60 °C. The formed nickel manganese oxalate was heated in 400 °C for 8 hours to form Ni_6MnO_8. Menezes *et al*. also synthetized Ni_6MnO_8 with same precursors using standard coprecipitation method which does not involve micelles.

Hexanickel manganese oxide has also been synthetized with coprecipitation using nickel and manganese nitrate solutions with Na_2CO_3 but the end product was a mixture of $NiMnO_3$, Ni_6MnO_8 and Mn_2O_3 [90]. Nickel manganese oxide prisms containing Ni_6MnO_8 have as well been made with almost similar method as Taguchi *et al*. but in addition to the acetate precursors nickel nitrate was added, everything was dissolved in ethanol and refluxed for 4 hours at 85 °C before drying [91]. Maeda *et al*. obtained a mixture of lithium nickel manganese oxides also containing some Ni_6MnO_8 through a two-step solid-state reaction [92]. A reaction mixture of nickel manganese double hydroxide (in different ratios obtained from a manufacturer) and LiOH was pressed in to pellets and heated in 1000 °C and 700 °C for 12 hours. The lines of Ni_6MnO_8 were seen in the diffraction patterns of nickel rich mixtures.

Ilmenite $NiMnO_3$ has been synthetized via coprecipitation [75,88,90,93] and sol-gel methods [88]. Coprecipitation synthetization by Mehandijiev *et al*. begins with nickel and manganese nitrate precursors which are added dropwise into a sodium bicarbonate solution. The mixture is then filtered, washed, and dried in 60 °C air followed with prolonged heating at 400 °C and shorter heating at 500 – 600 °C. Morales *et al*. used very similar method to create a mixture of phases containing also $NiMnO_3$ but they used sodium carbonate instead of bicarbonate and the temperatures of the drying and longtime heating were adjusted to 120 °C and 250 °C respectively. The sol-gel method of Ouaguenouni *et al*. starts by dissolving nickel and manganese acetate hydrates separately into boiling propionic acid. Once the acids are mixed together, the solvent was evaporated under constant stirring and the left-over resin was calcined in 750 °C or 900 °C air.

4.5 Applications

Today, most of research articles about nickel manganese are focused on its use with lithium as a cathode material in high-energy lithium ion batteries. Structures such as $LiMnPO_4$ and $LiM_xMn_{1-x}O_4$ (M = metal) have been widely studied and $LiNi_{0.5}Mn_{1.5}O_4$ has shown some promising results possessing high energy density with good structural and cycling stability. Other common applications include usage of nickel manganese oxides in capacitators and in OER/ORR devices. Supercapacitors are much like standard electrolytic capacitors but they offer better recyclability and faster charge delivery in addition to a

higher energy density which makes them usable as short-time backup power sources. Supercapacitors are kind of a middle ground between capacitors and batteries usable in applications that require higher energies than typical capacitors provide and rapid charge/discharge cycles that batteries could not handle. OER and ORR are opposite reactions to each other; ORR devices reduce oxygen (O_2) to, for example, water (H_2O) and OER device does the opposite which is breaking down water to form molecular oxygen ($H_2O \rightarrow O_2$). Both OER and ORR are used in many electrochemical energy conversion and storage devices such as fuel cells. For example in alkaline fuel cells (AFC), hydrogen is oxidized into H_2O at anode and oxygen is reduced with water to produce OH^- ions at cathode (ORR). [94]

It is common to use surface coatings such as AlF_3, ZnO, ZrO, or Al_2O_3 to increase stability and to further tune the electrical properties of nickel manganese compounds. Additionally, manganese oxide has been widely used as a surface coating too because of its high stability and good electrical properties. Fang *et al.* demonstrated the impact that even very thin surface coatings can produce by depositing an ultra-thin (less than 10 ALD cycles) layer of Al_2O_3 on top of a $LiNi_{0.5}Mn_{1.5}O_4$ electrode [95]. The coating increased the capacity retention of the electrode by around 10 percentage points. The effect was most likely caused by reduced overpotential on the surface and by a decrease in unwanted reactions during cycling. The excellence of surface coatings was also shown by Sun *et al*. who formed an AlF_3 layer on top of a $Li[Ni_{0.5}Mn_{0.5}]O_2$ electrode [96]. The AlF_3 coating decreased the dissolution of nickel and manganese from the electrode which contributed to an increase in capacity, better cycling performance and reduced resistance.

The performance of Li-Ni-Mn-cathodes as well as other Ni-Mn-electrodes can be enhanced with nanostructuring; structures like foams, nanosheets and nanoparticles can dramatically change the properties of the material. There are many different fabrication techniques ranging from self-aligning hydrothermal growth to the usage of templates and photolithography. Huang *et al.* excellently demonstrated the effect of nanostructuring by growing a nanosheet of MnO_2 on top of a nickel foam to compose an electrode for a supercapacitor, as seen in Figure 13 [97]. The produced structure provided maximum gravimetric energy density of 25.8 Wh/kg and power density of 223.2 kW/kg which surmounts the densities of previously reported MnO_2 based supercapacitors and typical Li-ion batteries. Layer-by-layer nanostructure has also been proven to revamp the

properties of Ni-Mn-materials: Yoshino *et al.* showed that electrochemically deposited layer-by-layer type manganese oxide/nickel oxide composite thin film had some of the superior properties of both materials such as nickel's high value of transmission and wide potential window of manganese [98].

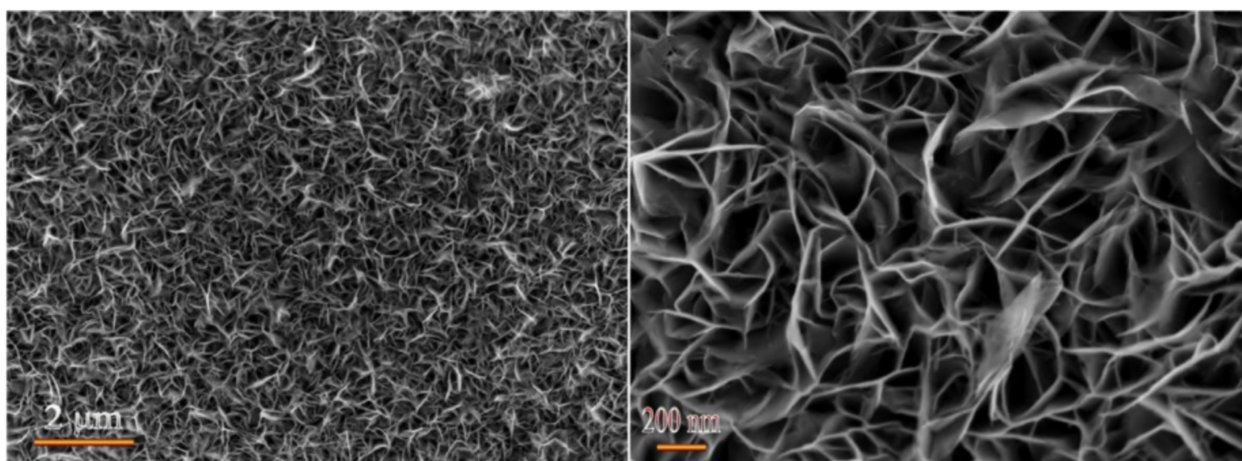

Figure 13. Scanning electron microscope picture of an electrode containing MnO_2 nanosheet on top of nickel foam. [97]

Nickel manganese oxides have seen a lot of research as different kinds of electrode materials. Usually nickel and manganese are combined with lithium to make good electrodes but electrodes containing purely nickel manganese oxides have been explored too. For example Chavan *et al*. spray deposited spinel $NiMn_2O_4$ thin films in search of new supercapacitor materials [99]. Characterizations revealed that the material is a mixture of $NiMn_2O_4$ and hausmannite Mn_3O_4 with a porous surface structure. The authors conclude that $NiMn_2O_4$ can act as an energy storage device possessing a maximum specific capacitance of 460 F/g (5 mV/s scan rate) and specific energy of 36.65 Wh/kg with excellent charge-discharge stability. There are numerous examples of lithium nickel manganese oxides being used in lithium-ion batteries [92,100–103]. The most promising material seems to be the before mentioned spinel $LiNi_{0.5}Mn_{1.5}O_4$ which provides good cycle stability and has an approximate capacity of 120 mAh/g.

$NiMnO_3$ and Ni_6MnO_8 have also been utilized as electrode materials. Kakvand *et al*. merged $NiMnO_3$ nanoparticles with graphite and reduced graphene oxide (RGO) to form

electrodes for supercapacitor applications [104]. The electrodes were made with coprecipitation method similar to earlier reported Mehandijiev's method. RGO-Ni_6MnO_8 combination worked the best providing 285 F/g (1 A/g current density) specific capacitance and good cycling stability (93.5 % after 4000 cycles). Furthermore, symmetric Ni_6MnO_8-RGO//Ni_6MnO_8-RGO –supercapacitors were tested and they showed energy density of 27.3 Wh/kg and power density 7.5 kW/kg. Similarly, Wang *et al*. added Ni_6MnO_8 nanoparticles into RGO to create an electrode for a supercapacitor [105]. RGO-Ni_6MnO_8 electrode demonstrated ultrahigh specific capacitance of ~780 F/g (1 A/g), excellent cycling stability (93.4 % after 9000 cycles), power density of 540 W/kg and energy density of 155 Wh/kg.

Additionally, Ni_6MnO_8 nanoparticles have been tested for usability in lithium-ion batteries. Alcántara *et al*. synthetized a series of $Ni_xMg_{6-x}MnO_8$ electrodes with coprecipitation method using oxalates and a test cell of Li/$LiPF_6$(EC:DEC)/$Ni_xMg_{6-x}MnO_8$. Pure Ni_6MnO_8 achieved initial capacity of ~600 mAh/g. Substituting nickel with magnesium led to decreased cell capacity but it also reduced cell polarization and facilitated the dispersion of nickel. Latorre-Sanchez *et al*. reported very similar results with their Ni_6MnO_8-graphene oxide anode measuring capacities of 400 – 600 mAh/g during first ten cycles [106]. It also mentioned that the composite material showed room temperature superparamagnetism.

Many different nickel manganese oxides are being researched for their use in ORR/OER devices. Periyasamy *et al*. demonstrated the materials' excellent urea oxidizing properties by comparing the basic oxide forms of NiO and Mn_2O_3 to their composites forms of $NiMn_2O_4$, $Ni_{1.5}Mn_{1.5}O_4$, and $MnNi_2O_4$ [107]. The materials were fabricated via hydrothermal method using nickel and manganese acetate tetrahydrates as precursor. The group demonstrated that the composite oxides had from two up to six times more electo-oxidation current than the pure nickel or manganese oxides. $Ni_{1.5}Mn_{1.5}O_4$ was the most effective in oxidation, most likely due to presence of multiple phases with different oxidation states. On the other hand, $NiMnO_3$ had superb catalytic activity in some cases such as oxidizing CO_2 and decomposing ozone. Ouaguenouni *et al*. studied the catalytic activity of nickel manganese oxides towards methane and found a substantially higher CO_2 selectivity ratio for the sample which contained a $NiMnO_3$ phase [88]. Similarly, $NiMnO_3$ was better than $NiMn_2O_4$ at catalyzing CO and benzene in the presence of ozone

which was believed to be because $NiMnO_3$ has more active surface oxygen [93]. Hong *et al*. tested the water oxidizing catalytic activity in visible light for $NiMnO_3$ and for different manganese and nickel oxides [73]. $NiMnO_3$ was the best one by far, even topping the O_2 evolution rate of Co_3O_4 which has been reported as the most active non-precious metal-oxide water oxidizing catalyst. In a recent study, He *et al*. compared the ability of nickel manganese oxides to catalyze OER & ORR [108]. Based on their results it was determined that surface Ni^{3+} ions ($NiMn_2O_4$) facilitate OER processes and Mn^{3+} and Mn^{4+} ions ($NiMnO_3$) improve ORR process. Best results in both reactions were achieved with the combination of both using mixture of 0.61 $NiMnO_3$ / $NiMn_2O_4$.

Also, nickel and especially manganese are among the common metals utilized in negative temperature coefficient (NTC) thermistors (thermally sensitive resistor). NTC thermistors are based on materials (usually semiconductor oxide ceramics) which exhibit decreasing electrical resistance when the temperature is increased. Compared to other kinds of temperature sensors NTC thermistors are very sensitive to temperature changes but also small sized, stable and reliable. For example, Le *et al*. crafted $Ni_xMn_{3-x}O_4$ microbolometers (usable for example in infrared cameras' detectors) using very low process temperature with liquid flow deposition [109]. They managed to deposit very smooth and uniform films with different compositions in very low temperatures of 30 – 80 °C. Also, the same low temperature technique worked for more complex films that have cobalt in addition to nickel and manganese [110]. Annealing in 400 °C was enough to remarkably improve the electrical properties. The authors conclude in both papers that the deposited nickel manganese oxides were good NTC thermistors with very low resistance (< 1 kΩ) and very low processing temperature (< 100 °C). The resistance was easily adjustable with the amount of doping. The best results (good NTC values and lowest resistance) came with $Ni_{0.1}Mn_{2.9-x}Co_xO_4$ thin films with 0.065 – 0.082 values for x.

4.6 Atomic layer deposition of nickel oxide and manganese oxide

Nickel(II) oxide, NiO, has been grown with various deposition methods using many different reactants. Depending on the substrate and the deposition parameters, NiO-films can be grown as epitaxial and polycrystalline films. The metallic precursors reported for NiO ALD process include cyclopentadienyl ($NiCp_2$) [111,112] and its different derivatives

such as ethylcyclopentadienyl ($Ni(EtCp)_2$) [113], the beta-diketonates such as Ni-bis-acetylacetonate ($Ni(acac)_2$) [114], Ni-bis-2,2,6,6-tetramethyl-3,5-heptadionate ($Ni(thd)_2$) [115,116], as well as dimethylglyoximato ($Ni(dmg)_2$) [114] and nickel amidinate Ni(AMD) [117]. Many of the precursors have low vapor pressures which makes it difficult to gasify them and transport them to the substrate thus requiring advanced vaporization equipment. Also, a precursor with high oxygen activity, such as O_3, may be required to get sufficient growth which may cause unwanted reactions. Although, most of these precursors have also been used with water the reactivity is substantially lower. [118,119]

Despite the fact that many of the first row transition metals are researched a lot using ALD, there are not many articles about the ALD of manganese oxides. Yet, Mn_xO_x has been deposited using few different precursor materials such as the same precursors ligands as with nickel $Mn(EtCp)_2$ [120–122], $Mn(acac)_3$ [123,124], and $Mn(thd)_3$ [125–128] but also with manganese carbonyl $Mn_2(CO)_{10}$ [129]. All precursors show saturated ALD growth but growth rates differ largely (~0.2 Å per cycle with usage of thd-precursor and 1 – 1.5 Å per cycle for the others). Both water and ozone have been successfully used as the co-reactant. Also, PEALD has been used to deposit different manganese oxides with the $Mn(thd)_3$ precursor [130]. The oxidizing/reducing potential of the used plasma reactant (H_2, H_2O, N_2, O_2, O_3, NH_3) determined the phase of the manganese oxide. MnO, MnO/Mn_3O_4 and MnO_2 thin films were deposited using NH_3, H_2, and O_3 plasma respectively. Manganese oxides phase is dependent on the growth parameters: the deposition chamber's temperature, the substrate, and the annealing temperature can all modify the phase structure of the Mn_xO_x [127,131]. For example, Nilsen *et al*. determined that ALD of $Mn(thd)_3$ produces β-MnO_2 when the temperature of the reactor is under 230 °C and Mn_3O_4 (hausmannite) at higher temperatures [125]. Similarly using $Mn_2(CO)_{10}$ as ALD precursor Jin et al. determined that below 120 °C deposition temperature produces α-Mn_2O_3 and higher temperature gives Mn_3O_4 [129].

Typically, the solid or liquid Mn and Ni precursors were kept and sublimated in relatively high temperatures of 50 - 200 °C during the depositions. The reaction chamber's temperature was between 100 – 300 °C. An increase of the reaction temperature to over 250 °C caused problems like thermal decomposition and poor adhesion to Si-wafer but otherwise the depositions were stable in the mentioned conditions. Pulse times for the

metal precursors were usually kept around 5 – 10 seconds to make sure that the whole surface is covered.

The reaction mechanisms for the ALD of nickel and manganese oxides are not fully known but the following mechanism for the reaction of $Ni(acac)_2$ with H_2O and O_3 was proposed by Utriainen *et al*. [114]

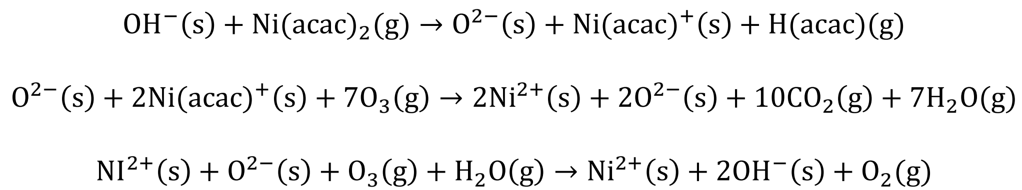

$$OH^{-}(s) + Ni(acac)_2(g) \rightarrow O^{2-}(s) + Ni(acac)^{+}(s) + H(acac)(g)$$

$$O^{2-}(s) + 2Ni(acac)^{+}(s) + 7O_3(g) \rightarrow 2Ni^{2+}(s) + 2O^{2-}(s) + 10CO_2(g) + 7H_2O(g)$$

$$NI^{2+}(s) + O^{2-}(s) + O_3(g) + H_2O(g) \rightarrow Ni^{2+}(s) + 2OH^{-}(s) + O_2(g)$$

Burton *et al.* proposed the following equation for the reaction of $Mn(EtCp)_2$ and H_2O. [120]

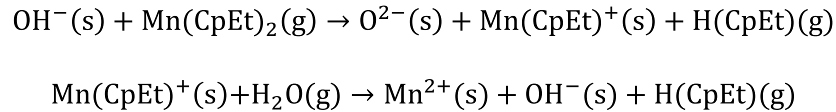

$$OH^{-}(s) + Mn(CpEt)_2(g) \rightarrow O^{2-}(s) + Mn(CpEt)^{+}(s) + H(CpEt)(g)$$

$$Mn(CpEt)^{+}(s) + H_2O(g) \rightarrow Mn^{2+}(s) + OH^{-}(s) + H(CpEt)(g)$$

As can be seen from the proposed reaction mechanisms, ALD reaction starts with active OH^- surface species and ends up with active OH^- surface species on top of the deposited metal permitting the deposition of another atomic layer. This would be the ideal case for the reactions. However, there are many opinions on the reaction mechanisms and some papers suggest that metal diketonates do not react with OH^- groups [50,132].

Experimental part

5 Research goals

The main objectives of this work were the atomic layer deposition of spinel structured $Ni_xMn_{3-x}O_4$ thin films, finding the proper parameters for the deposition, and investigation of the thin films' electronic and magnetic properties. Other nickel manganese oxide structures were looked into as well. Thin films of nickel manganese oxides have been previously made but currently there are no reports of nickel manganese oxides deposited with ALD which is why the atomic layer deposition of nickel and manganese oxides were used as a starting point for this work.

6 Sample preparation

This chapter presents all the steps and procedures taken to prepare the samples from the synthesis of the ALD precursors to heat-treating the deposited thin films. All the used equipment is introduced and the detailed parameters for each device are given. The characterization of the thin films and the results are in the following chapters of the experimental part.

6.1 Precursors' syntheses

Two precursors in addition to ozone were needed for the atomic layer deposition of nickel manganese oxides. Both precursors were made synthetization routes documented in this laboratory.

Bis(2,2,6,6-tetramethylheptane-3,5-dionato)nickel(II) ($Ni(thd)_2$) was synthesized from nickel(II) acetate tetrahydrate ($Ni(CH_3COO)_2 \cdot 4\ H_2O$, J.T.Baker, ≥ 99.7 %) and 2,2,6,6-

Tetramethyl-3,5-heptanedione (H(thd), Sigma-Aldrich, ≥ 98 %) using strong ammonia (NH_3, Merck) as a base. The net reaction is:

$$Ni(CH_3COO)_2 + 2\ H(thd) \rightarrow Ni(thd)_2$$

First, 5.92 g of nickel acetate was dissolved into 200 ml of 50 % EtOH. 10 ml of H(thd) was pipetted into mixture while heating in 60 - 80 °C and stirring on a hot plate. About 10 ml of ammonia was added so the pH is around 9-10 and a bluish precipitate starts to form. The solution was stirred and heated on a 90 °C hot plate for 3 - 4 hours after which it was vacuum filtered and washed with 30 ml of H_2O and 30 ml of 30 % EtOH. The formed turquoise sludge was kept in vacuum oven (Heraeus RVT 360) overnight in 20 torr & 50 °C and sublimated afterwards for about 24 hours in a Büchi Glass Oven B-585 sublimator. The temperature was slowly and stepwisely raised from room temperature to 120 °C while keeping the cooling water temperature of the coldfinger first at 60 °C and lowering it to 40 °C when the temperature was set to max. The obtained purple powder was kept in a freezer until use.

$Mn(thd)_3$ was more difficult to synthesize as it required potassium permanganate ($KMnO_4$, Merck, ≥ 99 %) in addition to manganese(II) chloride ($MnCl_2$, Merck, ≥ 98 %), H(thd) and strong ammonia. The two reactions happening during the synthesis are:

$$4\ Mn^{3+} + MnO^{-}{}_4 + 8\ H \rightarrow 5\ Mn^{3+} + 4\ H_2O$$

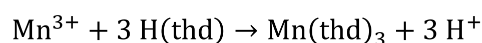

$$Mn^{3+} + 3\ H(thd) \rightarrow Mn(thd)_3 + 3\ H^+$$

2.014 g $MnCl_2$ was first dissolved into the solution of 20 ml MeOH and 100 ml H_2O. Also, 0.634 g of $KMnO_4$ was dissolved into 50 ml of MeOH (it was observed that the material did not completely dissolve). Then the two solutions were mixed together and about 1 ml of strong ammonia was added to ensure the pH is on the range of 6 - 8. A brown precipitate was formed. 12.4 ml of H(thd) was slowly pipetted alternately with NH_3 into

the solution to ensure that pH does not change greatly during the addition. The final solution was stirred for 24 hours, filtered and washed with 80 ml of MeOH. Last, the powder was vacuum-dried in the Heraeus vacuum oven for a couple of days (10 torr & 55 °C) and sublimated in a similar way with the Büchi sublimator as the nickel precursor was. The obtained dark brown powder was kept in a freezer until use.

Both precursors were similarly synthetized twice during the research. The obtained $Ni(thd)_2$ powders were alike but the second synthetization of $Mn(thd)_3$ produced a softer and not so clumpy powder which also had a more yellowish tint.

6.2 Thin film deposition

All the depositions were made with tubular hot-walled F-120 ALD-reactor made by ASM Microchemistry Ltd. Silicon wafer pieces (Si(100), p-type, Okmetic) and glass slides (Finnish specialglass) were used as substrates. In addition, one deposition was tried on stainless steel. All the substrates were cleaned similarly before the depositions; washed with 50 % ethanol solution and blown dry with pressurized air right before putting them into the reactor. This means that Si-wafers had a native silicon oxide (SiO_2) layer on the surface. Usually, three or two samples were deposited simultaneously (placed in a row to the reaction chamber) but setups with one to five samples were tested. If glass samples were coated together with Si-wafers, they were always placed in the middle of the chamber.

The $Ni(thd)_2$ and $Mn(thd)_3$ powders were used as precursors with O_3-gas (Fischer's O_3-generator). The powder precursors were sublimated from open vessels and swept to the reactor chamber with carrier gas. N_2-gas (AGA, > 99.95 %) was used as the carrier and purging gas with a primary flow of 300 sccm and secondary flow of 150 sccm. The primary gas flow transports the precursor gas to the substrate in the inner glass tubes and the secondary flow keeps the outer glass tube in correct pressure. In the few last depositions, a Parker domnick hunter HPN2-5000C-E nitrogen gas generator was used (99.999 % purity). The reactor was kept in pressures around 1 – 4 mbar.

There were a lot of deposition made with different parameters to find the ideal settings but after careful evaluation of the deposition parameters the following were used as a

standard. The $Ni(thd)_2$ and $Mn(thd)_3$ precursors were sublimated in temperatures of 130 °C and 110 °C respectively and the reactor chamber was heated to 220 °C. The pulse times for all precursors were 2.5 s with 8.0 s purges in between. Depositions were made with multiple different cycle amounts and with varying ratios of nickel and manganese.

In addition, quick test depositions were made with $Mn(acac)_3$ precursor. It was sublimated in 160 °C temperature and the reactor chamber needed to be heated to over 300 °C. Also, the precursor material needed longer pulse time of 5 – 7 seconds to fully saturate the surface.

6.3 Annealing

To further crystallize the thin films and to induce a possible change in structure, some of the thin film samples were annealed in an oven. Annealing is a heat-treatment technique that causes the atoms of a solid material to diffuse and change places in the crystal lattice and it also removes dislocations and stresses from the lattice which can change the properties of the material drastically. Different temperatures and annealing atmospheres can be used to control the resulting structure. Higher temperatures naturally lead to high temperature crystal structures and different atmospheres can have oxidizing or reducing effect on the final product. Also quenching, or quick cooling, after heat-treatment is a way to keep the high temperature crystal structure and prevent low temperature phase changes.

In our research, temperatures of 400 – 1400 °C were used with three different atmospheres: air, oxygen and nitrogen. Heating rate of 200 °C per hour was used and the maximum temperature was held for one hour before cooling on all treatments. The samples were quickly cooled in normal room air by taking them out of the oven as soon as possible after the annealing. ATV PEO-601 bench top furnace was used for oxygen and some air heat-treatments, Nabertherm RS 80/300/13 tube furnace was used in nitrogen annealing, and Koyo KTF 433 tube furnace was used in air.

Annealing was systematically done to all different kind of samples in different temperatures and atmospheres. Temperatures of 400 °C, 600 °C, 800 °C, and 1000 °C were done on air atmosphere while 400 °C, 600 °C, and 800 °C were done on oxygen and

nitrogen atmospheres. In addition, some additional tests were run on higher temperatures. Borosilicate glass samples could only be annealed in temperatures of 400 – 500 °C as one hour in 600 °C already melted and bended the glass partly tearing off the thin film.

The heat-treatment of a sample was made step-wisely. First, a sample was annealed in 400 °C and characterized, then 600 °C and characterization and so forth. From a single deposition of samples, one sample was annealed in every atmosphere if it was possible.

7 Characterizations

In this chapter, the different characterization methods used in the experimental work are briefly introduced and detailed parameters of each method are given. The results of the characterizations are discussed later on in chapter 7.

7.1 X-ray reflectivity

X-ray reflectivity (XRR) is an analytical technique to study the structure of surfaces, films, and multilayered materials. In XRR, an angled beam of X-rays at a grazing angle is directed to the sample and the intensity of the reflected rays is measured. The analysis is based on the fact that x-rays are reflected from the surface and the different interfaces of the material and the distances between them can be interpreted from the reflection patterns. Film's density can be determined from the critical angle below which total reflection occurs and the thickness can be interpreted from the interference fringe caused by the top and the bottom surfaces of the film.

Also, in multilayered materials, the periodical interference caused by each layer can be analyzed to specify the distances between the layers and the amount of layers. Furthermore, surface roughness can be determined from the noise it causes to interference patterns and from the fall of the intensity. [133,134]

The thickness of a thin film can be interpreted from a XRR-graph using PANalytical's X'Pert Reflectivity software, as shown in Figure 14. The position of the critical angle is often difficult to determine due to the geometrical contribution but a popular method is to place the angle on half-maximum of the intensity (first line from left). Then the first and second fringe angles are placed on the two first local minimums (second and third lines). After determining these angles, the thickness is calculated as:

$$\lambda = 2t[\sqrt{cos^2\Theta_c - cos^2\Theta_2} - \sqrt{cos^2\Theta_c - cos^2\Theta_1} \tag{3}$$

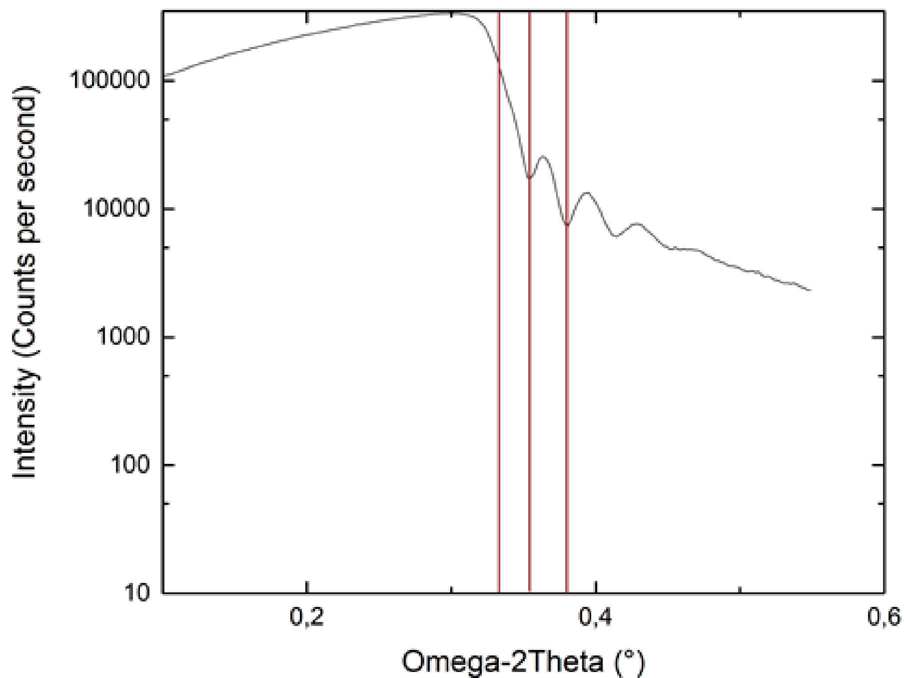

Figure 14. An XRR-graph of a thin film where the places of the critical angle and the first and second fringe angles are marked. Using them it is possible to determine the thickness of the sample.

In this work, x-ray reflectivity was used to determine the thickness of the deposited thin films. The thicknesses of the films are needed for defining of the ALD-window and for the optical bandgap calculations. Measurements were done with PANalytical X'Pert MPD Pro Alfa 1 x-ray diffractometer using a Cu K_{α} x-ray source with a wavelength of 1.5405980 Å. A step size of 0.002 ° and 1.0 s time per step were used. The measured angles omega were usually 0.1 – 0.5 ° after which the signal was too noisy. The XRR data was refined and analyzed with PANalytical's X'Pert Reflectivity software.

7.2 Grazing angle incidence x-ray diffraction

Grazing angle incidence x-ray diffraction (GIXRD) is a characterization technique suitable for examining the detailed structure of thin films. The difference between normal XRD

and GIXRD comes from the lower angles used in GIXRD to inhibit the effect of the substrate on the reflections and raise the volume of the measured film. Thin film thicknesses can be as low as few nanometers which means that normal XRD would mostly measure the diffraction from the substrate but with very shallow angles of GIXRD it's possible to inspect only the thin film on top. In a normal XRD machine the x-ray source and the detector are moved symmetrically in Bragg-Brentano geometry but in GIXRD the source is fixed on grazing angles and only the detector is moved.

The technique is based on Bragg's law which states that diffractions occur when radiation with wavelength similar to atomic spacing is scattered from the atoms of the material. When the scattered waves interfere constructively, distinctive peaks can be seen on the x-ray diffractogram and they can be identified to present certain Miller indices in the crystal lattice. The Bragg's law follows the equation:

$$2d \sin\theta = n\lambda \tag{4}$$

where d is distance between scattering atoms, θ is scattering angle, n is a positive integer and λ is wavelength. For example, GIXRD is suitable for phase identification and crystal structure analysis. [134,135]

GIXRD measurements were done with PANalytical X'Pert MPD Pro Alfa 1 x-ray diffractometer using a Cu K_α x-ray source with 1.5405980 Å wavelength. Scans were first conducted in the angles of 5 – 60 ° but later on with 5 – 80 ° to see all necessary peaks. Normally, a step time of 3 seconds was used with a step size of 0.05 ° but longer and more accurate scans were made with longer step times and smaller step sizes.

7.3 Spectroscopy

Optical spectroscopy is a mean to study properties of a material through the interaction between electromagnetic radiation and the material. All visible matter either absorbs or reflects electromagnetic radiation. The electromagnetic radiation (photons) cause measurable resonance on the sample which can be measured for example as spectral

lines. The frequency of the electromagnetic radiation is related to the energy of the photon which can be calculated from the formula:

$$E = hf \tag{5}$$

in which h is the Planck constant and f is the frequency of the radiation

Studies were conducted using visible light and radiation ranging from the near-ultraviolet – to the near-infrared ranges (190 – 1100 nm). The measurements of the first precursor patch were done using a Hitachi U-2000 UV/vis spectrophotometer which broke down, so the rest of the measurements were done with newer PerkinElmer Lambda 950 UV/vis/NIR spectrophotometer. Transmittance (the intensity of the light passed through a sample) and reflectance (the intensity of the light reflected by a sample) were measured to calculate the absorption of a sample with the equation:

$$A = \frac{100 - \text{transmittance} - \text{reflectance}}{100} \tag{6}$$

The absorption of the glass on which the film was deposited is subtracted from the absorption of the sample to give only the absorption of the thin film. Then the absorption coefficient α can be derived from absorption A and thickness of the film t:

$$\alpha = \frac{\ln(A)}{t} \tag{7}$$

The optical energy band gap E_g can be determined by plotting $(\alpha hv)^{1/r}$ versus hv and extrapolating a straight line to cut the x-axes. Different r-values are used for different band gaps: for example, 0.5 for allowed direct, 2 for allowed indirect, 3 for forbidden

direct and 1.5 for forbidden indirect optical transition. The calculations were done with the assumption that the transitions are allowed direct transitions. [136,137]

The Hitachi U-2000 spectrophotometer was operated on remote control mode using Teknologia tutkimuskeskus VTT Oy's Thinscan program that has been designed for the spectrophotometer's thin film analysis. First, the scanning parameters were given (wavelength step 1 % and width of the scan step 1 nm) and spectrophotometer's baseline was measured in wavelengths of 190 - 1100 nm. Then the transmittance and reflectance measurements were done on the same wavelengths (sample holder was changed between the transmittance and reflectance measurements) and the data was collected as a XY text file. On the PerkinElmer Lambda 950 spectrometer, wavelengths of 250 – 1100 nm were scanned using 1 nm steps. The response time of the detector was set to 0.4 s. The detector part of the device needed to be changed between the transmittance and reflectance measurements.

7.4 Magnetic measurements

Manganese oxides and nickel manganese oxides, specially the spinel $NiMn_2O_4$, have shown interesting magnetic phenomena such as colossal magnetoresistance and ferromagnetism [138]. The magnetic properties of the nickel manganese oxides depend on their oxygen stoichiometry and differences in the stoichiometries of different ions. Therefore, the magnetic properties of our samples were investigated with field-cooled (FC), zero-field-cooled (ZFC) and magnetic hysteresis measurements and compared to the literature on the area. The FC and ZFC measurements give an estimate of the temperature where the transition from ferromagnetic to paramagnetic behavior happens. The magnetic hysteresis loops reveal how the material behaves in changing magnetic field at a certain temperature.

The ZFC measurements were conducted by cooling the sample to 5 K, applying a magnetic field of 5000, 1000 or 50 Oe, and heating the sample to 220 K. The FC measurement was otherwise similar but the magnetic fields were applied already during the cooling to 5 K and maintained while heating to 300 K. The magnetic hysteresis loops were measured using a magnetic field varying from -30 kOe to 30 kOe while keeping the sample in 10 K.

All the measurements were done using the Physical Property Measurement System DynaCool from Quantum Design.

7.5 Scanning electron microscopy

Scanning electron microscopy (SEM) is a way to image nanoscale details from a surface of a sample. SEM is based on a focused electron beam that scans through the sample. The beamed electrons interact with the sample and produce various signals such as x-rays and back-scattered electrons which are read by the detectors. These signals can be processed to form, for example, high-resolution images of the sample or they can be used to determine the abundance of different elements in the sample. Typically, the sample needs to have a conductive surface to be used in SEM or the accumulated charge on the sample can cause damage. However, the sample can be sputter-coated with conducting material or a low-voltage SEM can be used. [139]

SEM was used to determine the quality of thin film depositions. It reveals the surface of the sample in detail and shows features such as surface roughness. The microscope used was a Zeiss Sigma VP that was operated in high vacuum ($< 10^{-5}$ Pa) with 1.5 kV current detecting the signal of secondary electrons. Small pieces of deposited Si-samples were used for the scans.

8 Results

Results of all the experimental work done are presented and discussed in this chapter. The results are also compared to the relevant literature.

8.1 Quality of the thin films

The quality of the deposited thin films differentiated largely which also made it challenging to find the proper deposition parameters. Each sample usually had darker color on edges compared to the middle and there were also samples that had substantial unsymmetrical color variances. Also, there was variation between the samples used in a single deposition: the first sample in the row could have completely different color than the last sample of the row. This might mean that the samples have different compositions but more likely it is because of divergence in thicknesses of the thin films. The variation is most likely caused by the travelling wave configuration of the reactor meaning that the gasses enter the reaction chamber from one side and exit on another side causing a gradual difference into the composition of the gas. It is also possible that the gas flows differently in front and back side of the reaction chamber causing uneven results. Nilsen *et al*. reported similar behavior while depositing manganese oxide with the thd-precursor [125]. According to them, the ozone gas caused the gradient growth because O_3 decomposes quickly in high temperatures (0.03 s at 250 °C) but in addition, the manganese oxide film is a known catalyst for ozone decomposition.

On the other hand, the results of subsequent depositions are very similar even though the mentioned problems persist in each deposition. This was easily proven by measuring the amounts of sublimated precursors after each deposition. Usually the variation was around 0.01 g between depositions with same pulse lengths and cycle amounts which at least means that the sublimation of the precursors were even between depositions. Also, similarly positioned samples in equal consecutive depositions had very identical thicknesses.

There was variance between different precursors. The first batch of manganese thd-precursor produced more diverse colors than the second thd-batch. Some of the films

from the first batch had very yellowish to even slightly red colors but the second batch produced only brownish colors similar to the $Mn(acac)_3$ precursor. This behavior is most likely due to higher nickel content in the films with the first precursor batch, which can be clearly seen from the XRD-results in the following chapters. There was a clear difference between the first and second $Mn(thd)_3$ precursors as noted before. Although the second batch produced better quality films, it left a mixture of yellow and black clumpy powder instead of hard black grains that the first batch left. This hints that there is possibly some other material too in the latter thd-precursor batch. Thus, the leftovers of a sublimated second thd-precursor were analyzed with powder XRD to identify the remainings, shown in Figure 15.

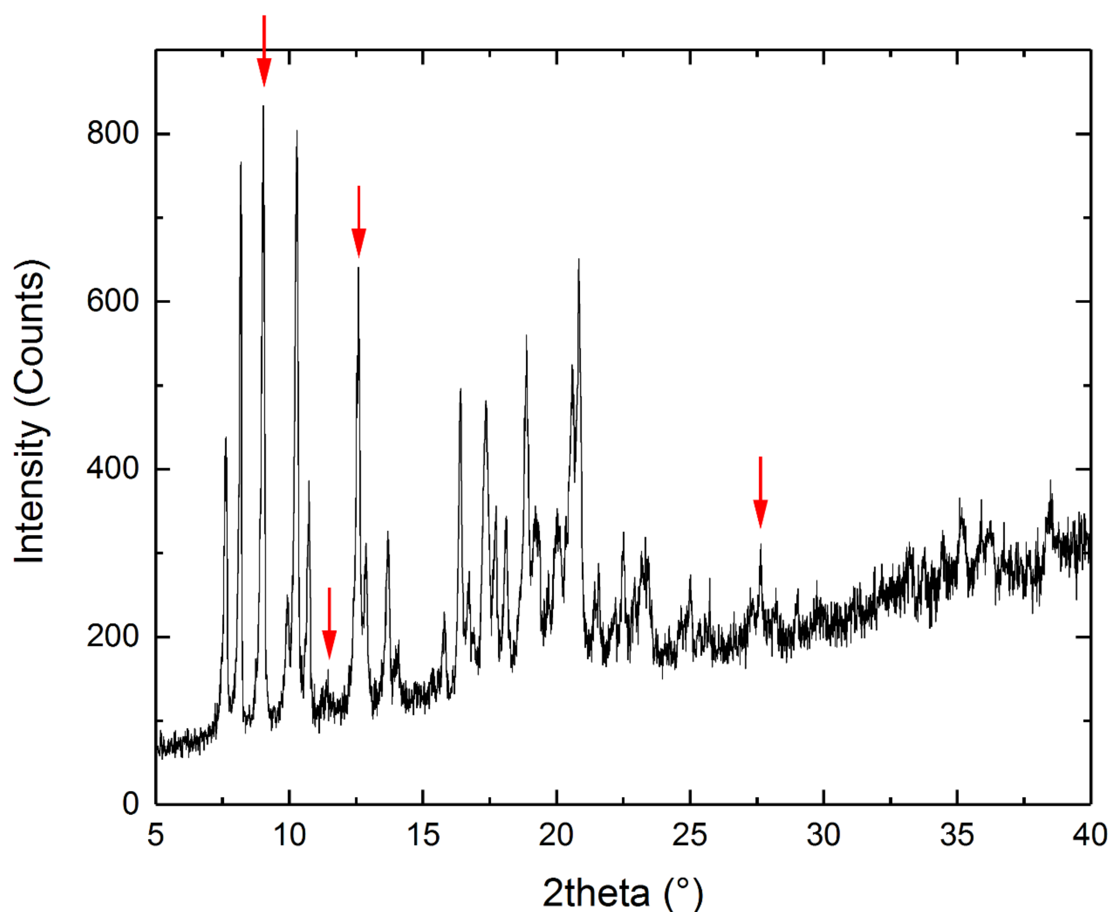

Figure 15. Powder XRD of a used precursor from the second patch of Mn-precursor material. The red arrows mark peaks matching to manganese acetate tetrahydrate.

The Figure 15 reveals that the precursor leftovers most likely contain some manganese acetate tetrahydrate as well as some amorphous and crystalline organic material. Manganese acetate tetrahydrate got around 80 % match with PANalytical's Match program and other substantial matches were purely organic materials. This result is supported by the fact that the second precursor batch worked better than the first one even though it contained impurities. Manganese acetate tetrahydrate and the organic materials have high sublimation temperatures of well over 200 °C so they will not sublimate during the ALD process and cause impure films. Yet, the impurities are somehow affecting the deposition of the manganese. One possible explanation is that a small amount water sublimates from the hydrate and helps with the reactions happening on the surface. For example, it could be that the additional H_2O-gas inhibits the breakdown of O_3-gas and helps it oxidize the surface.

It is not certain why the two thd-precursors batches differ from one another as they were made with the same recipe but the second batch clearly contained some impurities or some of the $Mn(thd)_3$ reacted further to different forms. As the second precursor batch presumably contained hydrates, the difference of the precursors may come from the vacuum oven which was used for removing the moisture from the powder. Perhaps there was a problem with the vacuum oven or the sample was exposed to the atmosphere of the room for too long before going to the sublimator.

It is possible to simulate XRR-graphs with the PANalytical's X'Pert Reflectivity software meaning that the software tries to simulate and fit a graph similar as possible to the one you already have. It does it by testing different numeric values for density, thickness and roughness until it finds the closest match. One way to test the quality of the films is by checking if the simulations can find a near match to the samples. The simulations match some XRR-graphs very neatly, example shown in Figure 16. Furthermore, scanning electron microscope showed very even and uniform surface, as seen in Figure 17.

Altogether, the samples were of ok quality and the repeatability of the depositions was good but the fact that the samples of a single deposition diverged needed to be taken account.

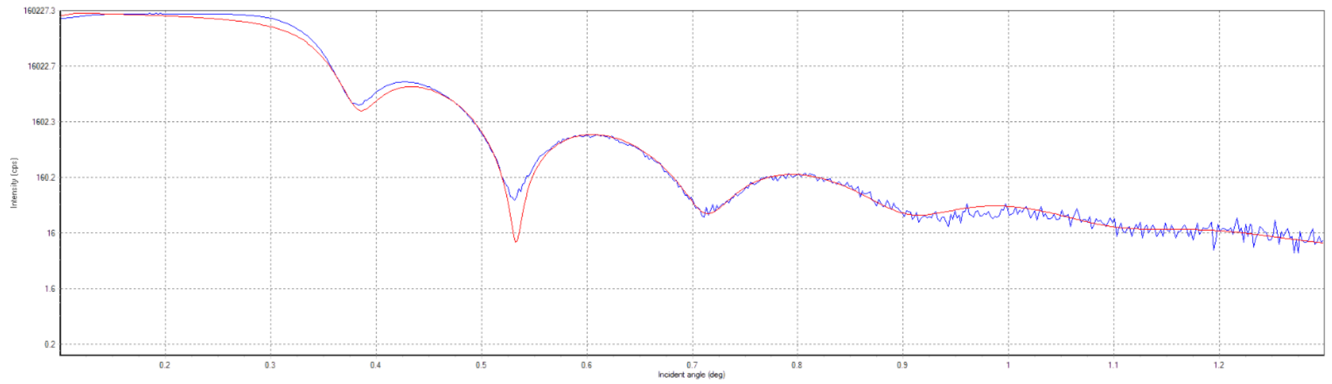

Figure 16. XRR-graph of a deposited manganese thin film (blue) and the simulated fit (red).

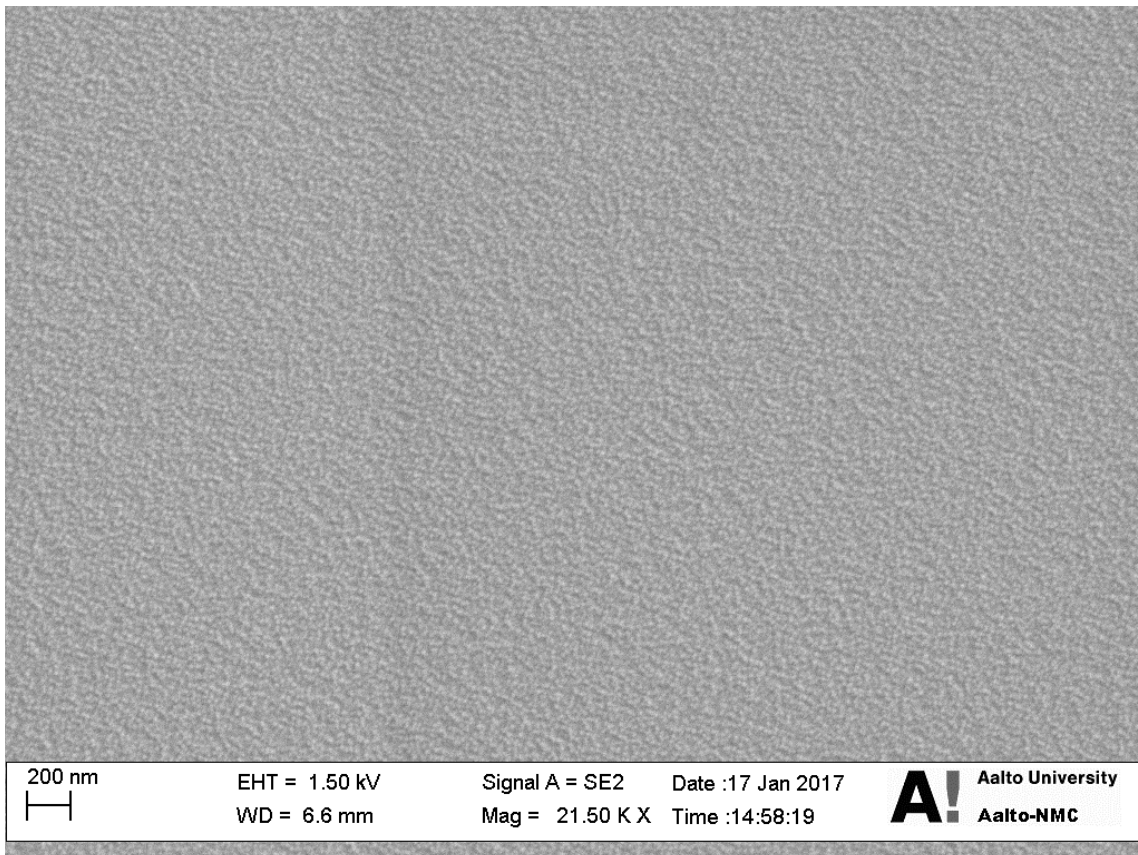

Figure 17. SEM-picture of a nickel manganese oxide deposition onto a Si-wafer. Very uniform and smooth looking surface.

8.2 ALD-reactor optimization

The first depositions of our research were done with $Mn(thd)_3$ and ozone to find out the optimal deposition parameters for the reactor and manganese precursor. The nickel precursor was already tested and the parameters were optimized beforehand for the reactor. As mentioned in chapter 2, the ALD-window can be found by changing the pulse and purge lengths and plotting them against growth per cycle that was determined with the thicknesses gained from the XRR measurements. Literature gave us a good starting point to look for the parameters. The results from optimization of reactor settings are found in Figure 18. The results are obtained from glass samples because their results were more uniform.

The A graph of the Figure 18 shows how the growth rate stabilizes around three seconds' pulse time. There was clearly not enough manganese to saturate the surface in the shortest pulse lengths because growth rate increases near linearly with pulse length before the two or three second mark. The growth rate seems to go down after 2.5 s data point but there was a lot of variation in the growth rates even with same pulse lengths. Depositions with similar parameters had maximum variation of 0.03 Å/cycle growth rate.

The reaction chamber of the F-120 ALD-reactor is heated from outside (hot wall) and it has a separate heater on the both ends of the tubular chamber. This means that the chamber temperature in the Figure is the average of the temperatures on both sides and that the actual temperature inside the reaction chamber is actually about 20 °C less. B graph in the Figure 18 displays that there is a near linear region between the chamber temperatures of 190 – 240 °C. Growth rate rose quickly after 240 °C and it also caused very uneven depositions. The XRR charts of Si-samples were already so rough that the thickness could not be determined, as can be seen in Figure 19. Around 280 °C the quality of the depositions plummeted and thicknesses could not be measured for the glass either. Similar findings have been reported by Nilsen *et al.* who noted that this was probably due to decomposition of $Mn(thd)_3$ [125].

GIXRD was measured from the manganese oxide silicon thin films (shown in Figure 20) and revealed very low intensity peaks that match well with $Mn(thd)_3$ deposited β-MnO_2 patterns from the literature [125,131]. In the literature higher deposition temperatures showed low intensities similar to our sample. The peak at 20.5 ° matches β-MnO_2 (100)

reflection, the peak at 28.3 ° matches (110) reflection, and the peak at 41 ° matches (200) reflection similarly to the first literature source. The hump at 73 ° is marked as (310) reflection in the latter source. Glass deposition shows more clearly the (211) and (220) reflections in 57 ° and 59 ° similar to the latter literature source. The glass substrate shows as the big mountain in 15 – 25 ° and Si-wafer can be seen in the peaks at 50 – 55 °. It is clear that the deposited manganese oxide was β-MnO_2. [125]

In addition, $Mn(acac)_3$ was quickly optimized for the reactor. It required higher sublimation temperature of 160 °C but also higher chamber temperature of over 300 °C to produce uniform looking thin films. The pulse time needed to be set to over 5 seconds to get good growth per cycle.

Overall, the results are in line with the literature. Average growth rates of 0.2 Å/cycle have been reported for the $Mn(thd)_3$ and both pulse time and chamber temperature are found to be on the same scales [125]. Based on these results we decided to use 2.5 seconds pulse time for $Mn(thd)_3$ and 220 °C chamber temperature as the standard parameters.

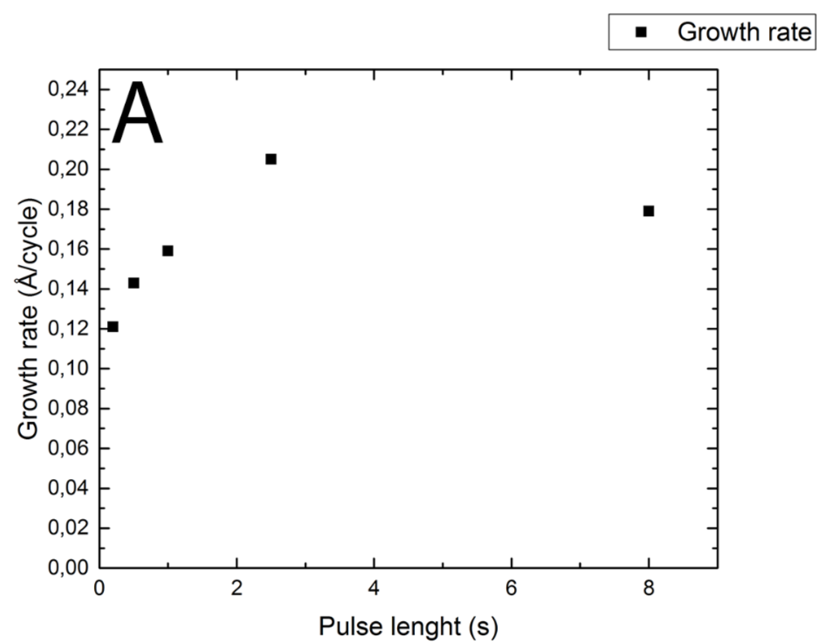

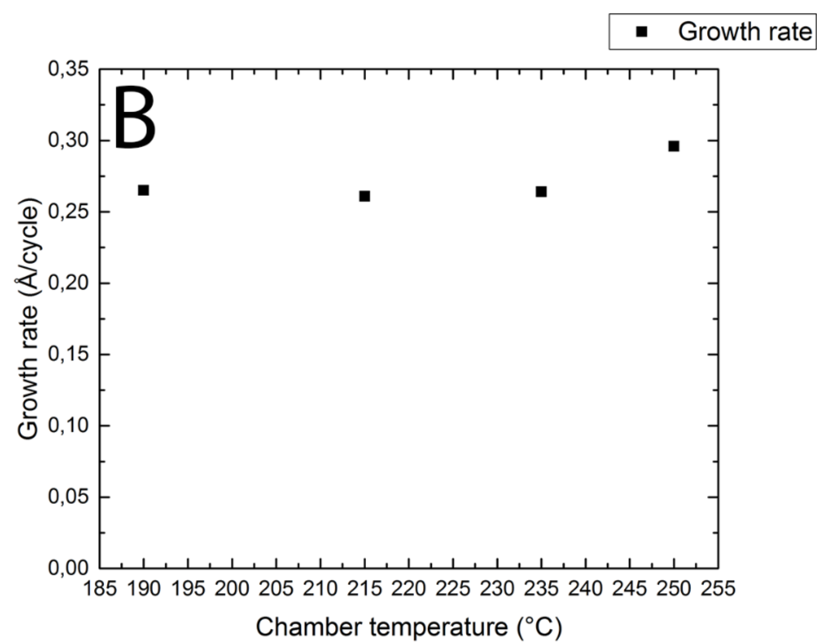

Figure 18. A: growth per cycle plotted against the pulse length of $Mn(thd)_3$. B: growth per cycle versus chamber temperature.

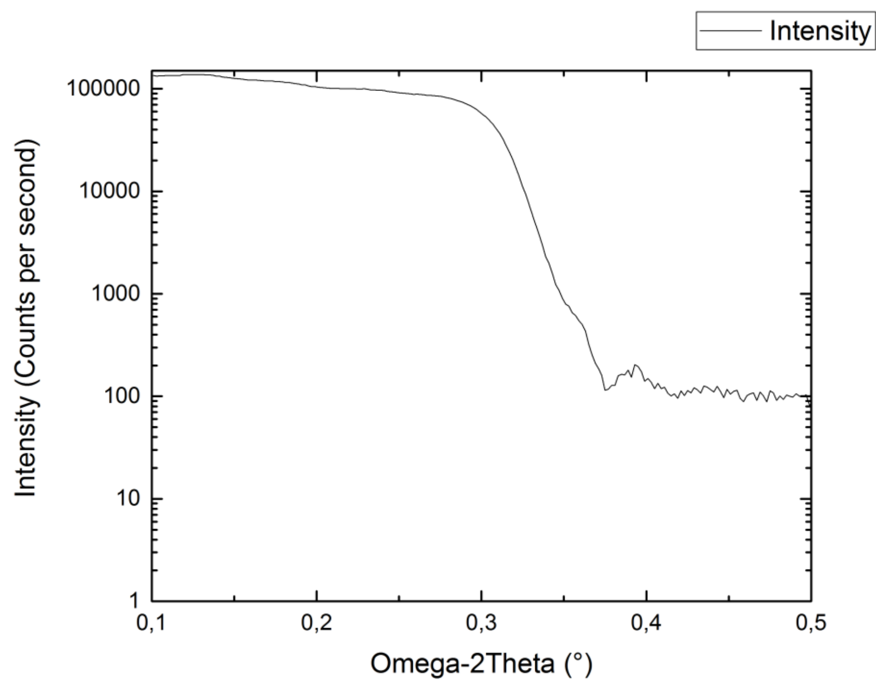

Figure 19. XRR of a manganese sample deposited with 250 °C chamber temperature. The thickness cannot be measured as the fringe angles cannot be determined.

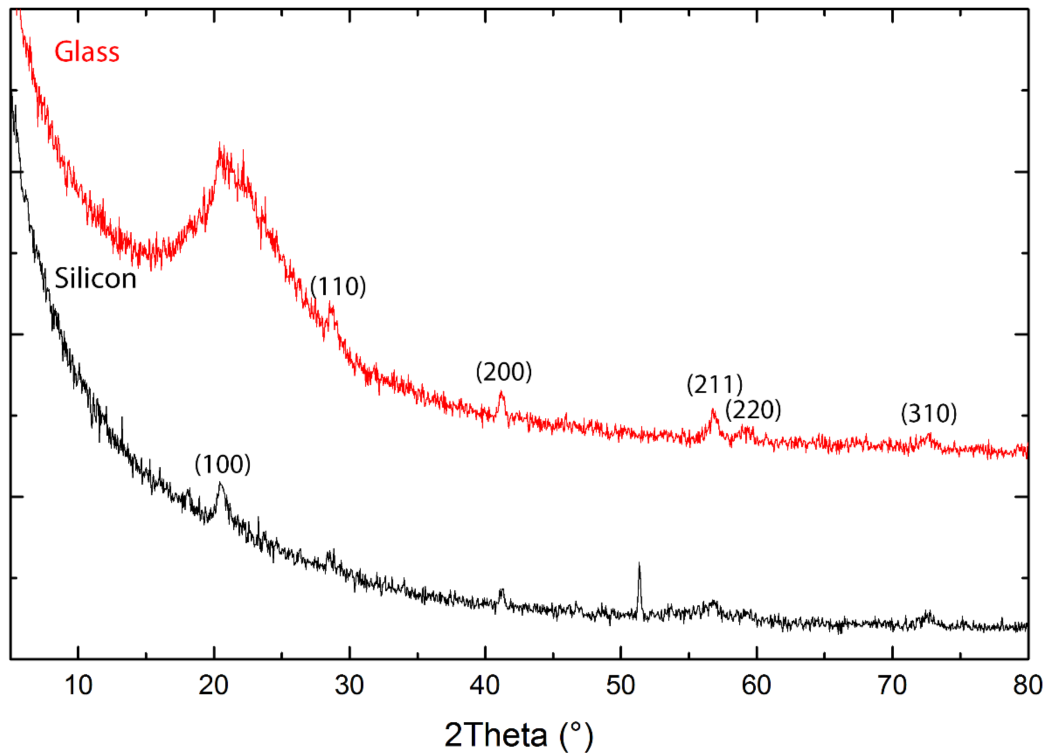

Figure 20. GIXRD patterns of manganese depositions to glass and Si-wafer.

8.3 Crystal structure of the thin films

One of the experimental goals of this research was to deposit the spinel structure of nickel manganese oxide. Thus, the crystal structure of the deposited thin films is important to determine with the GIXRD measurements. Every deposited thin film was measured with XRD.

In the beginning of the research XRD-measurements were conducted with multiple different settings to find fitting XRD-scan for our samples. GIXRD measurements of eight differently grown nickel manganese oxides on Si-wafers are presented in the Figure 21 and measurements of seven glass samples are given in Figure 22. All the depositions were made with the standard ALD-parameters mentioned in the chapter 6. The samples are named based on their nickel-manganese ratio: For example, a deposition having full cycle of one manganese layer and three nickel layers is called "Ni3:1Mn". Depositions were done with varying total cycle amount because different ratios of nickel and manganese altered the growth per cycle and the thickness of the samples was tried to keep the same. The pursued thickness was 100 nm.

Some depositions were done with different reactor settings to see if there is any difference. For example, variation in pulse and purge times and higher sublimation temperatures were tested but no observable changes were seen in the GIXRD measurements.

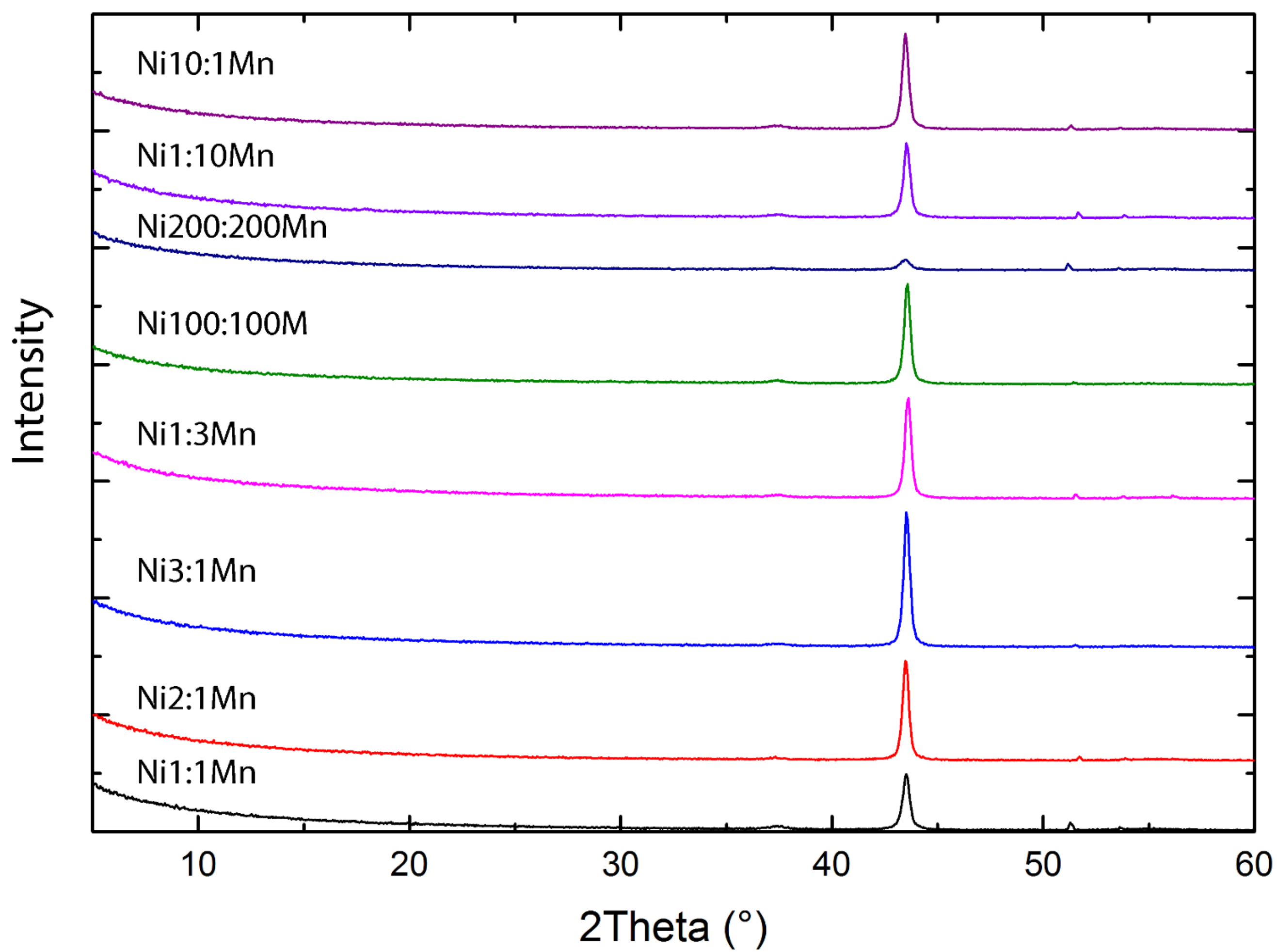

Figure 21. GIXRD measurements of a series of samples grown on Si-wafers.

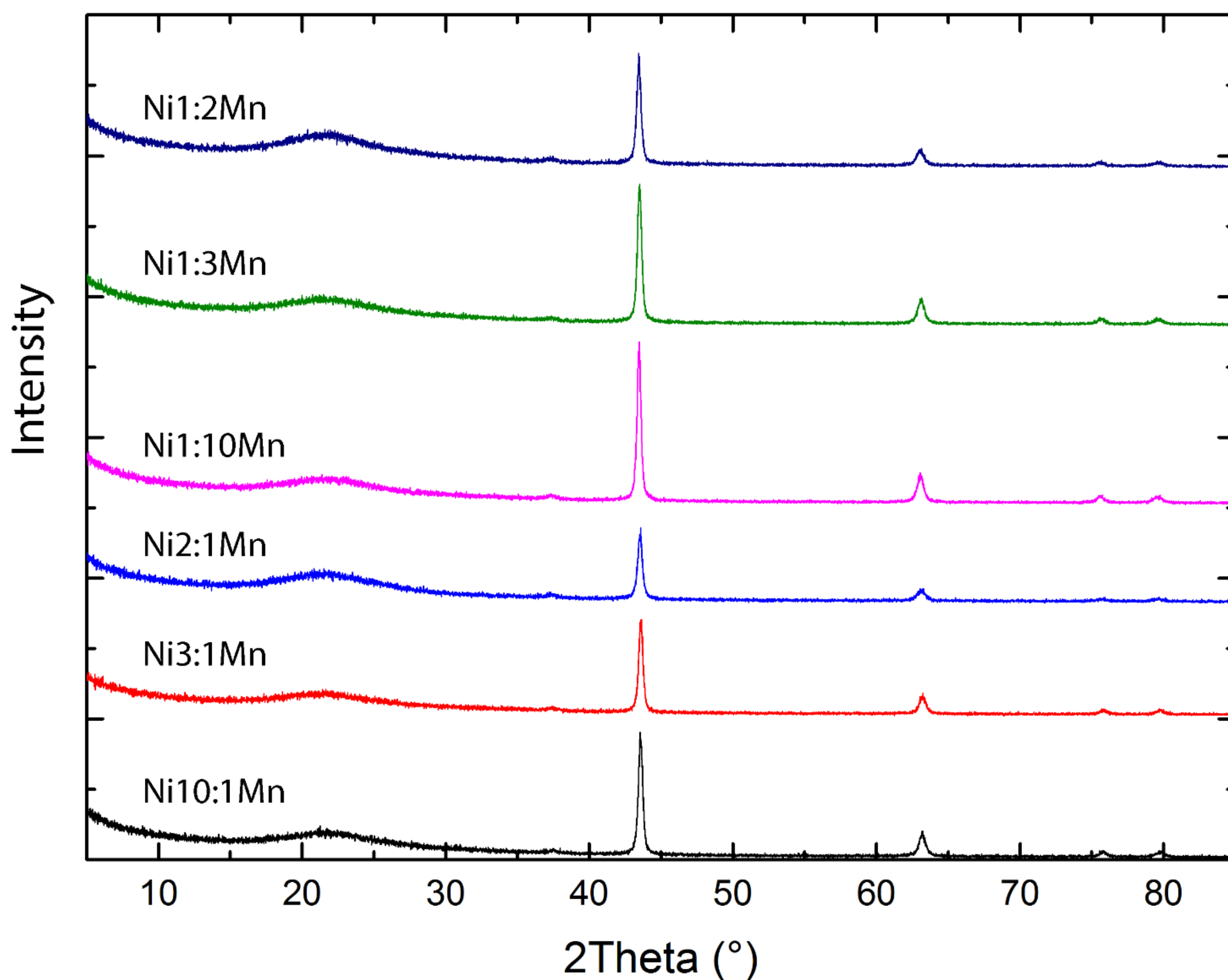

Figure 22. GIXRD measurements of a series of samples grown on glass slides.

The Figures 21 and 22 show the surprising similarity of the samples. Only change between the patterns of the samples is in the intensity of the peaks. It was expected that the crystal structure of the samples would change according to the ratio of nickel and manganese as in the phase diagram in Figure 9. Obviously atomic layer deposition causes different structures than the solid-state methods reported in the literature section.

In the Figure 21, there is a clear peak on the 43.5 ° but also a small hump on 37.3 °. The small peaks between 50 – 55 ° are from the Si-wafer. In addition, Figure 22 shows the glass substrate between 15 – 25 ° and additional NiO peaks at 63 °, 76 ° and 80 °.

The interpretation of the patterns is very difficult because nickel oxide and all the different forms of nickel manganese oxide have peaks on same angles. Nickel oxide has (111) peak at 37 °, (200) peak at 43 °, (220) peak at 63 °, (311) peak at 76 °, and (222) peak at 80 °, as seen in Figure 23. The spinel $NiMn_2O_4$ has very similar peaks at 37 ° (222), 43 ° (400), 63 ° (440), 76 ° (622), and 80 ° (444), shown in Figure 24. Furthermore, Ni_6MnO_8 has the very same peaks at the same angles: (220), (400), (440), (622), and (444) respectively only difference being in the mutual intensities of the peaks, as can be seen in Figure 25. Even $NiMnO_3$ has peaks on some of the angles: (110) at 36 °, (120) at 43 °, and (130) at 63 ° but it does not have peaks at 70 – 80 °, shown in Figure 26.

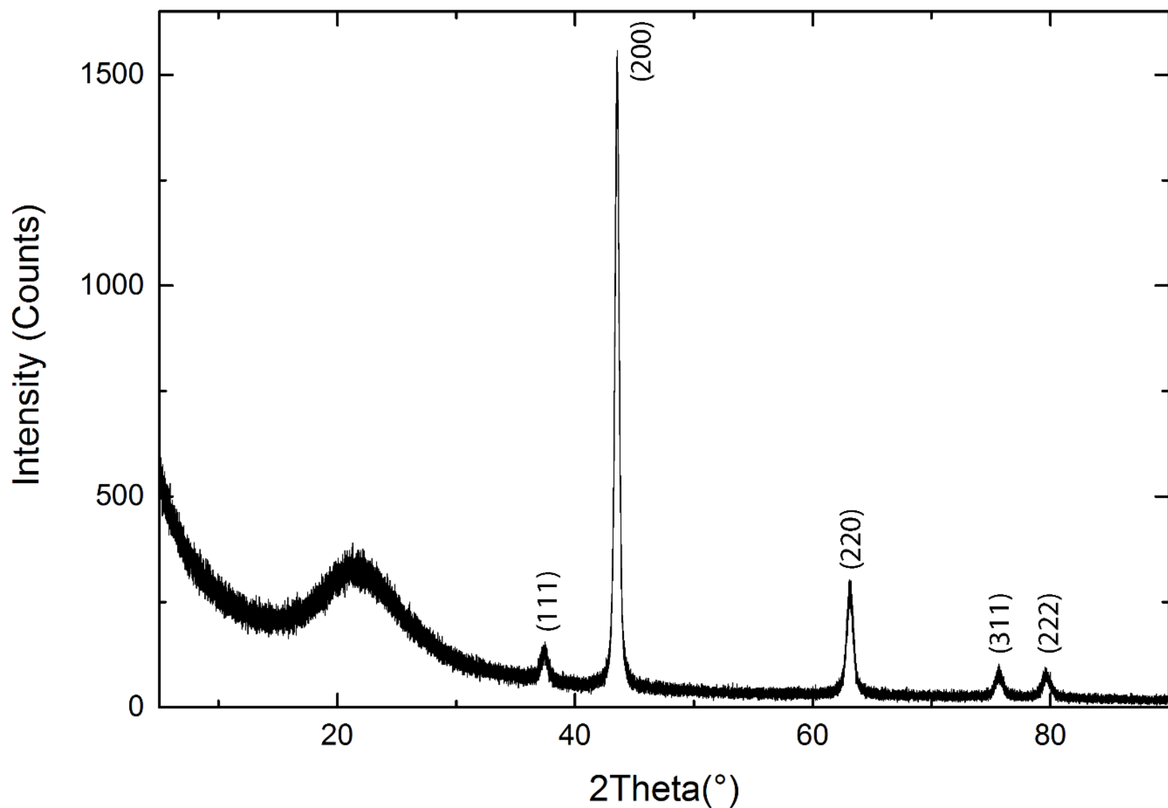

Figure 23. GIXRD pattern of NiO deposited on glass with the same F-120 ALD-reactor.

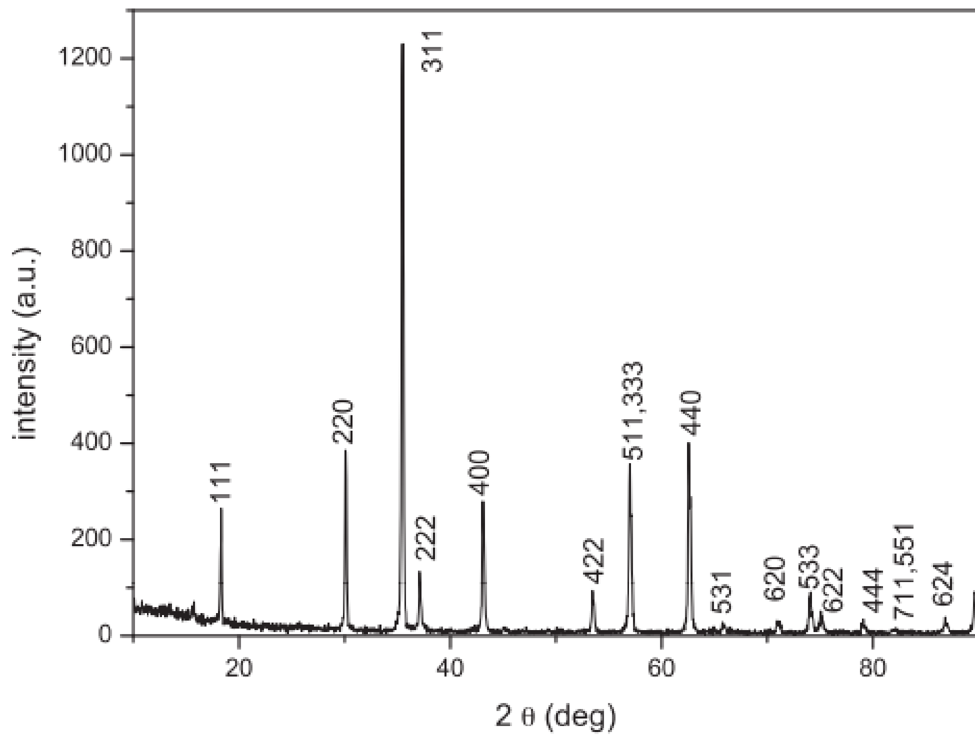

Figure 24. XRD pattern of $NiMn_2O_4$ powder from measurements of Sagua *et al*. [65]

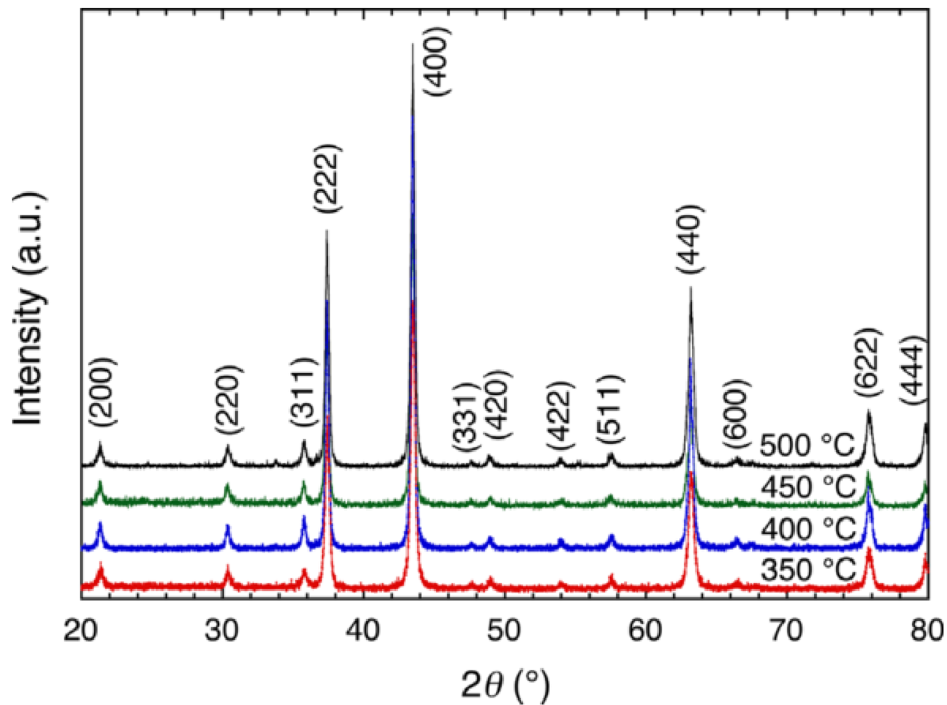

Figure 25. XRD of Ni_6MnO_8 calcined in different temperatures by Taguchi *et al.* [81].

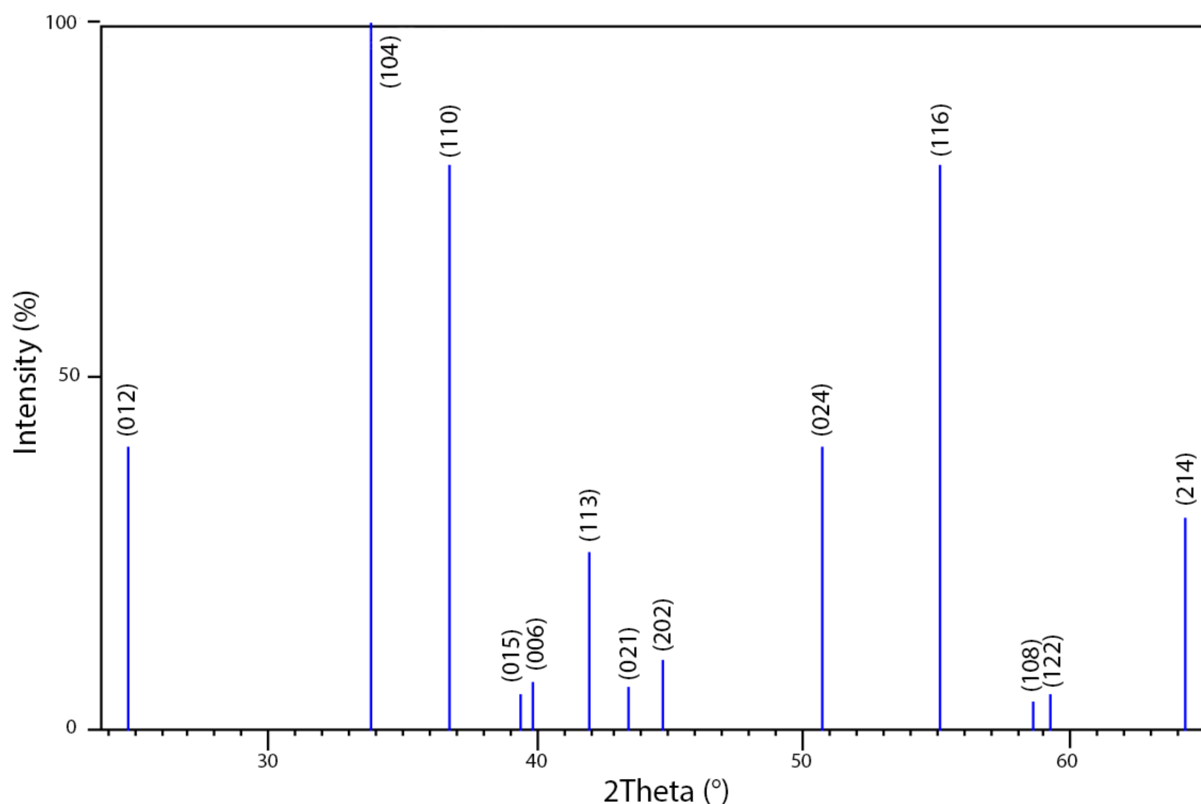

Figure 26. The XRD lines of $NiMnO_3$ (ICDD file 00-002-0880)

From the different XRD Figures above it can be interpreted that the XRD pattern of NiO is the closest resemblance to the patterns seen on the samples. Even the intensities of the samples' peaks match well with NiO. Based on this, the samples definitely contain crystalline nickel oxide. Still, it is hard to say if the samples contain only crystalline NiO or crystalline NiO and small amount of some crystalline nickel manganese oxide because of the similarity of the reflection angles. It is also possible that the manganese oxide is in amorphous form and does not show in the XRD.

Even if the GIXRD shows only NiO, it is certain that we also deposited manganese because the $Mn(thd)_3$ precursor lessened during the deposition. The growth per cycle of manganese oxide is on average less than one layer of the material meaning that every manganese oxide cycle does not produce a complete layer but possibly diffuses into the material. Also, the intensities of XRD intensities of deposited manganese films have been very weak (as seen in Figure 20) so the manganese could just be hidden behind the strong NiO pattern. However, Layek *et al*. had very similar XRD-results with Mn-doped (< 10 %) NiO nanoparticles so it is possible that there is just too little manganese on the films [140].

Surprisingly, already the first depositions done with the second in-lab synthetized Mn-precursor showed large digression from the earlier results. Results of few depositions with different Ni-Mn ratios are presented in Figure 27. Already 1:3 Ni-Mn ratio produced a clear pattern of spinel $NiMn_2O_4$ and the pattern got stronger with increased manganese. Likewise, the pattern of NiO got weaker as the relative amount of nickel lessened. The NiO pattern is still dominating in the 1:1 sample as there are no peaks at 18 °, 30 ° or 57 ° angles. Also, the peaks have which match both NiO and $NiMn_2O_4$ have high intensities at 38 °, 44 ° and 64 ° angles. Based on these results with the second precursor batch, it can be said that the ALD of $NiMn_2O_4$ is successful. However, we cannot say if the samples are mixtures of NiO and $NiMn_2O_4$ based on the XRD results alone.

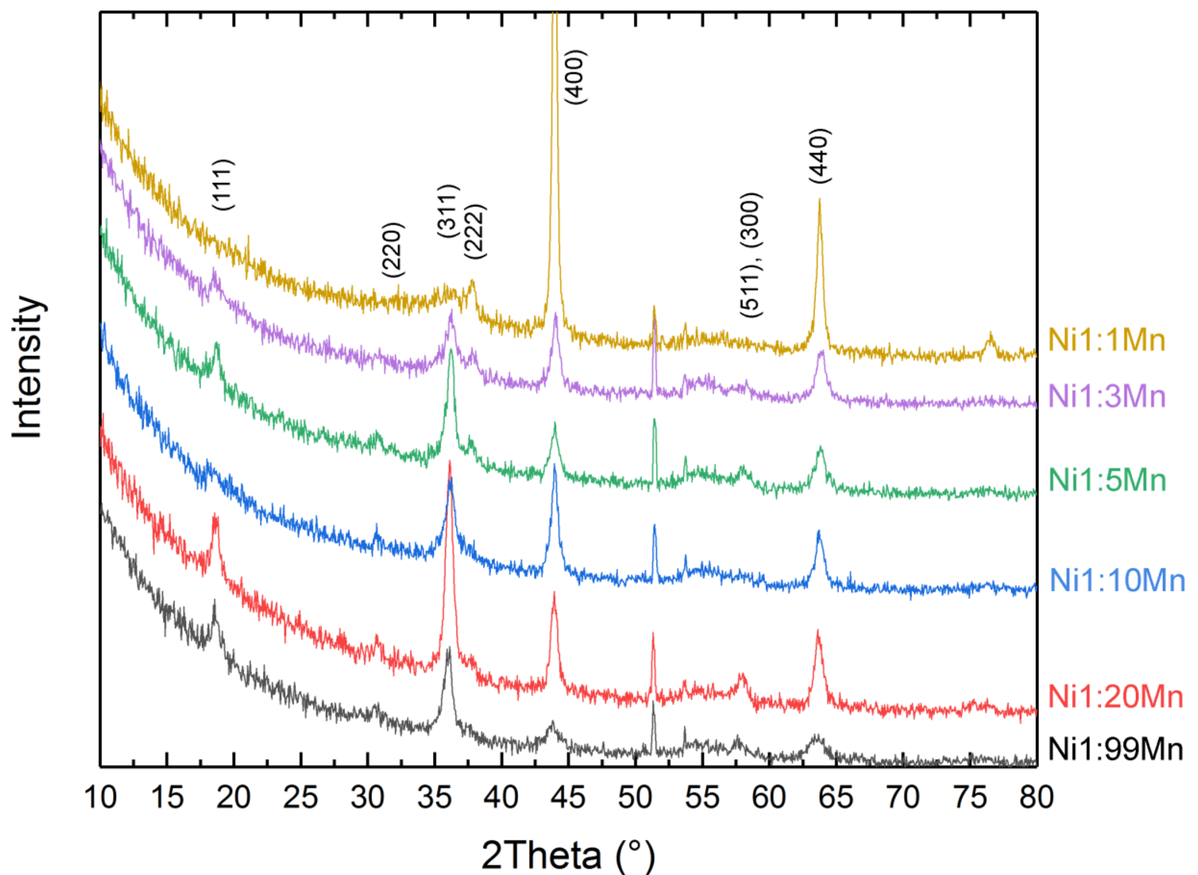

Figure 27. GIXRD patterns of samples deposited with second Mn-precursor batch. Peaks belonging to $NiMn_2O_4$ marked on top with Miller indices.

Comparison of 1:20 Ni-Mn ratio depositions with the same reactor settings but using a different batch of Mn-precursor material is presented in Figure 28. The first XRD pattern resamples crystalline NiO similarly to the samples in Figure 23 but the second pattern has new peaks. Furthermore, the peaks found on similar angles have very different intensities.

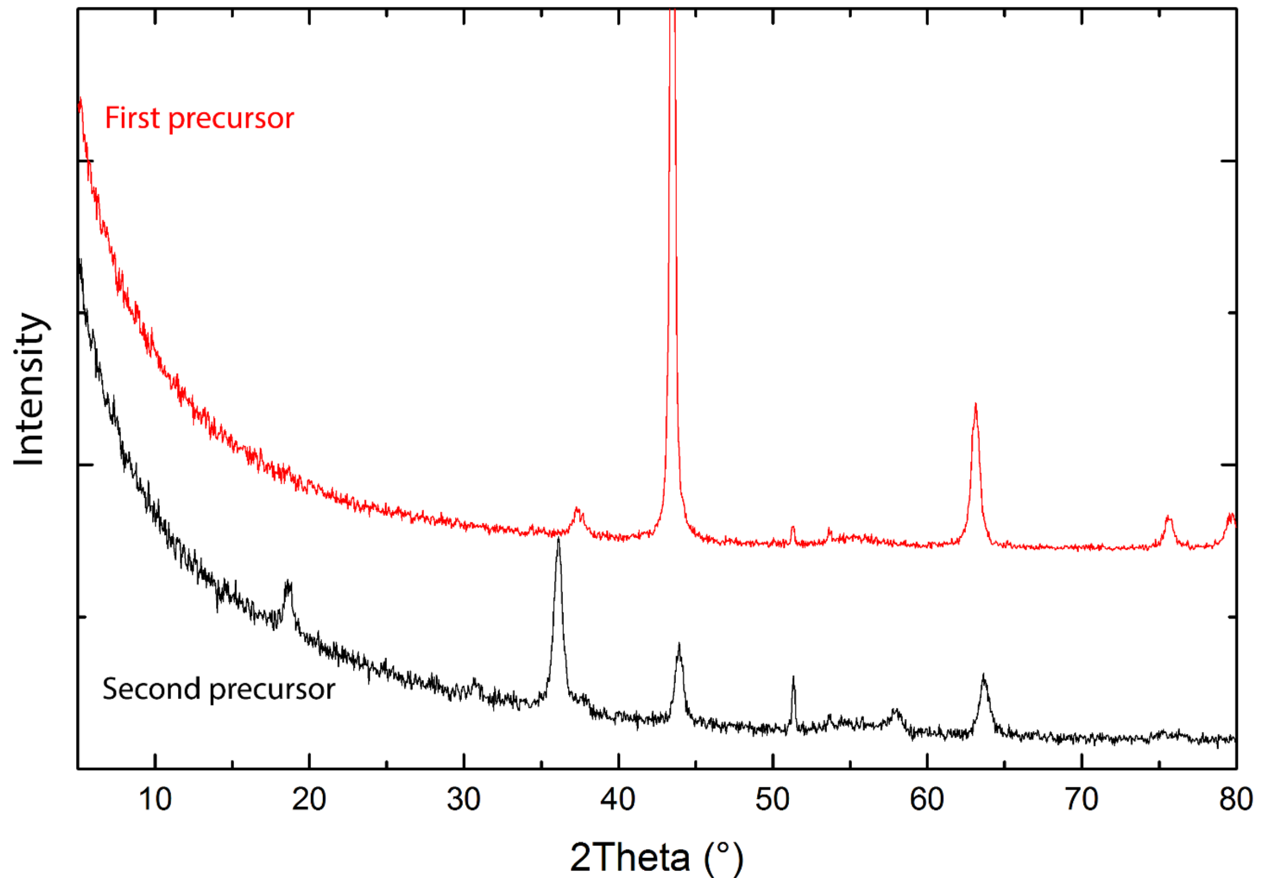

Figure 28. GIXRD patterns of 1:20 Ni-Mn samples deposited in similar conditions using precursor materials from two different batches. The first precursor sample shows the pattern on NiO and the second precursor sample shows the pattern of $NiMn_2O_4$.

Both samples in Figure 28 show peaks at 37 °, 43 ° and 63 ° but the sample with the second precursor material shows additional peaks at 18 °, 30 °, 36 °, and 57 °. The angle of the peaks in addition to their intensities match closely with the spinel $NiMn_2O_4$. The intensities

would be a near perfect match to the powder XRD reference in Figure 24 if the peaks in 18 ° and 57 ° were more intense.

The few depositions made with $Mn(acac)_3$ precursor produced $NiMn_2O_4$ containing films already with 1:1 Ni-Mn cycle ratio, shown in Figure 29. The pattern of $NiMn_2O_4$ is clearer with the $Mn(acac)_3$ precursor as can be seen from the two peaks at 36 ° and 38 ° angles which have usually been mixed to one broader peak with the other precursors. In addition, the peak at 30 ° is very intense compered to $Mn(thd)_3$ precursor. However, $NiMn_2O_4$ was not fabricated on every 1:1 ratio deposition as the parameters of reactor were changed between the depositions.

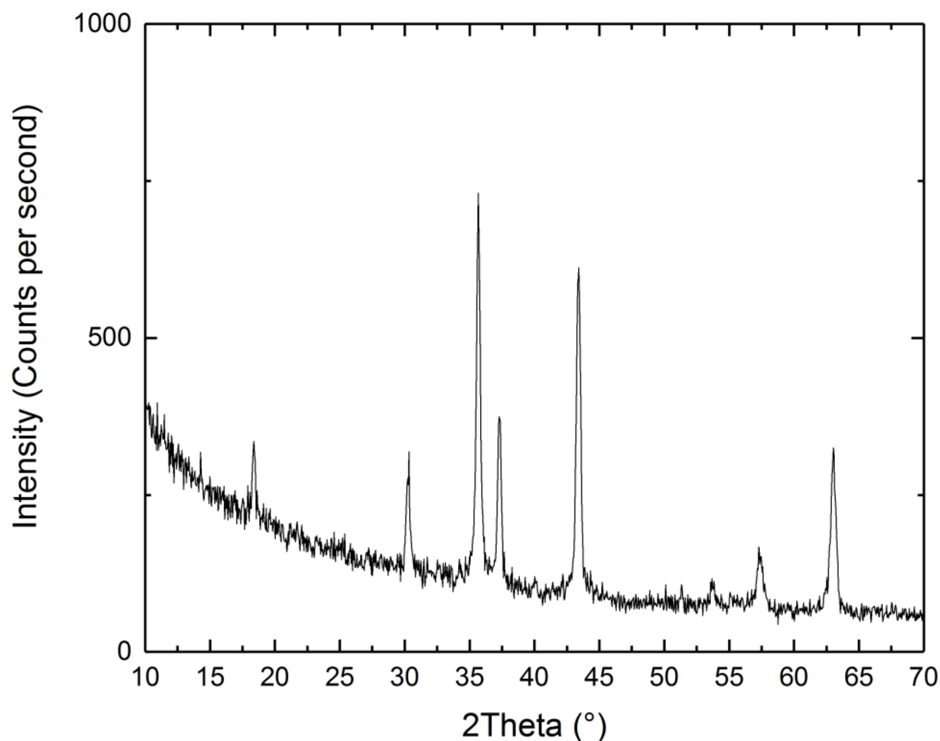

Figure 29. GIXRD pattern of a 1:1 Ni-Mn sample deposited from $Mn(acac)_3$ precursor. Deposited in 320 °C temperature with 7 second Mn-pulse time. Parameters for nickel were kept the same as before.

8.4 Annealing

As the initial Ni-Mn depositions showed no trace of crystalline manganese containing material, one possible way to crystallize it is through heat-treatment. Nielsen *et al.* and Mattelaer *et al.* have already shown that the crystal structure of thd-precursor deposited β-MnO_2 changes drastically when heated to higher temperatures [125,127]. In addition, the research by Mattelaer's group revealed that different annealing atmospheres (oxidizing, reducing, and inert) induces different changes into the crystal structure of manganese oxide.

The annealings on the first thd-precursor batch were done as kind of a test to probe the possibilities annealing can offer to the samples. Just a few tries showed annealing has a notable effect on the samples seen as a color change visible to the naked eye but also as change in crystal structures. For example, an unannealed 100:100 Ni-Mn sample showed only the peaks of NiO before annealing but afterwards peaks belonging to Ni_6MnO_8 were clearly seen, shown in Figure 30. Other samples of the first batch behaved similarly under the heat treatment: new peaks appeared and the intensity of the peaks got higher but the change was most noticeable with the 100:100 Ni-Mn sample. One possible explanation for this kind of behavior is that most of the deposited manganese is initially in amorphous form and crystallizes to nickel manganese structures when the samples are annealed.

The initial annealing tests also revealed that annealing in temperatures over 1000 °C start to deteriorate the films. The deterioration can be seen as colorable cracks on the film and as decrease in the intensity of the peaks in the XRD. In addition, at temperatures over 1200 °C the films reacted with the Si substrate resulting in new phaces such as Mn_2SiO_4, shown in Figure 31.

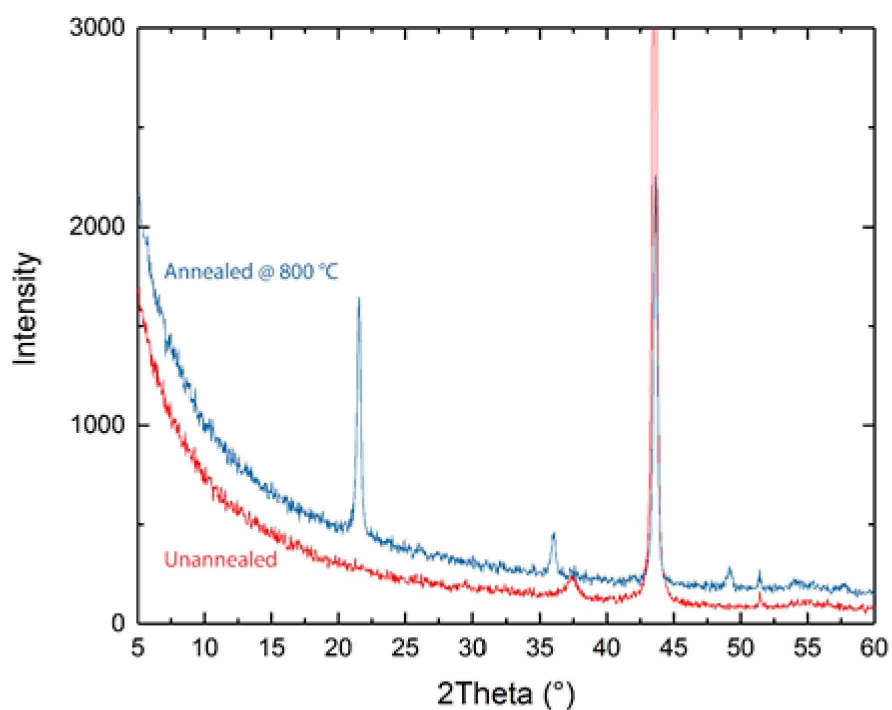

Figure 30. GIXRD of the same 100:100 Ni-Mn sample as deposited and annealed at 800 °C air for one hour.

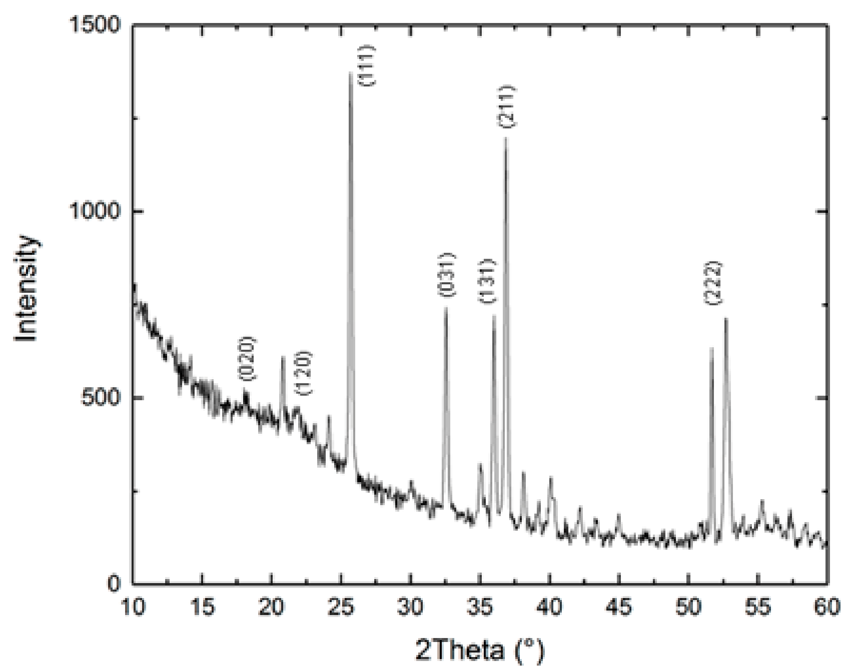

Figure 31. GIXRD pattern of a 1:10 Ni-Mn sample annealed for one hour in 1400 °C. Peaks of Mn_2SiO_4 marked with Miller indices.

The rest of the annealings were done with samples deposited from the second precursor batch and the different annealing atmospheres were also tested. As can be seen from the Figure 32, the different annealing atmospheres did not induce any notable effect on the crystallinity of the samples. The peaks are the same but the intensities differ a little: the most oxidizing (O_2) atmosphere having the highest peaks and the inert (N_2) atmosphere having the lowest. Oxidizing atmosphere evidently supports the crystallization of nickel manganese oxides. However, this effect was not seen on all the tested samples. The most substantial effect of the different annealing atmospheres was seen with the naked eye: N_2-atmosphere causes weird coloring and spots on the surface of the thin film.

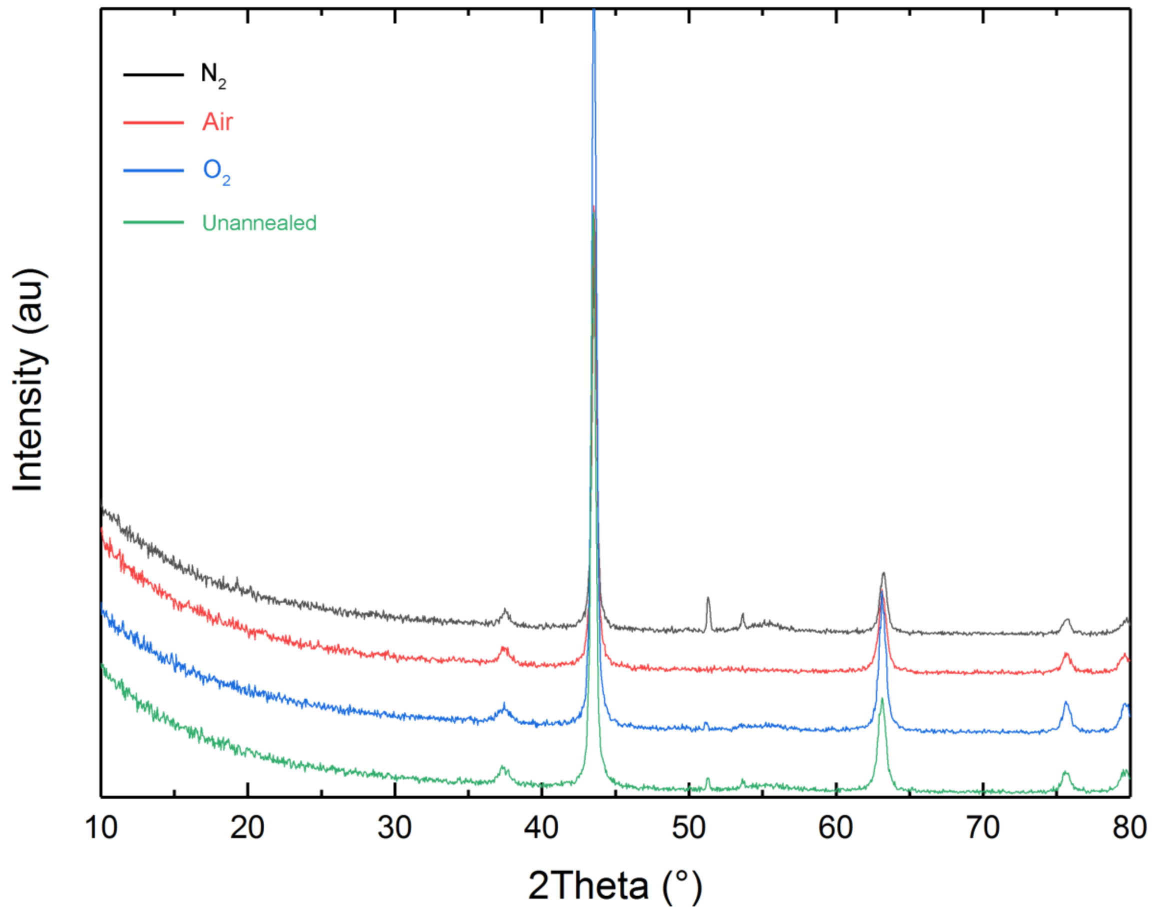

Figure 32. 1:20 Ni-Mn sample annealed in different atmospheres at 600 °C for 1 Hour. Green, blue, red, and black lines represent Unannealed, O_2, air, and N_2 annealed samples respectively. The peaks around 50 – 55 ° are caused by the Si-substrate.

Heat-treatment of different samples led to varying results. Annealing results of 1:20 Ni-Mn sample in different temperatures are given in Figure 33. Heat-treatment at 400 °C makes the $NiMn_2O_4$ peaks stronger but at 600 °C the crystal structure starts to change towards Ni_6MnO_8 as the intensities of the peaks lower in general and peaks belonging to Ni_6MnO_8 appear at 21 ° and 77 °. At 600 °C the structure is a mixture of $NiMn_2O_4$ and Ni_6MnO_8 as the pattern of $NiMn_2O_4$ are still visible. However, after heat-treatment at 800 °C there are no peaks belonging only to $NiMn_2O_4$ remaining which means that the structure has changed to Ni_6MnO_8.

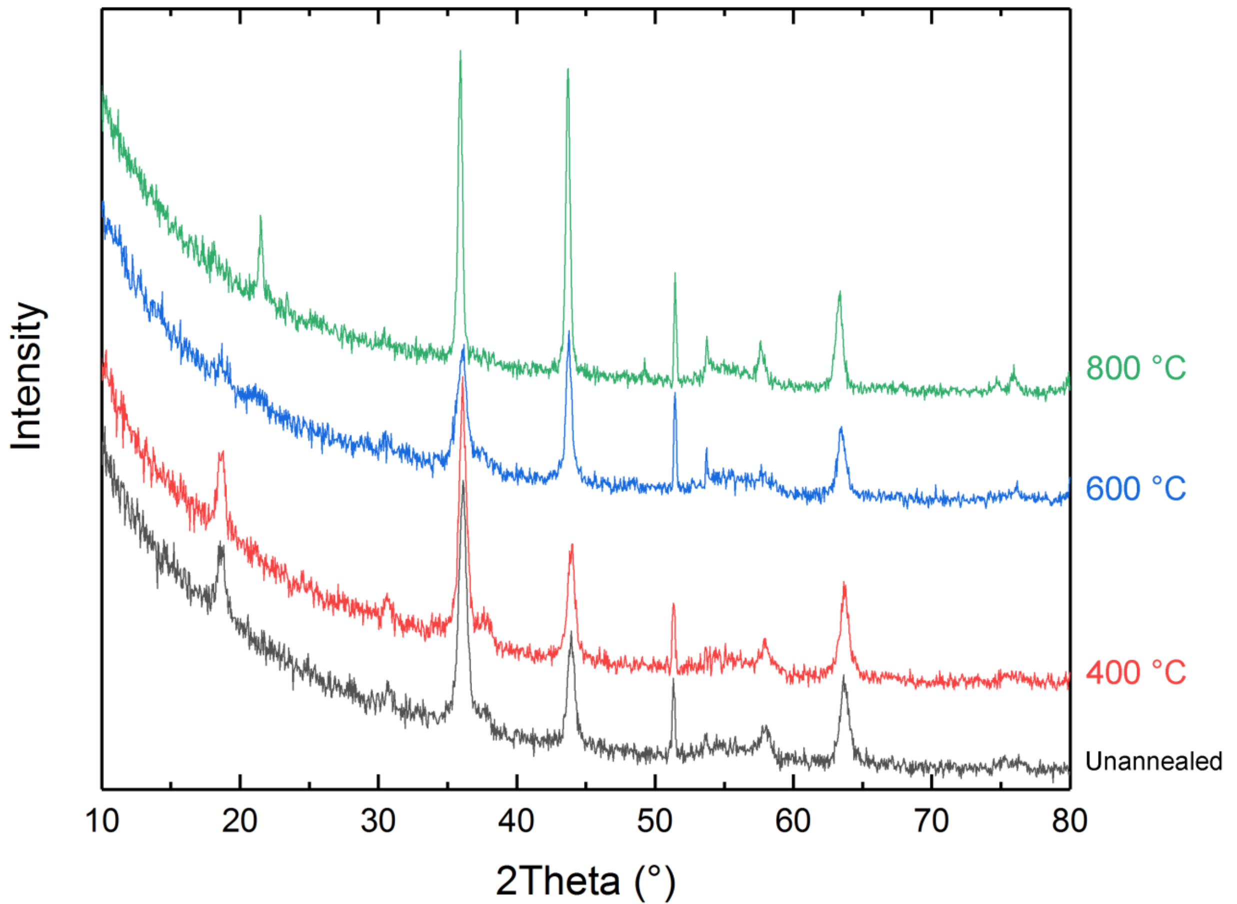

Figure 33. GIXRD patterns of 1:20 Ni-Mn sample annealed in air atmosphere for one hour at different temperatures.

In general, heat-treating at 400 °C made the spinel $NiMn_2O_4$ pattern of the samples from the second precursor batch more intense but at 600 °C the samples began to be a mixture of structures. Usually the structure of Ni_6MnO_8 showed up but in the sample containing most manganese (1:99 Ni-Mn) the pattern of $NiMnO_3$ appeared, shown in Figure 34. This signifies that all the different structures of nickel manganese oxides have been fabricated with the heat-treatment of the samples.

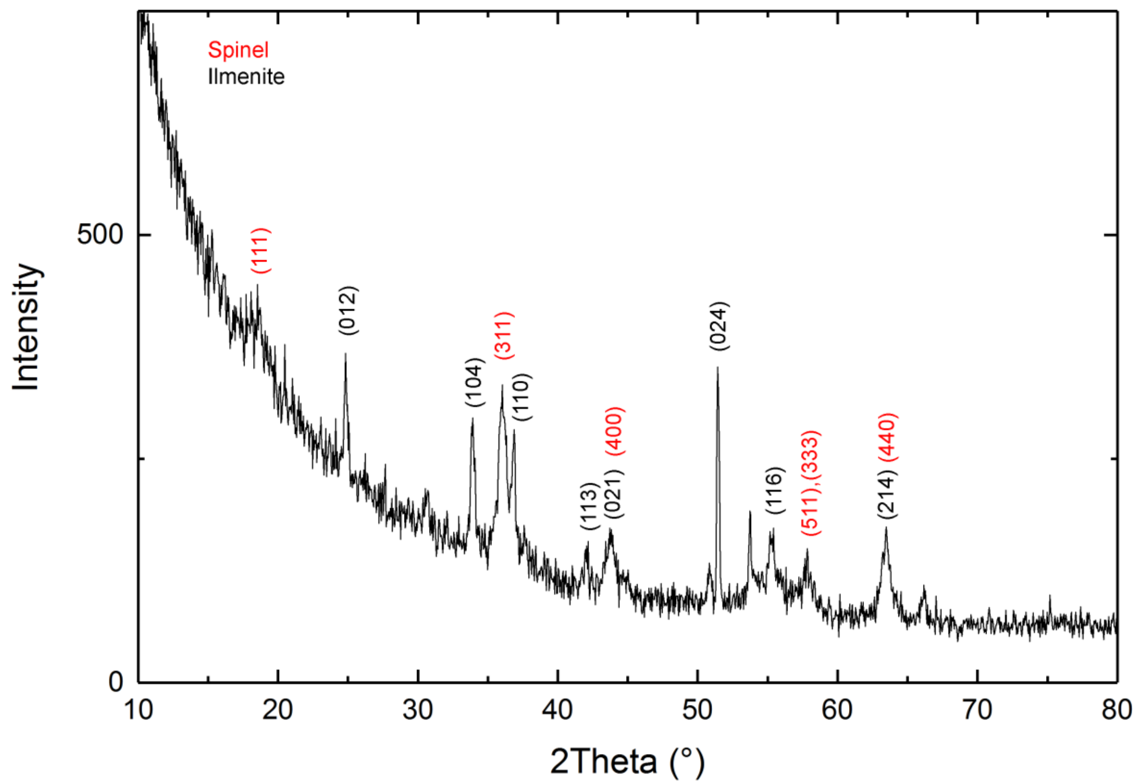

Figure 34. GIXRD pattern of 1:99 Ni-Mn sample annealed for one hour at 600 °C air. Peaks belonging to spinel $NiMn_2O_4$ and ilmenite $NiMnO_3$ marked with Miller indices.

8.5 Spectroscopy

Transmittance and reflectance measurements were conducted to investigate the differences in optical energy band gaps of depositions with different Ni-Mn ratios. Additionally, few prefatory measurements were conducted on the samples from the first batch, seen in Figure 35. The more detailed measurements were done on seven different glass samples before and after annealing in 400 °C for one hour. All the samples were from the second thd-precursor batch. The composition of the samples and the results of the measurement are gathered in the Table 1.

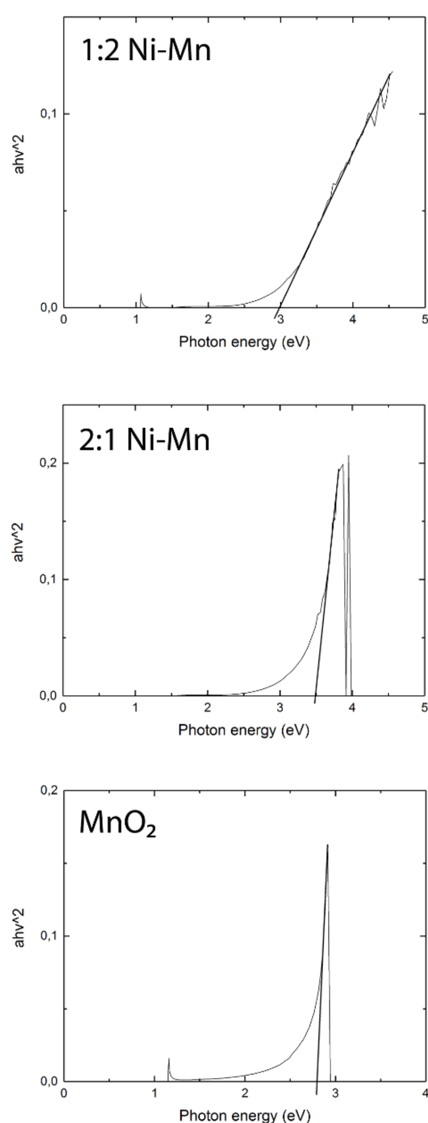

Figure 35. Optical band gaps measured from the first precursor patch. Determined by plotting $(\alpha h v)^{1/r}$ versus hv and extrapolating a straight line to cut the x-axis.

Table 1. The composition of the glass samples and results of the optical measurements.

Sample	Optical band gap	Optical band gap after annealing
1:1 Ni-Mn	4.84 eV	4.82 eV
1:3 Ni-Mn	4.62 eV	4.82 eV
1:10 Ni-Mn	4.88 eV	4.86 eV
1:20 Ni-Mn	4.91 eV	4.83 eV
1:99 Ni-Mn	4.66 eV	4.64 eV
20:20 Ni-Mn	4.71 eV	4.57 eV
MnO_2	4.79 eV	4.64 eV

The initial measurements presented on Figure 35 show clear differences in the optical band gaps. 1:2 Ni-Mn sample has an optical band gap of 3.0 eV, 2:1 Ni-Mn sample has a gap of 3.5 eV and the MnO_2 sample had the lowest gap of 2.8 eV. Based only on these measurements one could say that increase in the nickel content of the samples increases the optical band gap. However, the more accurate measurements done to confirm this failed.

As can be seen from the table 1, all the samples have similar optical band gaps before and after annealing. The heat treatment lowered the optical band gaps by a marginal amount. No resemblance can be found between the ratios of the samples and the optical band gap. The results are probably from the glass substrate showing only its absorbance.

The initial measurements in Figure 35 are somewhat in line with the literature as higher nickel count raises the band gap and the optical band gap of MnO_2 is close to the literature value. Khodair *et al.* got results around 3.6 eV with samples having less than 10 % manganese and Larbi *et al.* got band gaps around 2 eV with samples containing less than 5 % nickel [136,137]. Hendi *et al*. measured optical band gaps between 2.6 – 2.7 eV for MnO_2 thin films [141]. Clearly, the results from the literature indicate that higher nickel ratio increases the band gap. In Table 2, the band gaps are too large for the presented Ni-Mn ratios. Nevertheless, as it has been speculated earlier, it is possible that the actual amount of nickel is higher because the deposition rate of the manganese was so low.

8.6 Magnetic measurements

Zero-field-cooled, field-cooled and magnetic hysteresis measurements were done on a few carefully chosen samples. The chosen samples represented all the common different structures seen during depositions: strong spinel structure (1:20 Ni-Mn sample annealed at 400 °C for 1 hour), spinel with more intense peaks of NiO (1:3 Ni-Mn sample annealed at 400 °C for 1 hour), spinel with some ilmenite structure (1:99 Ni-Mn sample annealed at 800 °C for 1 hour), and a sample with strong NiO pattern (1:1 Ni-Mn sample unannealed). The strong NiO patterned sample turned out not to be magnetic so there results for the sample are not shown. The ZFC and FC results of the magnetic measurements of the strong spinel sample are in Figure 36, results of the NiO/spinel are in Figure 37, and results for the spinel/ilmenite sample are shown in Figure 38. The negative values of magnetic moment are because of dielectric background caused by Si-substrate.

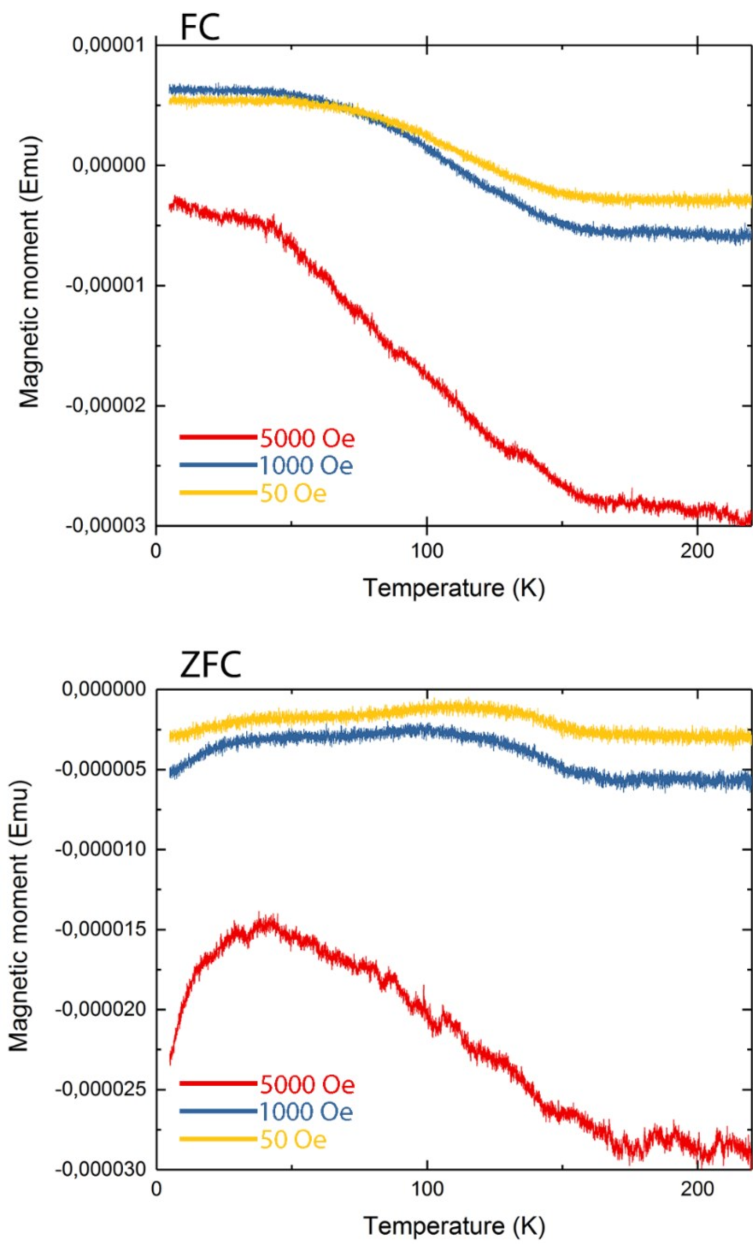

Figure 36. FC and ZFC measurements of the NiO/spinel sample.

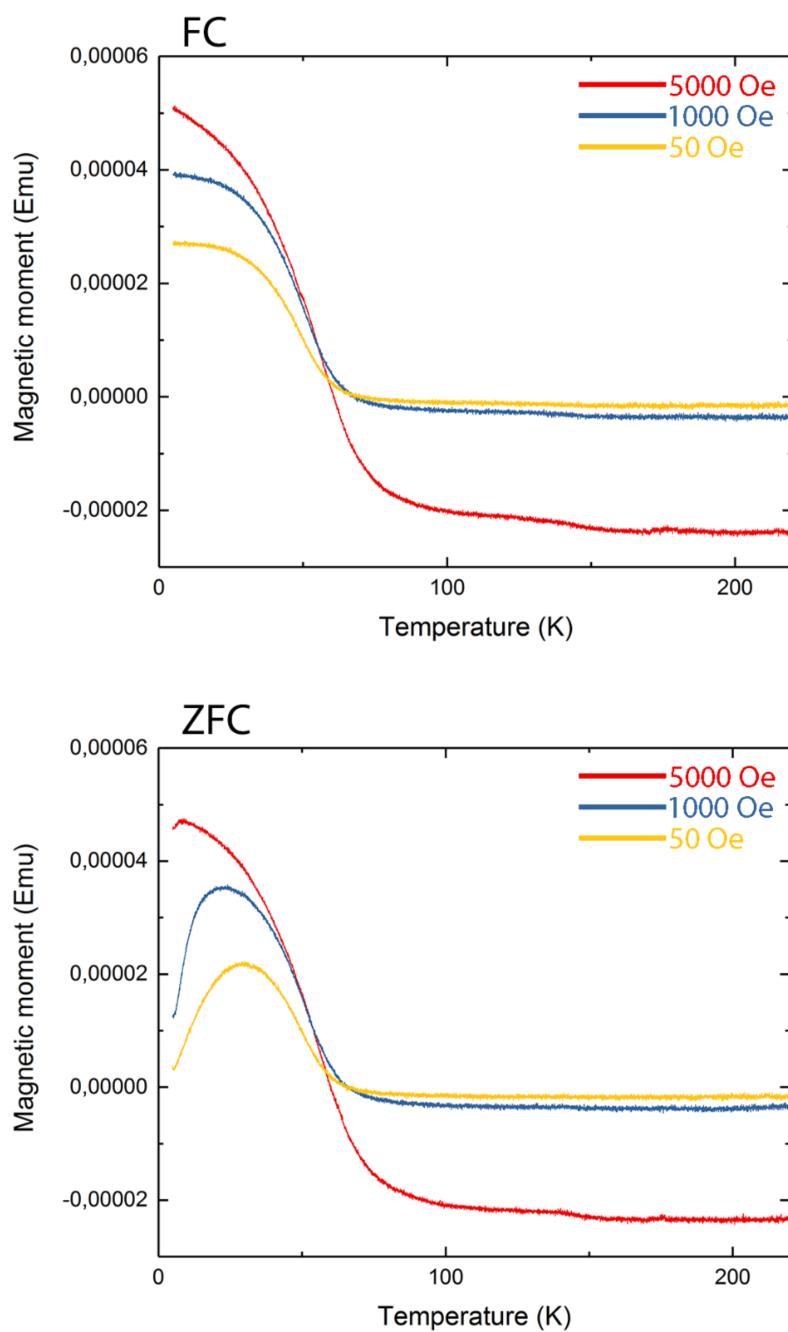

Figure 37. FC and ZFC measurements of the strong spinel sample.

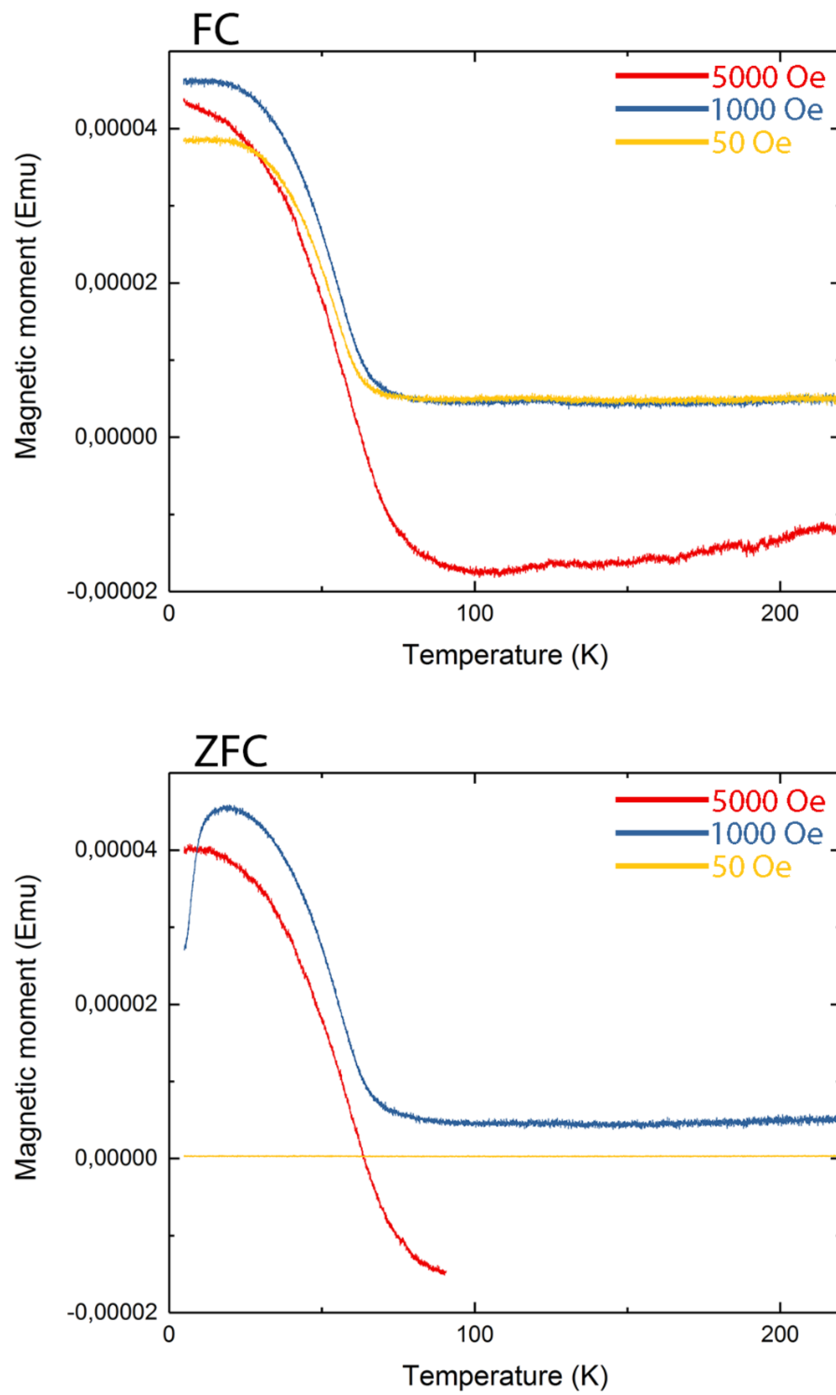

Figure 38. FC and ZFC measurements of the spinel/ilmenite sample. (The device malfunctioned during the 5000 Oe measurement)

The FC and ZFC measurements of the strong spinel (Figure 37) and spinel/ilmenite (Figure 38) samples show a clear magnetic transition from ferromagnetism to paramagnetism. It happens around 70 – 80 K for both of the samples in both measurements being little higher for the ilmenite containing sample. Ilmenite $NiMnO_3$ has a higher critical temperature than the spinel $NiMn_2O_4$ so the higher transition temperature of spinel/ilmenite sample is logical. On the other hand, the NiO/spinel sample showed a magnetic transition around 140 – 150 K but not as steep and clear as the other two other samples. The slower decrease of the magnetic moment may be explained with ferromagnetic and antiferromagnetic sublattices caused by composition of the sample being partly a nickel manganese oxide and partly NiO. The obtained results are in line with the literature: For example, Menaka *et al*. got values ranging between 72 – 145 K for the magnetic transition in their nanostructured $NiMn_2O_4$ samples [70].

Similar kind of behavior is seen on the magnetic hysteresis loops of the samples, Figure 39. The spinel and spinel/ilmenite structured samples have sharp hysteresis loops typical for ferrimagnetic materials. The spinel sample reaches saturation faster but the spinel/ilmenite sample has a higher magnetization and a sharper curve which is in line with He *et al*. results obtained at higher temperatures [108]. The magnetic moment of the two samples changes quickly with the applied magnetic field (soft magnetic material) reaching saturation around 10 – 15 kOe field. The magnetic hysteresis loop of NiO/spinel sample differs a lot from the other; it has a higher coercivity, lower magnetization, and the magnetic moment is not saturated even on the higher magnetic fields. This behavior is attributed to NiO impurities by Díez *et al*. in their $NiMn_2O_4$ studies [138]. Thus, the magnetic hysteresis loops are in line with the literature and the differences in the hysteresis loops can be easily explained by the NiO and ilmenite patterns seen on the samples.

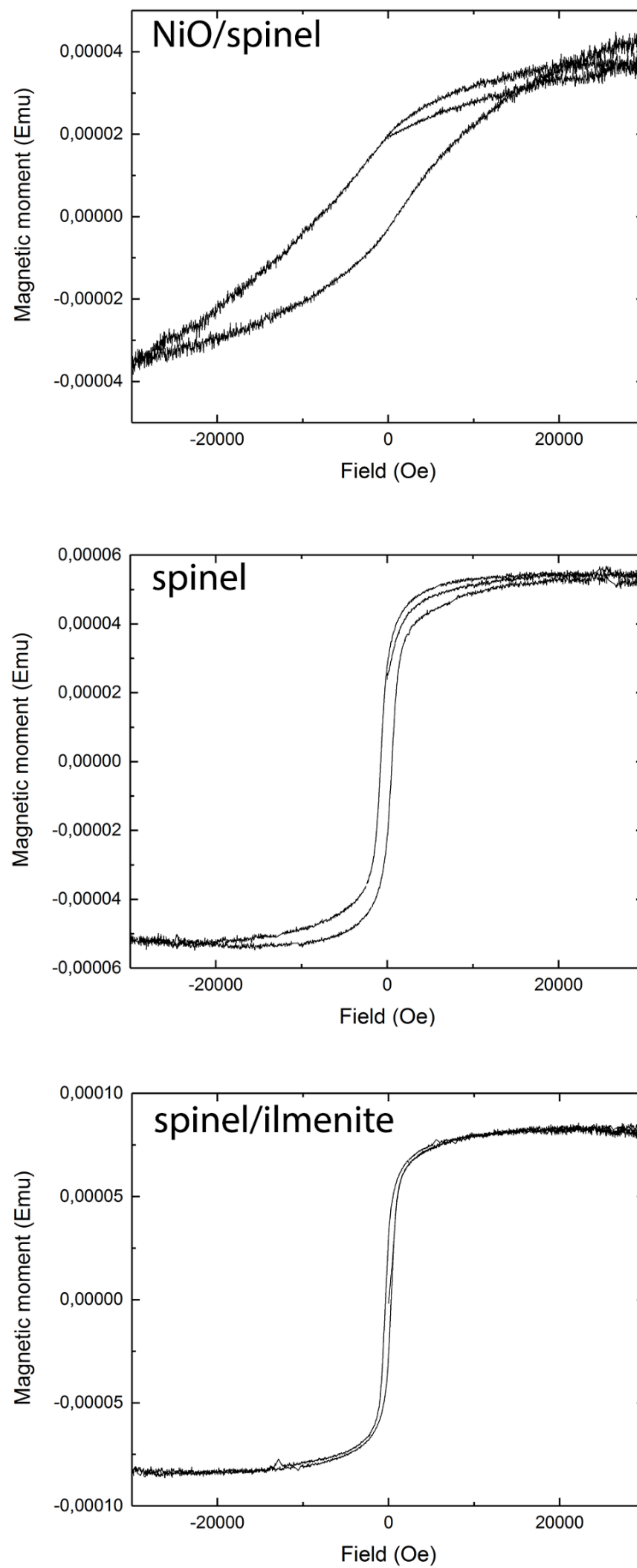

Figure 39. Magnetic hysteresis loops of samples measured in 10 K.

9 Conclusions

After finding optimized deposition parameters for the ALD of nickel oxide and manganese oxide separately using thd-precursors, both were deposited during the same run to fabricate a ternary oxide thin film. The thin films were investigated with XRR and XRD to know their quality and crystal structure. The results changed dramatically using different in-lab synthetized $Mn(thd)_3$ precursors. The samples made of the first $Mn(thd)_3$ precursor batch only showed the XRD-pattern of nickel oxide even when depositing 10 cycles of manganese for every cycle of nickel, whereas XRD revealed that almost all the samples made of the second batch contained at least some crystalline $NiMn_2O_4$. The peaks were already visible with 1:3 Ni-Mn ratio in some depositions. The second batch of $Mn(thd)_3$ looked worse with the naked-eye because it seemed like a mixture of black $Mn(thd)_3$ and traces of some other yellow powder but still it performed better. As the first precursor powder was exhausted before doing the second batch, no comparison could be made for the powders but clearly there was some substantial difference in them.

One hour heat-treatment in over 500 °C temperature changed the XRD-pattern in almost all samples to show peaks belonging to $NiMn_2O_4$. Also, peaks of Ni_6MnO_8 were found and one sample showed peaks belonging to $NiMnO_3$. Evidently, even the samples made from the first precursor batch contained manganese but either it could not be observed behind the strong NiO XRD-pattern or the manganese was in an amorphous form distributed into the NiO crystal structure. The heat-treatment made the manganese crystallize and changed the overall crystal structure which could also be observed as a color change of the thin films. Different heat-treating atmospheres did not influence the crystal structure of the samples but nitrogen atmosphere caused deterioration on the surfaces of the thin films.

Based on the XRD-results alone, it cannot be fully confirmed if the samples are purely in spinel form because the pattern of NiO and pattern of each different nickel manganese oxide overlap partly. However, the XRD-results confirmed that thin films containing $NiMn_2O_4$ had been deposited with ALD. In most cases, it was necessary to heat-treat the samples first but some thin films grew straight into the spinel structure during the ALD. Also, it was confirmed that Ni_6MnO_8 and $NiMnO_3$ thin films can be made by heat-treating the samples deposited with ALD.

The magnetic hysteresis loops and ZFC/FC measurements showed distinct differences in differently structured samples. The results matched with literature thus confirming the composition of the samples. The NiO XRD-patterned sample was not magnetic confirming that it was only nickel oxide. The samples that show clear XRD-pattern of $NiMn_2O_4$ actually are $NiMn_2O_4$ and the ones having more NiO pattern contain some NiO. It is then certainly confirmed that $NiMn_2O_4$ thin films can be deposited with ALD.

Most likely due to problems related to the precursor or the fact that a strong oxidizer like ozone was used, the ALD-reaction did not work ideally. There was deviation in the quality of the thin films but also inconsistency between similar depositions. It is possible that precursor material with impurities could cause CVD kind of reactions where the different precursor materials react together on the surface of the substrate instead of reacting with the substrate like in ALD. Ozone decomposes easily in high temperatures and manganese oxide is a known catalyst for the decomposing of ozone so it could be that there were problems in the oxidization step of the ALD-reaction.

The initial optic band gap measurements seemed promising showing similar magnitude band gaps as in literature. The measurements done with the more accurate spectrometer showed weird results that were probably wrong. There were problems getting readings of the resistances of the thin films and not all samples were even conductive.

10 Further research

To continue research on ALD of nickel manganese oxides it would be essential to perform X-ray photoelectron spectroscopy (XPS) measurements on few of the deposited thin films. This would tell the exact ion composition of the samples and would be the best confirmation for the spinel structure. Even though the magnetic measurements strongly suggest that the sample is spinel $NiMn_2O_4$, XPS would be the ultimate confirmation that the samples were in spinel phase instead of being a mixture of spinel and NiO structures.

More measurements could be done on the samples. As most of the applications for ternary oxides are electronic devices, it would be important to measure some of the electrical properties of the samples. For example, capacitance and resistances could be measured. Also, the samples' ability to catalyze oxygen evolution and oxygen reduction reactions should be measured since a mixture of $NiMn_2O_4$ and $NiMnO_3$ structures have performed well when fabricated differently [108].

For future manganese depositions, it is important to further optimize the ALD-reactor and the manganese precursor material. The two patches of in-lab synthetized $Mn(thd)_3$ precursor had very different results and the growth rates were very low with all parameters. On the other hand, the quick test depositions made with purchased $Mn(acac)_2$ seemed promising even though the high deposition temperatures caused difficulties. One should continue working with $Mn(acac)_2$ and try with some of the other available precursor options such as $Mn(EtCp)_2$. Problems caused by the high temperature differences required for the depositions with $Mn(acac)_2$ precursor could be easily solved with different reactor configuration. If the reactor chamber and the precursors were heated independently, there would be no such problems. The precursor problem could also be solved by using bubblers or other similar devices as they make it possible to use different precursors and potentially increase the concentration of the precursor going to the substrate.

The spinel $NiMn_2O_4$ has been utilized in combination with lithium as cathode material in high energy density Li-ion batteries. If a deposition of nickel and manganese works with additional lithium, atomic layer deposited Li-ion batteries could be one possible practical application to endeavor. Also, $LiMnO_4$ is used as cathode material so it could be

interesting to try to deposit this with ALD. Lithium-containing materials have been deposited with ALD but there seem to be no articles about ALD of $LiMnO_4$.

References

[1] Malygin, A. A., Drozd, V. E., Malkov, A. A., and Smirnov, V. M., From V. B. Aleskovskii's "framework" hypothesis to the method of molecular layering/atomic layer deposition, *Chem. Vap. Depos.* **21** (2015) 216–240.

[2] T. Suntola, J. A., International patent, FIN 52359, US 4 058 430, priority Nov 29, 1974, publication Nov 15, 1977., 1977.

[3] Puurunen, R. L., A short history of atomic layer deposition: Tuomo Suntola's atomic layer epitaxy, *Chem. Vap. Depos.* **20** (2014) 332–344.

[4] Leskelä, M., and Ritala, M., Atomic layer deposition chemistry: Recent developments and future challenges, *Angew. Chemie - Int. Ed.* **42** (2003) 5548–5554.

[5] George, S. M., Atomic layer deposition: An overview, *Chem. Rev.* (2010).

[6] Sneh, O., Clark-Phelps, R. B., Londergan, A. R., Winkler, J., and Seidel, T. E., Thin film atomic layer deposition equipment for semiconductor processing, *Thin Solid Films* **402** (2002) 248–261.

[7] Miikkulainen, V., Leskelä, M., Ritala, M., and Puurunen, R. L., Crystallinity of inorganic films grown by atomic layer deposition: Overview and general trends, *J. Appl. Phys.* **113** (2013).

[8] Vahlas, C., Caussat, B., Gladfelter, W. L., Senocq, F., and Gladfelter, E. J., Liquid and solid precursor delivery systems in gas phase processes, *Recent Patents Mater. Sci.* **8** (2015) 91–108.

[9] O'Brien, P., Pickett, N. L., and Otway, D. J., Developments in CVD delivery systems: A chemist's perspective on the chemical and physical interactions between precursors, *Chem. Vap. Depos.* **8** (2002) 237–249.

[10] Ting Kai, L., and Scott, D., Liquid vaporizer system and method, 5,835,678, 1998.

[11] Leskelä, M., and Ritala, M., Atomic layer deposition (ALD): From precursors to thin film structures, in *Thin Solid Films*, 2002, 138–146.

[12] Profijt, H. B., Potts, S. E., van de Sanden, M. C. M., and Kessels, W. M. M., Plasma-assisted atomic layer deposition: Basics, oOpportunities, and challenges, *J. Vac. Sci. Technol. A Vacuum, Surfaces, Film.* **29** (2011) 50801.

[13] Puurunen, R. L., Surface chemistry of atomic layer deposition: A case study for the trimethylaluminum/water process, *J. Appl. Phys.* **97** (2005) 1–37.

[14] Sundberg, P., and Karppinen, M., Organic and inorganic–organic thin film structures by molecular layer deposition: A review, *Beilstein J. Nanotechnol.* **5** (2014) 1104–1136.

[15] George, S. M., Yoon, B., and Dameron, A. A., Surface chemistry for molecular layer deposition of organic and hybrid organic - inorganic polymers, *Acc. Chem. Res.* **42** (2009) 498–508.

[16] Musat, V., Fortunato, E., Fernandes, F. B., and Cordeiro, R. J., Sol gel porous ZnO thin films for gas sensing applications, *J. Optoelectron. Adv. Mater.* **9** (2007) 1395–1398.

[17] Franssila, S., *Introduction to Microfabrication*, 2nd ed., John Wiley & Sons, Ltd, 2004.

[18] Ghosh, R., Basak, D., and Fujihara, S., Effect of substrate-induced strain on the structural, electrical, and optical properties of polycrystalline ZnO thin films, *J. Appl. Phys.* **96** (2004) 2689–2692.

[19] Jones, A. O. F., Chattopadhyay, B., Geerts, Y. H., and Resel, R., Substrate-induced and thin-film phases: Polymorphism of organic materials on surfaces, *Adv. Funct. Mater.* **26** (2016) 2233–2255.

[20] Ong, B. S., Pey, K. L., Ong, C. Y., Tan, C. S., Antoniadis, D. A., and Fitzgerald, E. A., Comparison between chemical vapor deposited and physical vapor deposited WSi2 metal gate for InGaAs n-metal-oxide-semiconductor field-effect transistors, *Appl. Phys. Lett.* **98** (2011) 182102.

[21] Rui, M., Li, X., Gan, L., Zhai, T., and Zeng, H., Ternary oxide nanocrystals: Universal laser-hydrothermal synthesis, pptoelectronic and electrochemical applications, *Adv. Funct. Mater.* **26** (2016) 5051–5060.

[22] Chen, D., Wang, Q., Wang, R., and Shen, G., Ternary oxide nanostructured materials for supercapacitors: a review, *J. Mater. Chem. A* **3** (2015) 10158–10173.

[23] Parthiban, S., and Kwon, J.-Y., Role of dopants as a carrier suppressor and strong oxygen binder in amorphous indium-oxide-based field effect transistor, *J. Mater. Res.* **29** (2014) 1585–1596.

[24] Sønsteby, H. H., Fjellvåg, H., and Nilsen, O., Functional perovskites by atomic layer deposition - an overview, *Adv. Mater. Interfaces* (2017) 1600903.

[25] Vasala, S., and Karppinen, M., A2B′B″O6 perovskites: A review, *Prog. Solid State Chem.* **43** (2015) 1–36.

[26] Johnsson, M., and Lemmens, P., Crystallography and chemistry of perovskites, in *Handb. Magn. Adv. Magn. Mater.*, John Wiley & Sons, Ltd, Chichester, UK, 2007, 11.

[27] Ito, Y., and Uchino, K., Piezoelectricity, in *Encycl. RF Microw. Eng.*, John Wiley & Sons, Inc., Hoboken, NJ, USA, 2005.

[28] Bersuker, I. B., Modern aspects of the Jahn−Teller effect theory and applications to molecular problems, *Chem. Rev.* **101** (2001) 1067–1114.

[29] Hill, N. A., Why are there so few magnetic ferroelectrics?, *J. Phys. Chem. B* **104** (2000) 6694–6709.

[30] Wang, Q. H., Kalantar-Zadeh, K., Kis, A., Coleman, J. N., and Strano, M. S., Electronics and optoelectronics of two-dimensional transition metal dichalcogenides, *Nat. Nanotechnol.* **7** (2012) 699–712.

[31] Sawada, M., Higuchi, M., Kondo, S., and Saka, H., Characteristics of indium-tin-oxide/silver/indium-tin-oxide sandwich films and their application to simple-matrix liquid-crystal displays, *Jpn. J. Appl. Phys.* **40** (2001) 3332–3336.

[32] Minami, T., Substitution of transparent conducting oxide thin films for indium tin oxide transparent electrode applications, *Thin Solid Films* **516** (2008) 1314–1321.

[33] Granqvist, C. G., and Hultåker, A., Transparent and conducting ITO films: new developments and applications, *Thin Solid Films* **411** (2002) 1–5.

[34] Ohta, H., and Hosono, H., Transparent oxide optoelectronics, *Mater. Today* **7** (2004) 42–51.

[35] Bae, K., Jang, D. Y., Choi, H. J., Kim, D., Hong, J., Kim, B.-K., et al., Demonstrating the potential of yttrium-doped barium zirconate electrolyte for high-performance fuel cells, *Nat. Commun.* **8** (2017) 14553.

[36] Fabbri, E., Magrasó, A., and Pergolesi, D., Low-temperature solid-oxide fuel cells based on proton-conducting electrolytes, *MRS Bull.* **39** (2014) 792–797.

[37] Sengodan, S., Choi, S., Jun, A., Shin, T. H., Ju, Y.-W., Jeong, H. Y., et al., Layered oxygen-deficient double perovskite as an efficient and stable anode for direct hydrocarbon solid oxide fuel cells, *Nat. Mater.* **14** (2014) 205–209.

[38] Mai, L.-Q., Yang, F., Zhao, Y.-L., Xu, X., Xu, L., and Luo, Y.-Z., Hierarchical MnMoO4/CoMoO4 heterostructured nanowires with enhanced supercapacitor performance, *Nat. Commun.* **2** (2011) 381.

[39] Zhi, M., Xiang, C., Li, J., Li, M., and Wu, N., Nanostructured carbon–metal oxide composite electrodes for supercapacitors: a review, *Nanoscale* **5** (2013) 72–88.

[40] Zhao, C., Zhao, C. Z., Werner, M., Taylor, S., and Chalker, P. R., Advanced CMOS Gate Stack: Present Research Progress, *ISRN Nanotechnol.* **2012** (2012) 1–35.

[41] Lopes, J. M. J., Durğun Özben, E., Roeckerath, M., Littmark, U., Lupták, R., Lenk, S., et al., Amorphous ternary rare-earth gate oxides for future integration in MOSFETs, *Microelectron. Eng.* **86** (2009) 1646–1649.

[42] Zhao, C., Zhao, C. Z., Tao, J., Werner, M., Taylor, S., and Chalker, P. R., Dielectric relaxation of lanthanide-based ternary oxides: Physical and mathematical models, *J. Nanomater.* **2012** (2012) 1–6.

[43] Rapoport, W. R., and Khattak, C. P., Titanium sapphire laser characteristics, *Appl. Opt.* **27** (1988) 2677.

[44] Wang, Q.-Y., Li, Z., Zhang, W.-H., Zhang, Z.-C., Zhang, J.-S., Li, W., et al., Interface-induced high-temperature superconductivity in single unit-cell FeSe films on SrTiO3, *Chinese Phys. Lett.* **29** (2012) 37402.

[45] Ohta, H., Kim, S., Mune, Y., Mizoguchi, T., Nomura, K., Ohta, S., et al., Giant

thermoelectric Seebeck coefficient of a two-dimensional electron gas in SrTiO3, *Nat. Mater.* **6** (2007) 129–134.

[46] Haeni, J. H., Irvin, P., Chang, W., Uecker, R., Reiche, P., Li, Y. L., et al., Room-temperature ferroelectricity in strained SrTiO3, *Nature* **430** (2004) 758–761.

[47] Brinkman, a, Huijben, M., van Zalk, M., Huijben, J., Zeitler, U., Maan, J. C., et al., Magnetic effects at the interface between non-magnetic oxides, *Nat. Mater.* **6** (2007) 493–496.

[48] Santander-Syro, A. F., Copie, O., Kondo, T., Fortuna, F., Pailhès, S., Weht, R., et al., Two-dimensional electron gas with universal subbands at the surface of SrTiO3, *Nature* **469** (2011) 189–193.

[49] Tanskanen, J. T., Hagglund, C., and Bent, S. F., Correlating growth characteristics in atomic layer deposition with precursor molecular structure: The case of zinc tin oxide, *Chem. Mater.* **26** (2014) 2795–2802.

[50] Elliott, S. D., and Nilsen, O., Reaction mechanisms in ALD of ternary oxides, in 2011, 175–183.

[51] Putkonen, M., Development of low-temperature deposition processes by atomic layer epitaxy for binary and ternary oxide thin films development of low-temperature deposition processes by atomic layer epitaxy for binary and ternary oxide thin films, Helsinki University of Technology, (2002).

[52] Wiemer, C., Lamagna, L., and Fanciulli, M., Atomic layer deposition of rare-earth-based binary and ternary oxides for microelectronic applications, *Semicond. Sci. Technol.* **27** (2012) 74013.

[53] Sánchez, F., Ocal, C., and Fontcuberta, J., Tailored surfaces of perovskite oxide substrates for conducted growth of thin films, *Chem. Soc. Rev.* **43** (2014) 2272.

[54] Sinha, A. P. B., N. R. Sanjana, and A. B. Biswas. “On the structure of some anganites.” Acta Crystallographica 10.6 (1957): 439-440., (n.d.).

[55] Scerri, E., *The Periodic Table: Its Story and Its Significance*, Oxford University Press, Inc., New york, 2007.

[56] Liu, E.-H., Li, W., Li, J., Meng, X.-Y., Ding, R., and Tan, S.-T., Preparation and

characterization of nanostructured NiO/MnO2 composite electrode for electrochemical supercapacitors, *Mater. Res. Bull.* **44** (2009) 1122–1126.

[57] Nguyen, T., Boudard, M., Rapenne, L., Carmezim, M. J., and Montemor, M. F., Morphological changes and electrochemical response of mixed nickel manganese oxides as charge storage electrodes, *J. Mater. Chem. A* **3** (2015) 10875–10882.

[58] Christel, L., Pierre, A., and Abel, D. A.-M. R., Temperature programmed reduction studies of nickel manganite spinels, *Thermochim. Acta* **306** (1997) 51–59.

[59] Kjellqvist, L., and Selleby, M., Thermodynamic assessment of the Mn–Ni–O system, *Int. J. Mater. Res.* **101** (2010) 1222–1231.

[60] Datta, P. K., Klusek, Z., Basu, A., and Brinkman, A. W., Nanoscale studies of morphological and electrical properties of NixMn3-xO3-δ (0.4≤x≤1) thin films by in-situ high temperature scanning tunneling microscopy and spectroscopy, *Surf. Coatings Technol.* **187** (2004) 161–166.

[61] Fau, P., Bonino, J. P., Demai, J. J., and Rousset, A., Thin films of nickel manganese oxide for NTC thermistor applications, *Appl. Surf. Sci.* **65**–**66** (1993) 319–324.

[62] Baudour, J. L., Bouree, F., Fremy, M. A., Legros, R., Rousset, A., and Gillot, B., Cation distribution and oxidation states in nickel manganites NiMn2O4 and Ni0.8Mn2.2O4 from powder neutron diffraction, *Phys. B Phys. Condens. Matter* **180**–**181** (1992) 97–99.

[63] Fritsch, S., Sarrias, J., Brieu, M., Couderc, J. J., Baudour, J. L., Snoeck, E., et al., Correlation between the structure, the microstructure and the electrical properties of nickel manganite negative temperature coefficient (NTC) thermistors, *Solid State Ionics* **109** (1998) 229–237.

[64] Aleksic, O. S., Nikolic, M. V., Lukovic, M. D., Nikolic, N., Radojcic, B. M., Radovanovic, M., et al., Preparation and characterization of Cu and Zn modified nickel manganite NTC powders and thick film thermistors, *Mater. Sci. Eng. B Solid-State Mater. Adv. Technol.* **178** (2013) 202–210.

[65] Sagua, A., Lescano, G. M., Alonso, J. A., Martínez-Coronado, R., Fernández-Díaz, M. T., and Morán, E., Neutron structural characterization, inversion degree and transport properties of NiMn2O4 spinel prepared by the hydroxide route, *Mater.*

Res. Bull. **47** (2012) 1335–1338.

[66] Iguchi, E., Ueda, K., and Jung, W., Conduction in LaCoO3 by small-polaron hopping below room temperature, *Phys. Rev. B* **54** (1996) 17431–17437.

[67] Basu, A., Brinkman, A. W., Klusek, Z., Datta, P. K., and Kowalczyk, P., In situ study of the effect of temperature on the electronic structure of NixMn3-xO4+delta thin films using scanning tunneling spectroscopy, *J. Appl. Phys.* **92** (2002) 4123–4125.

[68] Liu, H., Pourret, A., and Guyot-Sionnest, P., Mott and Efros-Shklovskii variable range hopping in CdSe quantum dots films, *ACS Nano* **4** (2010) 5211–5216.

[69] Ma, C., Liu, Y., Lu, Y., and Qian, H., Preparation and electrical properties of Ni0.6Mn2.4−xTixO4 NTC ceramics, *J. Alloys Compd.* **650** (2015) 931–935.

[70] Menaka, Garg, N., Kumar, S., Kumar, D., Ramanujachary, K. V., Lofland, S. E., et al., Nanostructured nickel manganese oxide: aligned nanostructures and their magnetic properties, *J. Mater. Chem.* **22** (2012) 18447.

[71] Peña, O., Moure, C., Bodenez, V., Cailleaux, X., Piriou, B., Ortiz, J., et al., Magnetic properties of spinel-type oxides NiMn2-xMexO4, *J. Chil. Chem. Soc.* **50** (2005) 617–623.

[72] Cloud, W. H., Crystal Structure and Ferrimagnetism in NiMnO3 and CoMnO3, *Phys. Rev.* **111** (1958) 1046–1049.

[73] Hong, D., Yamada, Y., Nomura, A., and Fukuzumi, S., Catalytic activity of NiMnO3 for visible light-driven and electrochemical water oxidation, *Phys. Chem. Chem. Phys.* **15** (2013) 19125.

[74] Mathieu, R., Ivanov, S. A., Solovyev, I. V., Bazuev, G. V., Anil Kumar, P., Lazor, P., et al., Mn2FeSbO6: a ferrimagnetic ilmenite and an antiferromagnetic perovskite R., *Phys. Rev. B* **87** (2013) 14408.

[75] Mehandjiev, D., Zhecheva, E., Ivanov, G., and Ioncheva, R., Preparation and catalytic activity of nickel–manganese oxide catalysts with an ilmenite-type structure in the reactions of complete oxidation of hydrocarbons, *Appl. Catal. A Gen.* **167** (1998) 277–282.

[76] Yu, J., Yan, Q., Chen, W., Jain, A., Neaton, J. B., and Persson, K. a., First-principles

study of electronic structure and photocatalytic properties of MnNiO3 as an alkaline oxygen-evolution photocatalyst, *Chem. Commun.* **51** (2015) 2867–2870.

[77] Porta, P., Minelli, G., Botto, I. L., and Baran, E. J., Structural, magnetic, and optical investigation of Ni6MnO8, *J. Solid State Chem.* **92** (1991) 202–207.

[78] Alcántara, R., Jaraba, M., Lavela, P., and Tirado, J. L., New NixMg6−xMnO8 mixed oxides as active materials for the negative electrode of lithium-ion cells, *J. Solid State Chem.* **166** (2002) 330–335.

[79] Taguchi, H., Omori, S., Nagao, M., Kido, H., and Shimada, M., Crystal structure and magnetic properties of (Ni1-x]Mgx)6MnO8, *J. Solid State Chem.* **118** (1995) 112–116.

[80] Taguchi, H., Relationship between crystal structure and electrical properties of murdochite-type Ni6+2xMn1−xO8, *Solid State Commun.* **108** (1998) 635–639.

[81] Taguchi, H., Tahara, S., Okumura, M., and Hirota, K., Synthesis of murdochite-type Ni6MnO8 with variable specific surface areas and the application in methane oxidation, *J. Solid State Chem.* **215** (2014) 300–304.

[82] Golestani-Fard, F., Azimi, S., and Mackenzie, K. J. D., Oxygen evolution during the formation and sintering of nickel-manganese oxide spinels for thermistor applications, *J. Mater. Sci.* **22** (1987) 2847–2851.

[83] Fang, D. L., Zheng, C. H., Chen, C. S., and Winnubst, A. J. A., Aging of nickel manganite NTC ceramics, *J. Electroceramics* **22** (2009) 421–427.

[84] Parlak, M., Hashemi, T., Hogan, M. J., and Brinkman, A. W., Effect of heat treatment on nickel manganite thin film thermistors deposited by electron beam evaporation, *Thin Solid Films* **345** (1999) 307–311.

[85] Ko, S. W., Li, J., Podraza, N. J., Dickey, E. C., and Trolier-Mckinstry, S., Spin spray-deposited nickel manganite thermistor films for microbolometer applications, *J. Am. Ceram. Soc.* **94** (2011) 516–523.

[86] Schulze, H., Li, J., Dickey, E. C., and Trolier-Mckinstry, S., Synthesis, phase characterization, and properties of chemical solution-deposited nickel manganite thermistor thin films, *J. Am. Ceram. Soc.* **92** (2009) 738–744.

[87] Wu, C. H., Ma, J. S., and Lu, C. H., Synthesis and characterization of nickel-manganese oxide via the hydrothermal route for electrochemical capacitors, *Curr. Appl. Phys.* **12** (2012) 1190–1194.

[88] Hadj-Sadok Ouaguenouni, M., Benadda, A., Kiennemann, A., and Barama, A., Preparation and catalytic activity of nickel-manganese oxide catalysts in the reaction of partial oxidation of methane, *Comptes Rendus Chim.* **12** (2009) 740–747.

[89] Menezes, P. W., Indra, A., Littlewood, P., Göbel, C., Schomäcker, R., and Driess, M., A single-source precursor approach to self-supported nickel-manganese-based catalysts with improved stability for effective low-temperature dry reforming of methane, *Chempluschem* **81** (2016) 370–377.

[90] Morales, M. R., Barbero, B. P., and Cadús, L. E., Combustion of volatile organic compounds on manganese iron or nickel mixed oxide catalysts, *Appl. Catal. B Environ.* **74** (2007) 1–10.

[91] Wei, C., Cheng, C., Ma, L., Liu, M., Kong, D., Du, W., et al., Mesoporous hybrid NiOx-MnOx nanoprisms for flexible solid-state asymmetric supercapacitors, *Dalt. Trans.* **45** (2016) 10789–10797.

[92] MAEDA, Y., ARIYOSHI, K., KAWAI, T., SEKIYA, T., and OHZUKU, T., Effect of deviation from Ni/Mn stoichiometry in Li[Ni1/2Mn3/2]O4 upon rechargeable capacity at 4.7 V in nonaqueous lithium cells, *J. Ceram. Soc. Japan* **117** (2009) 1216–1220.

[93] Mehandjiev, D., Naydenov, A., and Ivanov, G., Ozone decomposition, benzene and CO oxidation over NiMnO3-ilmenite and NiMn2O4-spinel catalysts, *Appl. Catal. A Gen.* **206** (2001) 13–18.

[94] Dou, S., Review and prospect of layered lithium nickel manganese oxide as cathode materials for Li-ion batteries, *J. Solid State Electrochem.* **17** (2013) 911–926.

[95] Fang, X., Ge, M., Rong, J., Che, Y., Aroonyadet, N., Wang, X., et al., Ultrathin surface modification by atomic layer deposition on high voltage cathode LiNi 0.5 Mn 1.5 O 4 for lithium ion batteries, *Energy Technol.* **2** (2014) 159–165.

[96] Sun, Y.-K., Myung, S.-T., Park, B.-C., and Yashiro, H., Improvement of the electrochemical properties of Li[Ni0.5Mn0.5]O2 by AlF3 coating, *J. Electrochem.*

Soc. **155** (2008) A705.

[97] Huang, M., Zhao, X. L., Li, F., Zhang, L. L., and Zhang, Y. X., Facile synthesis of ultrathin manganese dioxide nanosheets arrays on nickel foam as advanced binder-free supercapacitor electrodes, *J. Power Sources* **277** (2015) 36–43.

[98] Yoshino, T., Kobayashi, K., Araki, S., Nakamura, K., and Kobayashi, N., Electrochromic properties of electrochemically fabricated nanostructure nickel oxide and manganese oxide films, *Sol. Energy Mater. Sol. Cells* **99** (2012) 43–49.

[99] Chavan, U. J., and Yadav, A. A., Electrochemical behavior of spray deposited mixed nickel manganese oxide thin films for supercapacitor applications, *J. Mater. Sci. Mater. Electron.* **0** (2016) 0.

[100] Patoux, S., Daniel, L., Bourbon, C., Lignier, H., Pagano, C., Le Cras, F., et al., High voltage spinel oxides for Li-ion batteries: From the material research to the application, *J. Power Sources* **189** (2009) 344–352.

[101] Patoux, S., Sannier, L., Lignier, H., Reynier, Y., Bourbon, C., Jouanneau, S., et al., High voltage nickel manganese spinel oxides for Li-ion batteries, *Electrochim. Acta* **53** (2008) 4137–4145.

[102] Choi, H. W., Kim, S. J., Rim, Y.-H., and Yang, Y. S., Effect of lithium deficiency on lithium-ion battery cathode LixNi0.5Mn1.5O4, *J. Phys. Chem. C* **119** (2015) 27192–27199.

[103] Wang, Y., Yang, G., Yang, Z., Zhang, L., Fu, M., Long, H., et al., High power and capacity of LiNi0.5Mn1.5O4 thin films cathodes prepared by pulsed laser deposition, *Electrochim. Acta* **102** (2013) 416–422.

[104] Kakvand, P., Rahmanifar, M. S., El-Kady, M. F., Pendashteh, A., Kiani, M. A., Hashami, M., et al., Synthesis of NiMnO3/C nano-composite electrode materials for electrochemical capacitors, *Nanotechnology* **27** (2016) 315401.

[105] Wang, L., Duan, G., Zhu, J., Chen, S.-M., and Liu, X., High capacity supercapacitor material based on reduced graphene oxide loading mesoporpus murdochite-type Ni6MnO8 nanospheres, *Electrochim. Acta* **219** (2016) 284–294.

[106] Latorre-Sanchez, M., Atienzar, P., Abellán, G., Puche, M., Fornés, V., Ribera, A., et

al., The synthesis of a hybrid graphene–nickel/manganese mixed oxide and its performance in lithium-ion batteries, *Carbon N. Y.* **50** (2012) 518–525.

[107] Periyasamy, S., Subramanian, P., Levi, E., Aurbach, D., Gedanken, A., and Schechter, A., Exceptionally active and stable spinel nickel manganese oxide electrocatalysts for urea oxidation reaction, *ACS Appl. Mater. Interfaces* **8** (2016) 12176–12185.

[108] He, X., Yin, F., Li, Y., Wang, H., Chen, J., Wang, Y., et al., NiMnO3/NiMn2O4 oxides synthesized via the aid of pollen: Ilmenite/spinel hybrid nanoparticles for highly efficient bifunctional oxygen electrocatalysis, *ACS Appl. Mater. Interfaces* **8** (2016) 26740–26757.

[109] Le, D. T., Jeon, C. J., Lee, K. W., Jeong, Y. H., Yun, J. S., Yoon, D. H., et al., Liquid flow deposited spinel (Ni,Mn)3O4 thin films for microbolometer applications, *Appl. Surf. Sci.* **330** (2015) 366–373.

[110] Le, D. T., Jeon, C. J., Lee, K. W., Jeong, Y. H., Yun, J. S., Yoon, D. H., et al., Characterization of ternary (Ni,Co,Mn)3O4 thin films for microbolometer applications, *J. Alloys Compd.* **650** (2015) 415–420.

[111] Lu, H. L., Scarel, G., Li, X. L., and Fanciulli, M., Thin MnO and NiO films grown using atomic layer deposition from ethylcyclopentadienyl type of precursors, *J. Cryst. Growth* **310** (2008) 5464–5468.

[112] Lamperti, A., Spiga, S., Lu, H. L., Wiemer, C., Perego, M., Cianci, E., et al., Study of the interfaces in resistive switching NiO thin films deposited by both ALD and e-beam coupled with different electrodes (Si, Ni, Pt, W, TiN), *Microelectron. Eng.* **85** (2008) 2425–2429.

[113] Lu, H. L., Scarel, G., Wiemer, C., Perego, M., Spiga, S., Fanciulli, M., et al., Atomic layer deposition of NiO films on Si(100) using cyclopentadienyl-type compounds and ozone as precursors, *J. Electrochem. Soc.* **155** (2008) H807.

[114] Utriainen, M., Kröger-Laukkanen, M., and Niinistö, L., Studies of NiO thin film formation by atomic layer epitaxy, *Mater. Sci. Eng. B* **54** (1998) 98–103.

[115] Lindahl, E., Lu, J., Ottosson, M., and Carlsson, J.-O., Epitaxial NiO (100) and NiO (111) films grown by atomic layer deposition, *J. Cryst. Growth* **311** (2009) 4082–

4088.

[116] Lindahl, E., Ottosson, M., and Carlsson, J. O., Atomic layer deposition of NiO by the Ni(thd)2/H2O precursor combination, *Chem. Vap. Depos.* **15** (2009) 186–191.

[117] Thimsen, E., Martinson, A. B. F., Elam, W., and Pellin, M. J., Energy levels, electronic properties, and rectification in ultrathin p-NiO films synthesized by atomic layer deposition, *J. Phys. Chem. C* **116** (2012) 16830–16840.

[118] Yang, T. S., Cho, W., Kim, M., An, K.-S., Chung, T.-M., Kim, C. G., et al., Atomic layer deposition of nickel oxide films using Ni(dmamp)2 and water, *J. Vac. Sci. Technol. A Vacuum, Surfaces, Film.* **23** (2005) 1238.

[119] Lindahl, E., Thin film synthesis of nickel containing compounds, Uppsala University, (2009).

[120] Burton, B. B., Fabreguette, F. H., and George, S. M., Atomic layer deposition of MnO using Bis(ethylcyclopentadienyl)manganese and H2O, *Thin Solid Films* **517** (2009) 5658–5665.

[121] Strandwitz, N. C., Comstock, D. J., Grimm, R. L., Nichols-Nielander, A. C., Elam, J., and Lewis, N. S., Photoelectrochemical behavior of n-type Si(100) electrodes coated with thin films of manganese oxide grown by atomic layer deposition, *J. Phys. Chem. C* **117** (2013) 4931–4936.

[122] Pickrahn, K. L., Park, S. W., Gorlin, Y., Lee, H. B. R., Jaramillo, T. F., and Bent, S. F., Active MnOx electrocatalysts prepared by atomic layer deposition for oxygen evolution and oxygen reduction reactions, *Adv. Energy Mater.* **2** (2012) 1269–1277.

[123] Godlewski, M., Wójcik-Głodowska, A., Guziewicz, E., Yatsunenko, S., Zakrzewski, A., Dumont, Y., et al., Optical properties of manganese doped wide band gap ZnS and ZnO, *Opt. Mater. (Amst).* **31** (2009) 1768–1771.

[124] Wójcik, A., Kopalko, K., Godlewski, M., Guziewicz, E., Jakieła, R., Minikayev, R., et al., Magnetic properties of ZnMnO films grown at low temperature by atomic layer deposition, *Appl. Phys. Lett.* **89** (2006) 51907.

[125] Nilsen, O., Fjellvåg, H., and Kjekshus, A., Growth of manganese oxide thin films by

atomic layer deposition, *Thin Solid Films* **444** (2003) 44–51.

[126] Miikkulainen, V., Ruud, A., Østreng, E., Nilsen, O., Laitinen, M., Sajavaara, T., et al., Atomic layer deposition of spinel lithium manganese oxide by film-body-controlled lithium incorporation for thin-film lithium-ion batteries, *J. Phys. Chem. C* **118** (2014) 1258–1268.

[127] Mattelaer, F., Bosserez, T., Rongé, J., Martens, J. A., Dendooven, J., and Detavernier, C., Manganese oxide films with controlled oxidation state for water splitting devices through a combination of atomic layer deposition and post-deposition annealing, *RSC Adv.* **6** (2016) 98337–98343.

[128] Ahvenniemi, E., and Karppinen, M., ALD/MLD processes for Mn and Co based hybrid thin films, *Dalt. Trans.* (2016).

[129] Jin, H., Hagen, D., and Karppinen, M., Low-temperature atomic layer deposition of crystalline manganese oxide thin films, *Dalt. Trans.* **34** (2016) 01A109.

[130] Mattelaer, F., Vereecken, P. M., Dendooven, J., and Detavernier, C., Deposition of MnO anode and MnO2 cathode thin films by plasma enhanced atomic layer deposition using the Mn(thd)3 precursor, *Chem. Mater.* **27** (2015) 3628–3635.

[131] Nilsen, O., Foss, S., Fjellvåg, H., and Kjekshus, A., Effect of substrate on the characteristics of manganese(IV) oxide thin films prepared by atomic layer deposition, *Thin Solid Films* **468** (2004) 65–74.

[132] Cohen, S. L., Liehr, M., and Kasi, S., Mechanisms of copper chemical vapor deposition, *Appl. Phys. Lett.* **60** (1992) 50–52.

[133] Filies, O., Böling, O., Grewer, K., Lekki, J., Lekka, M., Stachura, Z., et al., Surface roughness of thin layers—a comparison of XRR and SFM measurements, *Appl. Surf. Sci.* **141** (1999) 357–365.

[134] Pietsch, U., Holý, V., and Baumbach, T., *High-Resolution X-Ray Scattering*, Springer New York, New York, NY, 2004.

[135] Bouroushian, M., and Kosanovic, T., Characterization of Thin Films by Low Incidence X-Ray Diffraction, *Cryst. Struct. Theory Appl.* **1** (2012) 35–39.

[136] Larbi, T., Haj Lakhdar, M., Amara, A., Ouni, B., Boukhachem, A., Mater, A., et al.,

Nickel content effect on the microstructural, optical and electrical properties of p-type Mn3O4 sprayed thin films, *J. Alloys Compd.* **626** (2015) 93–101.

[137] Khodair, Z. T., Kamil, A. A., and Abdalaah, Y. K., Effect of annealing on structural and optical properties of Ni(1−x)MnxO nanostructures thin films, *Phys. B Condens. Matter* **503** (2016) 55–63.

[138] Díez, A., Schmidt, R., Sagua, A. E., Frechero, M. A., Matesanz, E., Leon, C., et al., Structure and physical properties of nickel manganite NiMn2O4 obtained from nickel permanganate precursor, *J. Eur. Ceram. Soc.* **30** (2010) 2617–2624.

[139] Goldstein, J., and Yakowitz, H., *Practical Scanning Electron Microscopy*, Springer US, Boston, MA, 1975.

[140] Layek, S., and Verma, H. C., Room temperature ferromagnetism in Mn-doped NiO nanoparticles, *J. Magn. Magn. Mater.* **397** (2016) 73–78.

[141] Hendi, A. H. Y., Al-Kuhaili, M. F., and Durrani, S. M. A., Chemical and optical properties of MnO2 thin films prepared by reactive evaporation of manganese, *Int. J. Res. Eng. Technol.* **5** (2016) 320–328.